Title
Advanced Penning-type ion source development and passive beam focusing techniques for an associated particle imaging neutron generator

Author
Sy, Amy

Publication Date
2013

Peer reviewed|Thesis/dissertation

Advanced Penning-type ion source development and passive beam focusing techniques for an associated particle imaging neutron generator with enhanced spatial resolution

by

Amy Vong Sy

A dissertation submitted in partial satisfaction of the
requirements for the degree of

Doctor of Philosophy

in

Engineering - Nuclear Engineering

in the

Graduate Division

of the

University of California, Berkeley

Committee in charge

Professor Ka-Ngo Leung, Chair
Professor Edward Morse
Professor Michael Lieberman
Dr. Qing Ji

Spring 2013

Abstract

Advanced Penning-type ion source development and passive beam focusing techniques for an associated particle imaging neutron generator with enhanced spatial resolution

by

Amy Vong Sy

Doctor of Philosophy in Engineering-Nuclear Engineering

University of California, Berkeley

Professor Ka-Ngo Leung, Chair

The use of accelerator-based neutron generators for non-destructive imaging and analysis in commercial and security applications is continuously under development, with improvements to available systems and combinations of available techniques revealing new capabilities for real-time elemental and isotopic analysis. The recent application of associated particle imaging (API) techniques for time- and directionally-tagged neutrons to induced fission and transmission imaging methods demonstrates such capabilities in the characterization of fissile material configurations and greatly benefits from improvements to existing neutron generator systems. Increased neutron yields and improved spatial resolution can enhance the capabilities of imaging methods utilizing the API technique. The work presented in this dissertation focused on the development of components for use within an API neutron generator with enhanced system spatial resolution. The major focus areas were the ion source development for plasma generation, and passive ion beam focusing techniques for the small ion beam widths necessary for the enhanced spatial resolution. The ion source development focused on exploring methods for improvement of Penning-type ion sources that are used in conventional API neutron generator systems, while the passive beam focusing techniques explored both ion beam collimation and ion guiding with tapered dielectric capillaries for reduced beam widths at the neutron production target.

Penning-type ion sources are utilized in commercially available API neu-

tron generator systems due to their compactness, ease of operation, and low power consumption. These types of ion sources, however, are characterized by low plasma densities and low atomic ion fractions in the discharge that make them unattractive for neutron generator applications requiring high neutron yields. The ion source development undertaken as part of this dissertation work focused on methods by which improvements to the plasma density and atomic ion fraction of Penning-type ion sources could be effected, and the modular Berkeley Lab Penning source was designed and fabricated to test the effects of the various improvement schemes. These improvement schemes included electrode material variation for enhanced plasma density from increased secondary electron emission under ion bombardment; electron injection into the discharge by way of electron field emission from carbon nanofiber arrays; and enhanced magnetic confinement of the plasma with the use of multi-cusp magnetic fields. Strategic combinations of these improvement schemes have resulted in a factor of 20 improvement in the extracted ion current density over the baseline source performance. The resultant extracted ion current density of 2.2 mA/cm^2 is comparable to existing Penning sources for neutron generator applications, with the Berkeley Lab Penning source exhibiting lower power consumption.

The spatial resolution of an API system is heavily dependent on the diameter of the ion beam spot at the neutron production target. Current API systems can achieve beam spots as small as 2 mm in diameter with the use of active focusing elements. In this work, passive beam focusing techniques were explored to achieve beam widths of 1 and 2 mm in diameter without the use of active focusing elements. Ion beam collimation with the use of high aspect ratio extraction channels at the ion source was explored to physically remove those ions in the beam with high divergence angles. At beam energies of 81 keV, the beam diameter at the target was consistent with the diameter of the extraction aperture, indicating that the high aspect ratio extraction channels act to suppress those ions with high divergence angles that act to increase the beam diameter downstream. However, the significant beam loss due to collimation with high aspect ratio extraction channels, with no focusing effects and corresponding increase in beam current density at the target, makes the use of ion beam collimation for small beam widths viable

only for high ion current densities.

Because the use of high aspect ratio extraction channels results in significant beam loss and no increase in the extracted ion current density, the passive beam focusing technique known as ion guiding was explored. The use of ion guiding with tapered dielectric capillaries for the transmission of tens of μA of hydrogen or deuterium ion current represents an area of the experimental parameter space that has not yet been explored. Tapered Pyrex tubes with inlet inner diameters of 2-3 mm and exit inner diameters of 0.5-1 mm were used in the ion guiding experiments for the passive focusing of ion beams to beam widths on the order of 1 mm in diameter. For a 40 keV, 20 μA deuterium ion beam from the Berkeley Lab Penning source, average transmission efficiencies of 50% were measured. This represents a transmitted ion current of 10 μA and corresponding beam compression factor of 6-8. Simultaneous measurements of the relative neutron yield resulting from D-D fusion reactions at a neutron production target initially confirmed the magnitude of the transmitted ion current, but secondary electron currents were observed to affect the ion current measurement and warranted further neutron yield measurements. Further neutron yield measurements utilizing different target materials resulted in a calculated transmission efficiency of 24% and corresponding beam compression factor of approximately 4. Further work is required to more accurately measure the transmitted ion current, as well as characterize the energy distribution of ions transmitted through tapered dielectric capillaries and the resultant effects on the neutron yield. The neutron yield measurements also indicated that the Pyrex tube itself contributes significantly to the neutron yield; this has implications for the further use of the ion guiding method for the API application and requires further study. The stable transmission of 5-10 μA of ion current through a tapered dielectric capillary represents at least an order of magnitude increase in the maximum ion current typically observed to have been transmitted with this ion guiding effect. These results are promising for the further extension of this method to higher beam currents for increased neutron yields.

Acknowledgments

I am deeply grateful to the members of my dissertation committee, Professor Ka-Ngo Leung, Professor Edward Morse, Professor Michael Lieberman, and Dr. Qing Ji, for their time and effort in overseeing and approving this dissertation work. I am especially grateful to Professor Leung for the opportunity to develop an interest in the field of ion source technology, and consider myself extremely fortunate to have been able to pursue this research. I cannot thank Dr. Ji enough for her role as my research advisor; I have learned so much under her guidance, and am forever thankful for the experience.

This work would not have been possible without the support of past and present members of the Ion Beam Technology group at Lawrence Berkeley National Laboratory, individuals I can always count on for fruitful and entertaining discussions, scientific and otherwise. I would like to thank Dr. Bernhard Ludewigt, Dr. Kelly Jordan, and Dr. Tak-Pui Lou for their guidance and assistance in my first research efforts. I would like to thank Dr. Thomas Schenkel and Dr. Arun Persaud for helpful discussions and invaluable insight. I would like to thank Dr. Christoph Weis for the roller hockey injuries. Special thanks go to former and current inhabitants of the Building 5 graduate student office, including Dr. Michael King, Dr. Ying Wu, Julian Schwartz, and Michael Ilg, for making a windowless office slightly less unbearable, for good advice, and for experimental assistance. My sincerest gratitude goes out to Stephen Wilde, Thomas McVeigh, and Michael Dickinson for their technical support in taking concept to reality and making it work.

I would like to thank the faculty and staff of the UC Berkeley Department of Nuclear Engineering, for assistance and guidance in all academic matters.

Finally, there are no words to express how much the love and support of my family has meant to me over the course of my graduate studies. This work is especially dedicated to my parents, for all of their hard work and sacrifice.

For my family.

Contents

List of Figures

List of Tables

Chapter 1

Introduction

1.1 Motivation

In our fast-paced, modern world, non-destructive analysis and imaging methods are increasingly attractive for maintaining safety and security standards with minimal interruption to the complex networks that deal with the movement of materials, goods, and people all over the world. The pervasive threat of terrorist activity, whether by way of diverting special nuclear materials (SNM) from transport routes or the transport of other illicit materials such as explosives, etc. underscores the importance of accurate, reliable methods for elemental and isotopic analysis. Regardless of the application, systems with short imaging times and high spatial resolution are desired to quickly obtain spatial maps of material distribution within the object of interest. Methods utilized for these types of analysis and imaging systems have been studied for the determination of carbon, nitrogen, and oxygen content for the detection of explosives [1], and have also been studied for the detection of fissionable materials [2]. Advances in system capabilities are important for threat deterrence and national security applications, but also have applications in commercial industries for online elemental analysis [3]. The versatility of such systems is also greatly enhanced by the incorporation of compact and inexpensive components that require low power consumption; these characteristics enable field-portability for wider deployment.

1.2 General detection systems

Types of detection systems employed in different situations and different locations are context-specific, depending on the types of materials of interest. The origin of the detected signal classifies a detection system into one of two categories: passive detection systems, where the object of interest emits radiation signatures that are detected and allow for the identification of the radioactive isotopes present; and active interrogation systems, where the object of interest is irradiated with an external radiation source and the stimulated emission of radiation is detected and analyzed. Passive detection systems are widely deployed at shipping ports and similar gateways that see high volume and traffic of transported materials, but are typically limited to the detection of unshielded, naturally radioactive materials. Shielded SNM and non-radioactive explosive materials would not be detected by such passive systems. Active interrogation systems are inherently more complex due to the incorporation of radiation sources to induce detectable radiation signatures, but detection capabilities are greatly enhanced by the information obtained through the stimulated emission of radiation due to inelastic nuclear reactions.

1.2.1 Neutron-based imaging methods

Active interrogation systems utilizing neutron sources are especially of interest for homeland security applications such as SNM detection and treaty verification, as well as explosives detection. Neutron-based imaging methods have been used since the 1970s for commercial applications in the geology/mineral and oil industries, with recent interest over the past decade in the use of such methods for luggage and cargo screening applications. The use of neutrons as an active probing source is appropriate for the imaging of high-Z materials and shielded materials because neutrons are not subject to electromagnetic forces, and can easily penetrate dense materials that greatly attenuate X-rays and gamma rays. These neutrons can then induce different nuclear reactions with nuclei in the object being probed, providing characteristic radiation signatures that allow for the non-intrusive, non-destructive

identification of materials within the object of interest. Techniques utilizing both fast and thermal neutrons have been developed and are most suitable for different applications. Several fast neutron-based imaging techniques are described in the following sections.

Neutron transmission radiography

Neutron transmission imaging methods are similar to conventional transmission imaging methods utilizing X-rays or gamma rays, where the attenuation of the incident source particles by the interrogated material is used to obtain information on the areal density of the material the neutrons have traversed. Thermal neutrons are more easily absorbed, especially in the presence of lighter materials and materials with high hydrogen content, and thus may not be suitable for neutron transmission measurements. Fast neutrons with energies greater than 1 MeV have longer attenuation lengths and thus can produce images with greater contrast. One well-known method utilizing fast neutrons for neutron transmission measurements, pulsed fast neutron transmission spectroscopy (PFNTS) [4], [5], [6], makes use of a continuous neutron energy distribution and known neutron attenuation spectra specific to different materials. The transmitted neutron intensity and energy spectra are compared to known data to determine the composition of the object of interest.

Induced fission imaging

For the characterization of fissile material configurations, treaty verification, and other applications involving special nuclear materials, induced fission imaging can be utilized to create a spatial map of the distribution of fissionable materials within the object of interest. Fission events are induced within the object of interest with incident neutrons, and reaction products are detected and analyzed to determine the fissionable isotopes within the object that the interrogation neutrons have interacted with. The detected reaction products of interest include characteristic gamma rays and neutron multiplicities. Much work has been done to characterize the emission spectra from various materials due to thermal and fast neutron-induced fission

events [7], [8], [9]. This method is especially applicable in situations where the presence of fissionable materials is suspected, such that the proper interrogation and detection techniques are applied.

Fast neutron analysis

Fast neutron analysis [10], or FNA, utilizes a continuous, collimated beam of fast neutrons to excite nuclei within the object of interest. The excited nuclei emit characteristic gamma rays in the de-excitation process that are used to determine the composition of the object of interest. Monoenergetic neutrons are typically used for fast neutron analysis for well-defined incident neutron energies. This technique suffers from high background signal due to unwanted neutron interactions within the detectors. Utilizing a pulsed neutron source for pulsed fast neutron analysis (PFNA) [11] greatly improves the signal to background ratio by utilizing time of flight information to reject background events.

Associated particle imaging

Associated particle imaging (API) [12], [13], [14] is a special form of fast neutron analysis that takes advantage of the physics of the deuterium-deuterium (D-D) or deuterium-tritium (D-T) fusion reactions to tag neutrons used in active interrogation methods with time and trajectory information, providing electronic collimation that enhances the detected signal of interest over the background signal. API makes use of the associated particle emitted following the D-D or D-T fusion reactions. In the D-D and D-T fusion reactions, the resultant neutron and associated particle (^{3}He for D-D and ^{4}He for D-T fusion, respectively) are emitted at an angle of nearly 180° with respect to each other in accordance with the conservation of linear momentum. Because the neutron emission from both the D-D and D-T fusion reactions is isotropic, some form of collimation is necessary to limit the extent of the image voxel size under neutron interrogation at any given time. Position-sensitive detection of the associated particle from the fusion reaction, as well as coincidence detection between the alpha particle and characteristic gammas from the de-excitation of the nuclei that have interacted with the incident neutrons, allow

for the associated particle trajectory and the correlated neutron trajectory to be determined. Limiting the spatial extent of the alpha trajectories that can contribute to the image likewise limits the spatial extent of neutrons interrogating the object, resulting in the desired electronic collimation. The position-sensitive detection of an alpha particle starts a timing window for the detection of characteristic gamma rays based on the time-of-flight expected of the monoenergetic neutron. The detection of gammas within this timing window are then coincident with an accepted alpha particle, and the signal is accepted. Detected gammas that are not coincident with accepted alpha trajectories are rejected as background signal. A schematic of the API method is shown in Figure 1.1.

API systems utilize accelerator-based neutron generators (see section 1.3) to achieve the fusion reactions necessary for neutron generation. The spatial resolution of an API system is dependent on the localization of the position of the neutron (and associated particle) generation, i.e. where the fusion reactions occur. As shown in Figure 1.1, neutrons are produced at the target where the D^+/T^+ ion beam is incident; thus a major contributor to the spatial resolution of such systems is the ion beam spot size on target. Current API systems utilize accelerator-based D-T neutron generators capable of achieving spatial resolution of 2-5 mm [15], with output neutron yields on the order of 5e7 n/s. Recent work involving the application of API techniques to induced fission and transmission imaging methods [16], [17] offers new capabilities for the characterization of fissile material configurations as well as enhanced detection of SNM. API systems with improved spatial resolution and increased neutron yields are desired to fully exploit these capabilities.

1.3 Accelerator-based neutron generators

Accelerator-based neutron generators have several advantages over traditional radioisotope sources. Radioisotope sources such as ^{252}Cf constantly emit neutrons as the isotope decays, thus requiring shielding when not in use to prevent unnecessary radiation exposure. The source strength also naturally decays over time. An accelerator-based neutron generator has the ability to provide neutrons on demand, with more sophisticated timing struc-

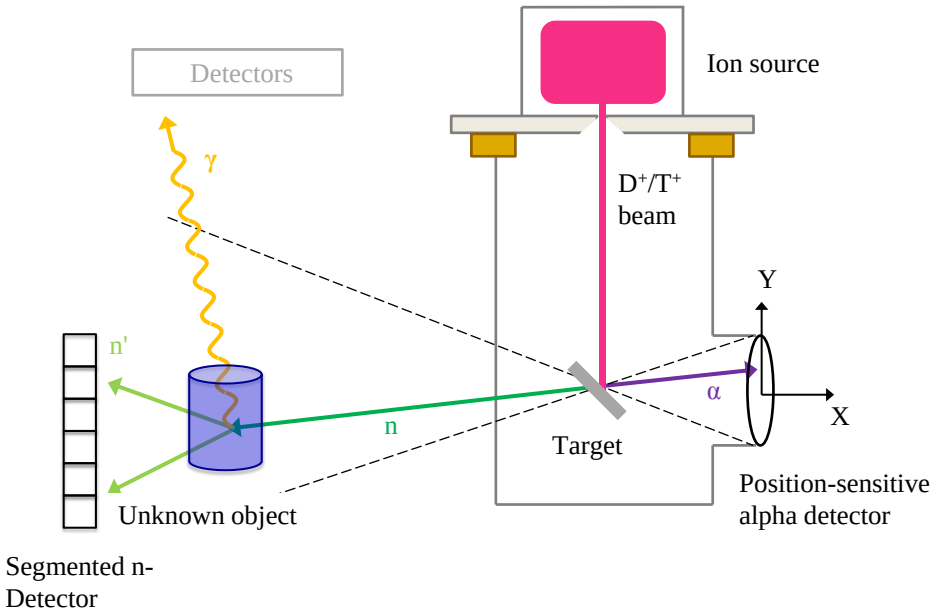

Figure 1.1: Schematic of the API method. Here, D-T fusion reactions at the target create a neutron and associated alpha particle that is detected at the position-sensitive alpha detector. The neutron interacts with a nucleus in the object of interest, emitting a gamma ray that is detected at the external detector array. The dashed lines indicate the spatial extent of the accepted alpha particle trajectories and the resultant extent of the interrogation space. For fissionable materials, the neutron may also induce fission events resulting in neutron multiplicity events; the additional neutrons are detected with segmented neutron detectors.

tures available with both pulsed and continuous wave operation. Accelerator-based neutron generators rely on neutron generation from fusion reactions, typically the deuterium-deuterium (D-D) or deuterium-tritium (D-T) fusion reactions, and thus output monoenergetic neutrons with variable neutron yields based on system parameters of the neutron generator. The neutron yield is a function of both the relative energies of the reactant atoms and the flux of reactant atoms; in an accelerator-based neutron generator, deuterium or tritium atoms are ionized to facilitate the acceleration to high energies for useful neutron yields. Key components of an accelerator-based neutron generator are thus the ion source for generation of deuterium and/or tritium ions; acceleration column components for proper acceleration and focusing of the ions extracted from the ion source; and a neutron production target where the fusion reactions occur. Figure 1.2 shows a schematic of the components required for a typical neutron generator. A plasma consisting of deuterium and/or tritium ions and electrons is ignited within the ion source. An ion beam is formed by extracting and accelerating ions from the ion source with the application of electrostatic potential gradients that facilitate the flow of ions from the source to the target. The target is either preloaded with deuterium and/or tritium atoms, or is loaded as beam ions are driven into the target in a process known as "beam-loading" of the target. Fusion reactions thus occur between beam ions and atoms in the target, and the neutron yield is a function of the beam energy, atomic fraction of ions in the beam, and ion beam current.

1.3.1 D-D and D-T neutron yields

The D-D and D-T fusion reactions generate monoenergetic neutrons of 2.45 and 14.1 MeV, respectively, along with associated helium isotopes ^{3}He and ^{4}He that are emitted to satisfy conservation of energy and momentum requirements.

$$D + D \rightarrow n(2.45MeV) +^3 He(0.82MeV) \tag{1.1}$$

$$D + T \rightarrow n(14.1MeV) +^4 He(3.5MeV) \tag{1.2}$$

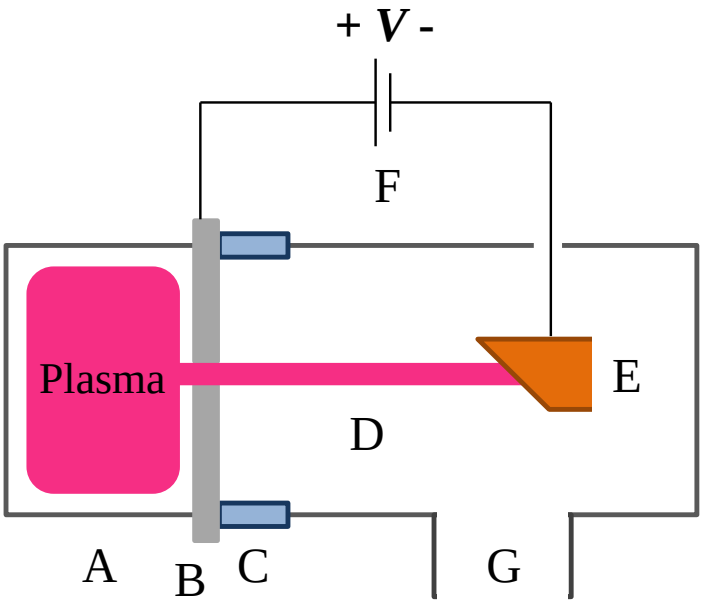

A–Ion source
B–Plasma electrode
C–High voltage insulator
D–Ion beam
E–Neutron production target
F–Applied high voltage
G–Port for pumping, etc.

Figure 1.2: Schematic of an accelerator-based neutron generator. Deuterium and/or tritium ions are generated within the ion source and accelerated through the aperture in the plasma electrode by the applied high voltage. The resultant ion beam produces neutrons at the neutron production target. The side port depicted in (G) would not be used in a sealed-tube system, as sealed-tube systems do not utilize external vacuum pumps.

The fusion reaction cross-section is a measure of the probability for the fusion reaction to occur, and varies with the energy of the reactant species. The D-D and D-T fusion reaction cross-sections as a function of center of mass energy are shown in Figure 1.3 [18]. For a deuterium ion beam incident on a deuterium or tritium loaded target, the total neutron yield over all incident ion energies is given by the yield integral

$$Y = \int_E N\sigma(E)\frac{I}{q}\left[\frac{\mathrm{d}(E)}{\mathrm{d}x}\right]^{-1}\mathrm{d}E \tag{1.3}$$

where

N: Atom density of D or T in target material
$\sigma(E)$: Fusion reaction cross-section
I: Deuterium ion current
q: Deuterium ion charge
$\left[\frac{\mathrm{d}(E)}{\mathrm{d}x}\right]$: Stopping power of the target

The neutron yield per unit ion current for beam ions incident on a neutron production target, here given in units of neutrons per second per μA of incident ion current, as a function of beam energy for both D-D and D-T reactions is given in Figure 1.4 (adapted from [19]). Several relationships can be noted from Figure 1.4. For constant ion current, the D-T neutron yield increases rapidly as the beam energy is increased up to 100 keV. Further increasing the beam energy up to 300 keV results in less than one order of magnitude increase in the neutron yield, with the yield curve essentially saturating beyond beam energies of 300 keV (not shown). D-T neutron generators are typically operated at beam energies at or near 100 keV for this reason. The D-D neutron yield is about two orders of magnitude lower than the D-T neutron yield for the same incident beam current at the same beam energy, and the D-D yield curve shows greater relative increase in the neutron yield with higher beam energy as compared the D-T yield curve.

It is noted here that the yield curves given in Figure 1.4 assume purely monatomic deuterium (D^+) ion beams incident on a titanium target that has been fully loaded with either deuterium or tritium atoms. These are ideal assumptions, and experimental neutron yields will be slightly lower due to sev-

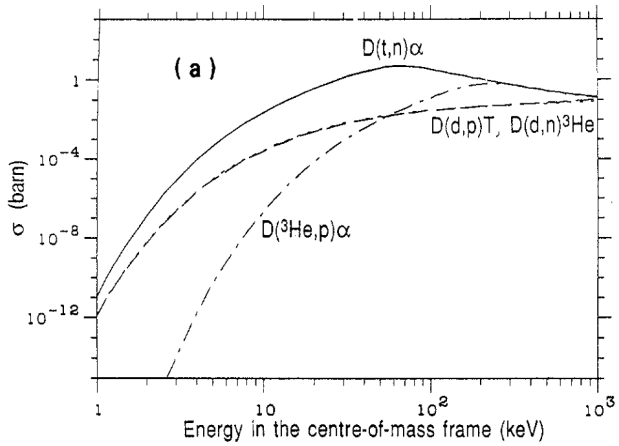

Figure 1.3: D-D and D-T fusion reaction cross-sections [18].

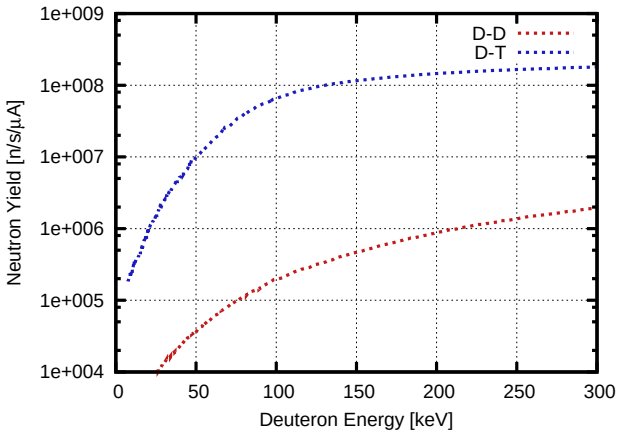

Figure 1.4: D-D and D-T neutron yields per unit ion current as a function of incident beam energy. The yields assume monatomic deuterium ions incident on titanium targets fully loaded with deuterium (for D-D fusion) or tritium (for D-T fusion) atoms.

eral effects. Target materials such as titanium, molybdenum, and scandium are utilized for their ability to retain large quantities of hydrogen isotopes in their material matrices through the formation of metal hydrides but often have poor thermal conductivities. As the target is bombarded with energetic ions, the target surface heats up and allows deuterium and/or tritium atoms in the target matrix to diffuse away from the incident ion beam, out of range of the incoming ions. This reduces the density of deuterium/tritium atoms in the target matrix at the ion beam spot, thus reducing the fusion reaction rate and the resultant neutron yield. The D-T neutron yield can also decrease over time in the case that a deuterium ion beam is accelerated into a tritium-loaded target. In this case, the tritium inventory available for fusion reactions is limited by the amount pre-loaded into the target, and the neutron yield will decrease as this inventory is depleted and fusion reactions between beam deuterium ions and beam-loaded deuterium atoms in the target occur. Finally, decreases in the theoretical maximum neutron yield also occur as a result of mixed ion species within the ion beam; the curves plotted in Figure 1.4 assume pure D^+ ion beams, while the fraction of D^+ ions in beams from real ion sources typically range between 10-90%, depending on the ion source. Radio-frequency and microwave-driven ion sources can produce ion beams where 90% of the deuterium ions in the beam are monatomic D^+, with the other 10% comprised of molecular D_2^+ and D_3^+ [20], [21]. Penning ion sources [22] typically produce ion beams where 80-90% of the deuterium ions in the beam are molecular D_2^+; the atomic ion fraction is thus only 10-20%. For a predominantly diatomic deuterium ion beam, as obtained from a Penning ion source, the neutron yield is comprised of contributions from both the monatomic and diatomic species. Diatomic D_2^+ ions break up upon impact at the target, with each deuterium atom receiving half of the incident beam energy. The effective beam current contribution from the diatomic deuterium is then increased by a factor of two; this, coupled with the reduced fusion cross-section due to the reduced beam energy of the newly created deuterium atoms, can result in up to a factor of five decrease in the neutron yield as compared to the theoretical maximum value. The reduced yield from predominantly diatomic deuterium ions makes those ion sources with low atomic ion fractions undesirable for high-yield neutron generators.

1.4 Compact API generator components

As previously discussed, the application of API techniques utilizing time- and directionally-tagged neutrons to induced fission and transmission imaging techniques has revealed new capabilities for these methods that substantially benefit from improved spatial resolution and increased neutron yields over existing API systems. Improved spatial resolution with increased neutron yield allows for faster, more sensitive detection capabilities than are currently available in the compact, portable accelerator-based neutron generators geared toward API applications. The work presented in this dissertation focuses on the development of components compatible with a compact accelerator-based neutron generator for associated particle imaging with enhanced spatial resolution. Key features of the ideal system include simple, self-focusing ion beam optics components that result in small beam widths on the order of 1 mm in diameter at the neutron production target without the use of active focusing elements. Active focusing elements are widely used in commercially available systems, allowing for beam widths on target to be focused to 2 mm in diameter, but the inclusion of such elements adds a layer of complexity to the overall system that is to be avoided in the current work. Key areas lie in the ion source development and development of passive ion beam focusing techniques to reduce the beam diameter with minimal current loss. The ion source development undertaken focused on the development of an advanced Penning-type ion source, with methods and results presented in Chapter 2. Passive focusing techniques centered on ion beam collimation with high aspect ratio extraction channels, and ion beam guiding using tapered dielectric capillaries; methods and results are presented in Chapter 3. Neutron production target considerations and initial neutron yield measurements are presented in Chapter 4. Summary and outlook are presented in Chapter 5.

Chapter 2

Penning-type ion source development

2.1 Introduction

Penning-type ion sources have continued to experience extensive use and development since first discharge experiments were performed by Penning [23] in 1936. These types of discharge sources have remained as vital front-end components for compact neutron generators due to their simplicity in both design and operation relative to ion sources with comparable extracted ion current density.

2.2 Penning ion source discharge characteristics

Penning-type ion sources utilize a DC discharge for ion generation, and thus the ion source design is often much simpler than that for discharges that are driven by radio-frequency waves or microwaves. A typical cold cathode Penning source geometry is illustrated in Figure 2.1. Here, the discharge source geometry is cylindrically symmetric about the central axis at R = 0.

A DC high voltage is applied between the anode and the cathode; this discharge voltage is typically on the order of 500-5000 V. The symmetric

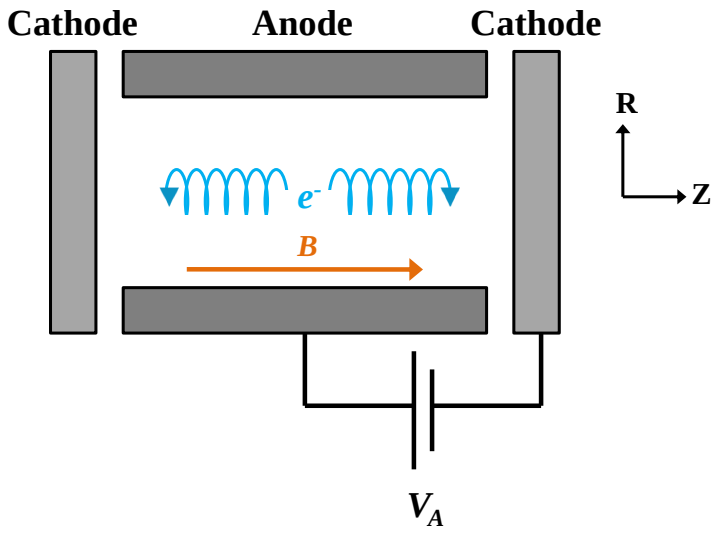

Figure 2.1: Schematic of typical Penning source electrode geometry. The two cathodes are at the same potential. The anode voltage V_A is applied between the anode and two cathodes. The magnetic field B is in the axial Z direction and causes electrons in the discharge region to gyrate around the magnetic field lines. The electrons oscillate along the axial Z direction, undergoing ionizing collisions with background neutral species in the process.

arrangement of electrodes increases the efficiency of the discharge by increasing the path length of the ionizing electrons through the discharge region; the electric field distribution induced by the applied high voltage forces the ionizing electrons to oscillate between the two cathodes. The path length of the ionizing electrons is further increased by the addition of a magnetic field along the axial direction of the discharge chamber, along the Z direction in the previous figure. The magnetic field along the direction of the path of the ionizing electrons induces a Larmor gyration about the magnetic field lines, with frequency

$$\omega_{ce} = \frac{eB}{m_e} \tag{2.1}$$

and radius

$$r_{ce} = \frac{m_e v_\perp}{eB} \tag{2.2}$$

where

m_e: electron mass
B: magnitude of the axial magnetic field
$v_\perp$: velocity component transverse to the axial magnetic field

The frequency is often referred to as the electron cyclotron frequency; the radius of gyration is often referred to as the Larmor radius. Similar equations apply for ionized species in the discharge; the electron charge and mass are replaced by the charge and mass of the ionized species, respectively. For electrons in the Penning-type ion source described in the following sections, typical values for the frequency and radius of gyration are 7.03e9 rad/s and 2.4 mm, respectively, based on an axial magnetic field strength of 400 G and maximum transverse electron energy of 800 eV. The axial magnetic field imposes a type of magnetic confinement on the ionizing electrons, as the electrons are "tied" to the field lines through the induced gyromotion, and the radius of gyration is typically much smaller than the dimensions of the discharge chamber. The increased path length of ionizing electrons through both the symmetric electrode arrangement and the axial magnetic confinement allows for the discharge to be ignited and maintained at much lower gas

pressures than would be possible otherwise. It is noted that these equations most accurately describe the electron behavior before the discharge is ignited; the presence of a plasma and the resultant local electric and magnetic fields results in much more complex particle trajectories.

Free electrons in the neutral gas are accelerated by the applied electric field and undergo collisions with the neutral gas species. If the electron has sufficient energy, the collision can remove one or more electrons from the neutral species, resulting in an ion and secondary electron. The primary electron loses energy in each collision, and can continue to ionize neutral species until it no longer has sufficient energy to remove an electron, or is lost to the discharge chamber walls. The secondary electrons can also be accelerated by the applied electric field and go on to ionize neutrals. It is by this process that the plasma is ignited and sustained. Table 2.1 lists the various collision processes and resultant products available for electrons in a hydrogen gas environment. The dominant ionization process is the electron impact ionization of the hydrogen molecule. Ions created through these ionization processes are much more massive than the electrons and are typically not well confined by the axial magnetic field. These ions are swept to the two cathodes by the symmetric potential distribution within the discharge region, and are also accelerated by the applied electric field. Additional secondary electrons are emitted from the cathodes upon ion impact; these secondary electrons are accelerated back into the discharge region and thus are also a major contributor to the sustenance of the Penning discharge.

Table 2.1: Electron impact ionization processes in a hydrogen gas environment [22].

$e^- + H_2$	$\rightarrow$	$e^- + H + H$	8.8 eV
$e^- + H_2$	$\rightarrow$	$e^- + e^- + H_2^+$	15.4 eV
$e^- + H$	$\rightarrow$	$e^- + e^- + H^+$	13.6 eV
$e^- + H_2$	$\rightarrow$	$e^- + e^- + H + H^+$	18 eV
$e^- + H_2$	$\rightarrow$	$e^- + e^- + e^- + H^+ + H^+$	46 eV

The discharge source becomes an ion source with the introduction of an

extraction aperture through which ions can be extracted from the plasma. For the Penning discharge, an aperture or apertures in one or both cathodes allow for ions that would have been lost at that position on the cathode to exit the discharge chamber to the external vacuum region. As will be discussed in the following sections on ion extraction and beam formation, the application of an electric field gradient in the vacuum region external to the discharge region allows for these ions to be formed into a beam and accelerated for the final application. The extracted ion current is a function of both the plasma density within the ion source and the size of the extraction aperture. The plasma density within Penning discharges is relatively low, on the order of 10^{10} cm^{-3} [24], and is thus a major drawback in the use of Penning-type ion sources for high-yield neutron generator applications due to the resultant low extractable ion current. For hydrogen and hydrogen isotope discharges from Penning-type ion sources, the atomic ion fraction, the fraction of atomic versus molecular ions in an extracted ion beam, is also low, on the order of 10-20%; the low atomic ion fraction is attributed to both the low electron density (and thus the low plasma density) and short dwell time of molecular H_2^+ ions in the Penning discharge [25]. The low atomic ion fraction is also apparent in examining the cross sections for hydrogen ion formation under electron impact shown in Figure 2.2 from [26]. At primary electron energies relevant to the current discussion, on the order of 1000 eV, the cross section for the creation of a molecular H_2^+ ion is one order of magnitude higher than that for the creation of an atomic H^+ ion when both originate from molecular H_2 species. The situation quickly worsens as the primary electron energy decreases after each collision event: the cross section for H^+ formation drops more rapidly than that for H_2^+ formation. The cross sections for H_2^+ and H^+ formation are comparable when the atomic H^+ ion is formed from electron impact on the atomic H neutral, but this event requires the prior dissociation of neutral H_2 to the neutral atomic species. The low atomic ion fraction is an additional major drawback in the use of Penning-type ion sources for high-yield neutron generator applications; the neutron yield is strongly dependent on the fusion cross-section, which exhibits an energy dependence as discussed in section 1.3.1. For a diatomic deuterium ion beam (D_2^+) with beam energy of 100 keV being driven into a neutron production

target, each atom in the molecular ion carries half of the incident beam energy when the molecular ion dissociates at the neutron production target; at these energies, the fusion cross-section for each resultant atom is reduced by as much as one order of magnitude. This greatly reduces the maximum obtainable neutron yield despite the increase in effective beam current on the neutron production target. High molecular ion fractions in the extracted ion beam are thus undesirable for high-yield neutron generators.

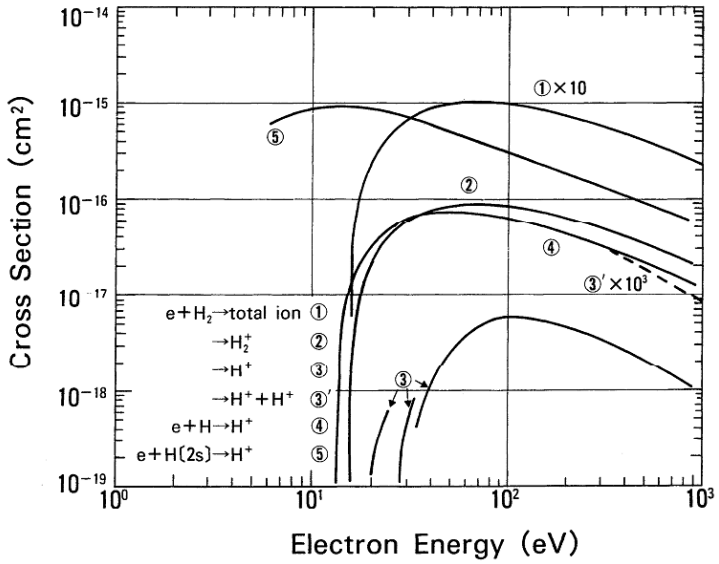

Figure 2.2: Cross-section data as a function of incident electron energy for hydrogen ion generation from [26].

Despite the limitations imposed by the low plasma density and low atomic ion fraction inherent to Penning-type ion sources, the compact nature and low power consumption readily achievable in such sources continue to make them attractive for further use in and development for neutron generator applications. Radio-frequency or microwave driven ion sources often consume several hundred watts of power in maintaining their discharges, while Penning sources used in commercially available neutron generator systems often consume much less discharge power, on the order of tens of watts. Overall neutron generator system design is also greatly simplified with the use of a Penning-type ion source, as the mechanisms by which wave-driven dis-

charges are sustained often require more complex and bulky system design and requisite components.

2.2.1 Penning discharge pressure dependence

For a given axial magnetic field and applied discharge voltage, the Penning discharge can operate in several modes that are dependent on the pressure within the discharge volume and differ in the potential distribution within the discharge chamber [27]. Within the confines of a given mode, the discharge current is generally proportional to the source operating pressure, motivating early experiments involving the use of the Penning discharge as a pressure gauge. Higher pressures within the discharge chamber result in higher neutral density, and the mean free path for ionization decreases. Pressures are generally measured at the gas inlet into the discharge volume due to lack of direct access to the discharge volume. Historically, discharges operating at gas pressures at or below 0.1 mTorr have been characterized as operating in the "low pressure" regime, though the transition from low to high pressure regimes is loosely defined. It is noted here that the pressures of interest for the experiments described in forthcoming sections fall in the "high pressure" regime, typically between 0.5-3.0 mTorr. At these pressures, Penning discharge operation can become unstable. Operation in this regime often requires adjustment of the pressure within the source to maintain discharge stability, especially as the pressure approaches the stability limit for a given set of discharge conditions.

2.2.2 Penning discharge axial magnetic field dependence

For a given source operating pressure and applied discharge voltage, the discharge characteristics are affected by the magnitude of the axial magnetic field and the resultant magnetic confinement of the species within the plasma. Larger values of the axial magnetic field result in smaller electron and ion gyroradii, according to equation 2.2, and it is expected that electron losses to the anode are reduced with increased axial magnetic field. The plasma

density therefore is expected to increase with increased axial magnetic field, typically manifesting as an increase in the discharge current. Experimentally, however, the discharge current increases with increasing axial magnetic field up to some transition point, after which further increasing the axial magnetic field causes the discharge current to decrease. This behavior is described in [28]. It is possible that the decreased discharge current does in fact result from reduced electron losses to the anode and subsequent reduced ion losses to the cathode, as the loss currents must balance to maintain overall quasi-neutrality of the plasma; thus the overall plasma density may be higher with increased magnetic field.

2.2.3 Penning discharge applied voltage dependence

For a given pressure and axial magnetic field, the discharge current and extracted ion current increase with increased discharge voltage. Electrons are accelerated by the electric field within the discharge region and thus gain more energy for increased applied voltages between the anode and the two cathodes. An individual electron is then able to ionize more neutrals before its total energy falls below the energy required per ionization event.

2.3 Berkeley Lab Penning ion source development

A Penning-type ion source (hereafter referred to as the Berkeley Lab Penning source, or BLP source) was developed in the Ion Beam Technology Group at Lawrence Berkeley National Laboratory with the express purpose of investigating various methods for improvement of the extracted ion current density and atomic ion fraction obtained from the Penning discharge. A schematic of the basic BLP source is shown in Figure 2.3. Photos of the source components are shown in Figure 2.4. The main source body is aluminum, with additional extension pieces of both aluminum and stainless steel available to accommodate various components for testing. The working gas is introduced into the discharge chamber volume through a feed-through in the stainless

steel source backplate and an aperture in the cathode opposite the extraction aperture. An additional feed-through allows for measurement of the gas pressure at the gas inlet. The discharge chamber volume is determined by the length of the annular anode and positions of the cathodes; in the basic BLP source, the cylindrical discharge volume is 2.54 cm in length and 2.54 cm in diameter. The basic BLP source features aluminum electrodes (both cathodes and anode). The cathodes sit at the source body potential. The discharge voltage is thus applied between the anode and the source body by way of a spring-loaded electrical feed-through in the side of the source body. The anode is electrically isolated from the source body with ceramic and plastic insulators. The extraction plate is interchangeable; the nominal extraction plate is magnetic steel, with an extraction aperture diameter of 2 mm. The axial magnetic field is applied with an electromagnet capable of supplying magnetic field strengths up to 700 G. The BLP source is modular in nature such that the various source components can be disassembled and replaced to create different configurations.

2.3.1 Basic BLP source performance

Basic BLP source performance was characterized by varying the axial magnetic field and discharge voltage and measuring the extracted ion current and atomic ion fraction. The basic BLP source was typically operated with a constant hydrogen gas pressure as measured at the gas inlet of 0.8 mTorr.

A schematic of the experimental test stand apparatus used in the characterization of the BLP source is shown in Figure 2.5. The test stand features a Faraday cup with electron suppression capabilities for measuring total extracted ion current, as well as a sector magnet and second Faraday cup for measurement of the mass spectra of ions in the extracted beam. The ion source components are floated at high voltage, while all measurement apparatuses are electrically isolated from the grounded vacuum chamber and accessible during ion source operation.

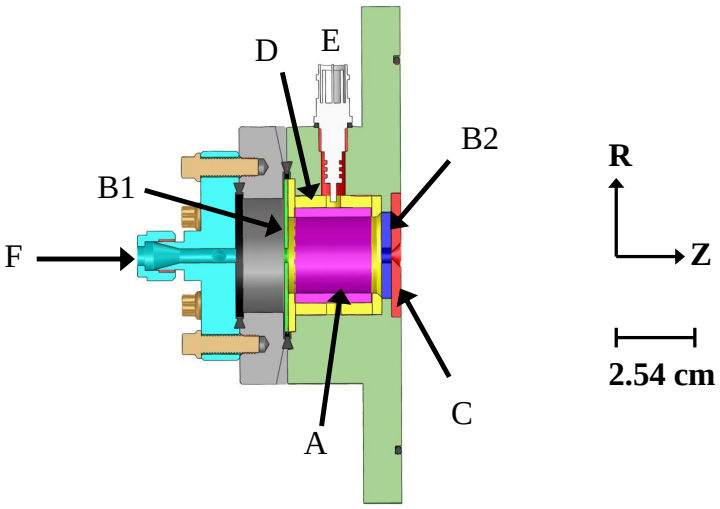

A–Anode
B1–Backplate cathode
B2–Cathode shield
C–Extraction aperture
D–Insulator
E–Electrical feed-through
F–Gas inlet

Figure 2.3: Schematic of Berkeley Lab Penning source. The basic configuration features a 2.54 cm diameter x 2.54 cm long cylindrical discharge region.

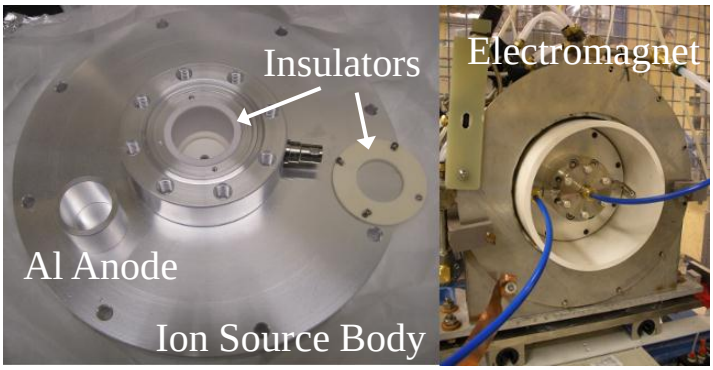

Figure 2.4: (Left) BLP source components dissassembled. (Right) BLP source assembled at test stand.

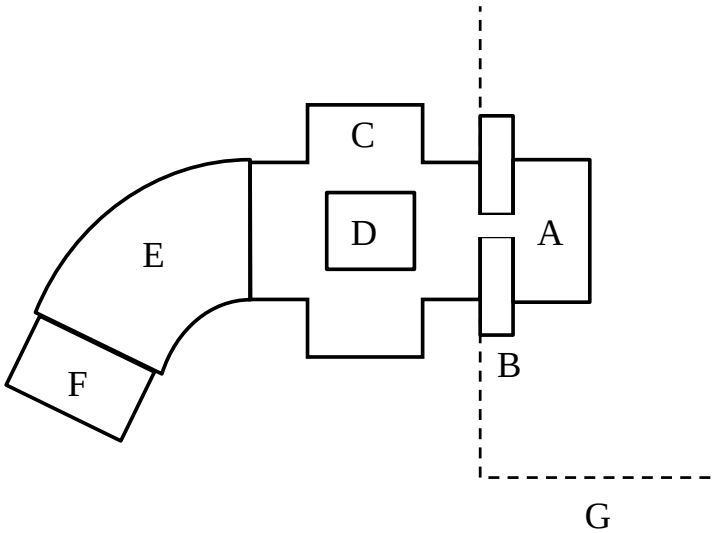

A–Ion source components
B–High voltage insulator + extraction electrode
C–Vacuum chamber
D–Faraday cup 1
E–Sector magnet for mass analysis
F–Faraday cup 2
G–High voltage cage area

Figure 2.5: Schematic of experimental test stand apparatus. Faraday cup 1 is retractable and can be moved out of the line of sight of the extracted ion beam.

BLP source magnetic field dependence

Figure 2.6 shows the discharge current as a function of magnetic field for the basic BLP source with fixed anode voltage of 800 V. The extracted ion current collected at Faraday cup 1 was measured across a sensing resistor and is plotted on an arbitrary scale in the same figure. The discharge current generally increases with increasing axial magnetic field until a transition magnetic field value is reached, after which the discharge current gradually decreases with increasing magnetic field. Under these operating conditions, the transition occurs near 350 G, with the discharge current reaching a maximum of 7.4 mA; similar trends were observed for anode voltage of 600 V. For low magnetic field values, it is noted that the discharge became unstable, resulting in swings in both the discharge and extracted ion currents. The extracted ion current decreases with increasing magnetic field. Though higher magnetic fields have little effect on the extracted ion current, the extracted ion current generally follows the trend of the discharge current. This indicates that in the high magnetic field regime past the transition point under these operating conditions, the increased axial field does not result in a measurable increase in the plasma density. It is noted here that the transition magnetic field was observed to shift to higher values with increased anode voltage.

Mass spectra of the ions in the extracted ion beam were obtained for the various hydrogen discharge conditions. Mass spectra for discharges with constant pressure of 0.8 mTorr, applied anode voltage of 600 V, and applied axial magnetic field values between 200-500 G are plotted in Figure 2.7. Diatomic hydrogen H_2^+ ions dominate, typically comprising about 90% of the hydrogen species in the beam. The measured proton fraction typically falls within the range of 5-10%, showing some variation with the variation in the axial magnetic field. These spectra indicate that the maximum discharge current and maximum proton fraction are typically not obtained under similar operating conditions, i.e. at the same axial magnetic field, though the variation of the proton fraction is small compared to the discharge current variation over the range of magnetic field studied.

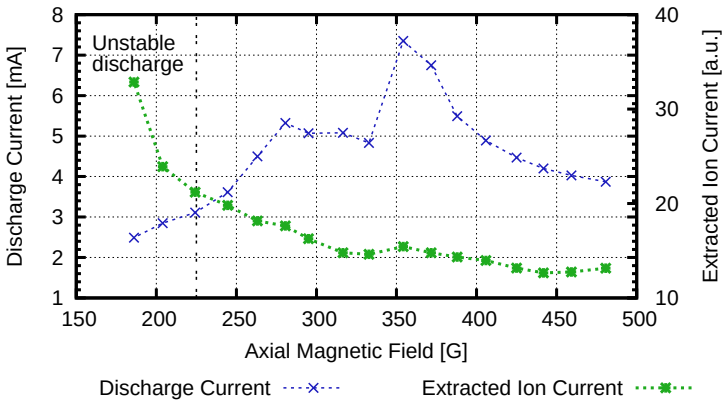

Figure 2.6: Discharge current and extracted ion current dependence on axial magnetic field for BLP source operation with 800 V anode voltage, 0.8 mT source pressure, and operation with Al electrodes. The extraction voltage is 5 kV. The discharge current gradually decreases after the transition point near 350 G. The axial magnetic field has little effect on the extracted ion current for high field values under these discharge conditions.

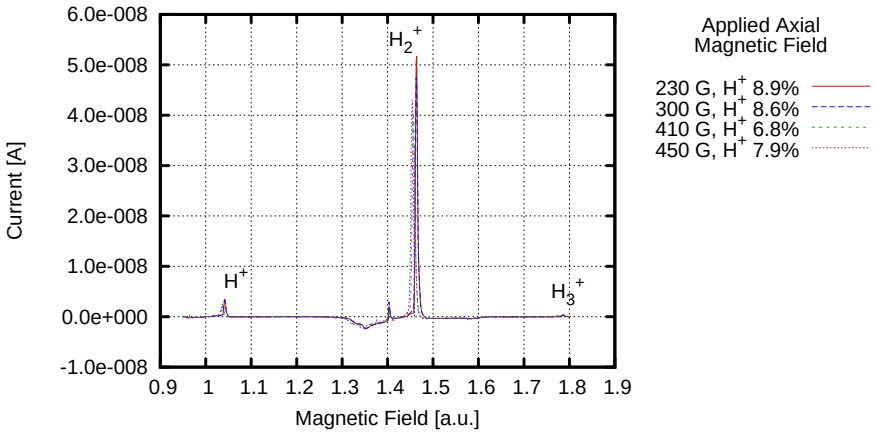

Figure 2.7: Mass spectra for varying axial magnetic field in the basic BLP source under constant pressure (0.8 mT) and anode voltage (600 V). The relative proton fractions are listed in the figure key. The proton fraction varies with the applied axial magnetic field, but typically falls in the range of 5-10%.

BLP source typical operating parameters

Table 2.2 summarizes the typical operating parameters for the basic BLP source. After characterization of the basic BLP source operation, methods for improving the source performance were investigated to increase the viability of the BLP source for neutron generator applications. Methods for boosting the source performance focused on increasing the electron density in the discharge through various methods described in the following sections.

Table 2.2: Basic BLP source operating parameters.

Pressure	$0.8 - 1.0$ mTorr
Anode voltage	$600 - 800$ V
Axial magnetic field	$300 - 400$ G
Discharge current	$3 - 4$ mA
Electrode material	Aluminum
Anode length	2.54 cm
Anode inner diameter	2.54 cm
Discharge volume	12.9 cm^3

2.3.2 Variation of electrode materials

Plasma interactions with the electrode surfaces comprising the discharge chamber walls affect both the atomic ion fraction of extracted beam ions and the discharge current, and, subsequently, the extracted ion current. Because a major mechanism by which the Penning discharge is sustained is the secondary electron emission from ion impact on the two cathodes, the use of various electrode materials that are subjected to this ion impact will yield different source operating characteristics. While extensive data exists for secondary electron emission under electron impact, secondary electron emission data under ion bombardment remains incomplete even for simple ion species such as protons, with much of the available data on proton and H_2^+ bombardment on metallic targets compiled in the 1960s–70s for incident

energies in the keV-MeV range [29], [30], [31]. Figure 2.8 (adapted from [29]) shows the velocity dependence of the secondary electron emission coefficient for bombardment of clean aluminum surfaces by low energy light ions. The minimum velocities correspond to incident ion energies of 2 keV. The secondary electron yields under proton/deuteron and H_2^+/D_2^+ bombardment for these energies/velocities fall within the range of 0.1-0.2 electrons per incident atom. The secondary electron emission coefficient has also been observed to change with the oxidation of aluminum surfaces due to changes in the effective work function [32]; for bombardment of an oxidized aluminum surface with Ar^+ ions, the reduced work function results in increased secondary electron emission. That the secondary electron emission coefficient changes with changes in the work function of a given material motivates the investigation of different electrode materials for use within the BLP source.

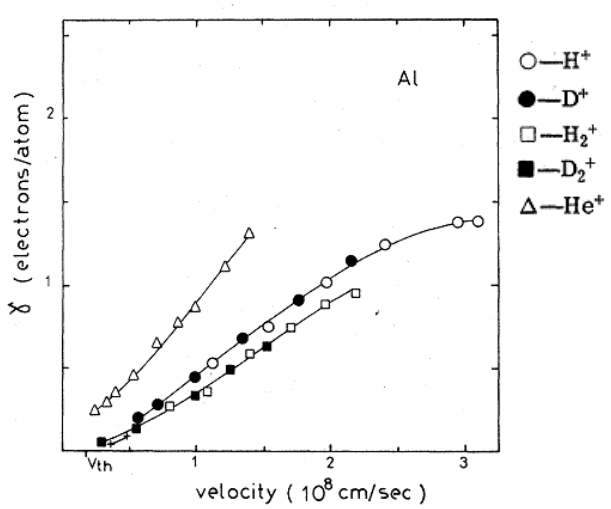

Figure 2.8: Secondary electron emission yields for various incident ion species.

The effects of electrodes fabricated from molybdenum, graphite, gold, and platinum on the discharge current, extracted ion current, and atomic ion fraction were measured and compared with the basic BLP source performance utilizing aluminum electrodes. The work functions of the materials investigated are listed in Table 2.3; experimental work performed for bombardment

Table 2.3: Material work functions (ϕ) and secondary electron emission coefficients (γ) under molecular hydrogen ion bombardment.

Material	ϕ [eV]	γ for 2 keV H_2^+ ions [e^-/atom]
Aluminum	4.17	0.087
Molybdenum	4.57	0.175
Gold	5.38	0.119
Graphite	4.83	−−
Platinum	5.55	−−
Boron Nitride	6.00	−−

Data from [34], [29], [35], [36], [37], [38], [39].

of platinum and carbon (graphite) foils (as well as several other target materials) by H^+/D^+ and H_2^+/D_2^+ ions demonstrate increased secondary electron emission with increasing work function of the target material [33], in contrast with the previously cited increased secondary emission observed with decreases in the work function of a single material. Table 2.3 also lists the secondary electron emission coefficient under bombardment by 2 keV H_2^+ ions for several materials, where available.

For each material test, the aluminum electrodes of the basic BLP source were replaced with cathode shields and an annular anode of the respective material. Figure 2.9 shows annular anodes of the materials tested for comparison with the basic BLP source. The molybdenum and graphite anodes were machined as single pieces. Gold and platinum electrodes were fabricated by coating the plasma-facing surfaces of base aluminum electrode pieces with films of the respective material in a vacuum deposition process. The base aluminum electrode pieces were first coated with a 150 Å thick layer of chromium for improved adhesion between the deposited film and the aluminum substrate. The nominal deposited film thickness for both gold and platinum electrodes is 1 μm. Figure 2.10 shows half-anode pieces within the deposition chamber after gold plating.

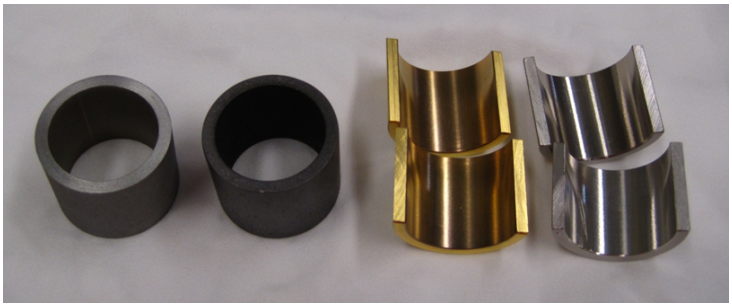

Figure 2.9: Molybdenum, graphite, gold, platinum anode pieces.

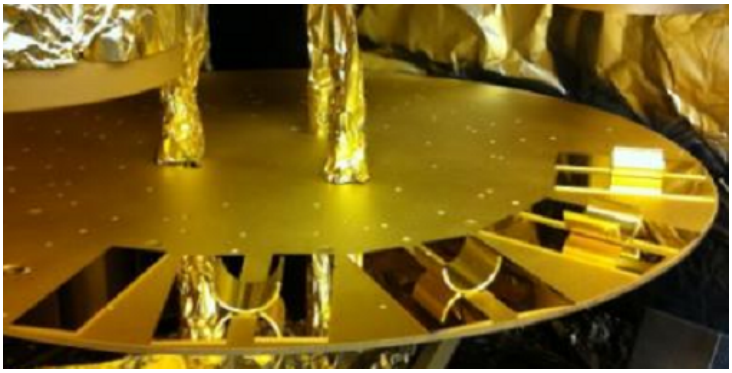

Figure 2.10: Gold anode pieces in deposition chamber. The half-anode pieces are supported by witness foils that serve as monitors of the deposition process.

The effects of boron nitride on the discharge properties in the BLP source were also observed by shielding one cathode from the discharge with a layer of boron nitride. Boron nitride has been shown to enhance the proton fraction in hydrogen discharges due to its low hydrogen recombination coefficient [40]. The 2 mm thick boron nitride layer was incorporated into the basic BLP source, shielding the cathode opposite the extraction aperture from the discharge. The insertion of the boron nitride layer results in an asymmetric electric field distribution and subsequent asymmetric discharge; ions incident on the boron nitride layer can cause the boron nitride surface to charge up, affecting the plasma sheath formation near this surface. Secondary electron emission from the boron nitride layer can further alter the potential distribution.

Experimental results

Figure 2.11 compares the extracted ion current density for basic BLP source operation with that of the various electrode materials, including the hybrid boron nitride-aluminum configuration. These data were obtained for similar source operating conditions of 0.8 mTorr hydrogen gas pressure, 800 V applied anode voltage, and 410 G applied axial magnetic field for all electrode materials, with the exception of the boron nitride case; operation with the boron nitride layer typically required higher source pressure of 1.1 mTorr and higher anode voltage of 1.1 kV to maintain stable discharge conditions. Under these discharge conditions, the discharge current for source operation with all electrode materials was lower than that for the basic BLP source operation. Conversely, the extracted ion currents plotted in Figure 2.11 indicate higher ion current densities from discharges utilizing electrode materials other than aluminum. The measured ion current density was observed to increase with increasing work function of the metallic electrode material.

Operation with gold and platinum electrodes resulted in as much as a factor of 2 increase in the ion current density over the basic BLP source operation. This indicates an electrode material-induced increase in the power efficiency of the source, as less power is required to generate comparable beam current densities. The power efficiency of the source, measured here in

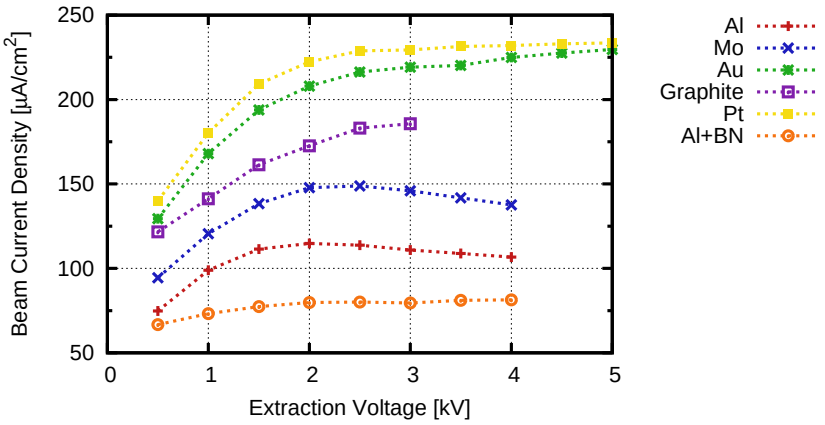

Figure 2.11: Ion beam current densities from BLP source operation with various electrode materials. Nearly all materials resulted in increased beam current density as compared to the basic BLP source utilizing aluminum electrodes.

units of current density per unit discharge power, is listed in Table 2.4 for the different electrode materials investigated and with ion current densities obtained with extraction voltage of 3 kV. The power efficiencies for molybdenum and platinum are comparable, as are those for gold and graphite. The increased power efficiency from discharges with molybdenum electrodes, however, is due to low discharge currents that result in smaller increases in the ion current density as compared to the other materials investigated. Operation with graphite electrodes was also found to be less than desirable, as the discharges with graphite electrodes were prone to instabilities resulting from outgassing of the electrode surfaces.

Similar to operation with the graphite electrodes, source operation with the hybrid boron nitride-aluminum configuration required a period of outgassing before stable conditions were reached. The outgassing period was characterized by increased pressure within the discharge region and occasional discharge instability, as impurity species trapped within the porous boron nitride layer were liberated by substrate heating due to plasma exposure. This outgassing period typically occurred over several hours, during which the source pressure gradually decreased to pre-outgas values and the

Table 2.4: Power efficiency for BLP source operation with different electrode materials.

Material	Power efficiency $[\frac{\text{mA}}{\text{cm}^2 \cdot \text{W}}]$
Aluminum	0.035
Molybdenum	0.072
Gold	0.093
Graphite	0.093
Platinum	0.079

intensity of impurity species as measured by the mass analyzing sector magnet decreased. The discharge current for source operation with the hybrid boron nitride-aluminum configuration was much lower than for operation with pure metallic electrodes, typically less than 1 mA; this is likely due to the asymmetric discharge induced by the obstruction of the cathode opposite the extraction aperture. This asymmetric discharge also results in reduced ion current density, seen in Figure 2.11.

Figure 2.12 compares the fraction of atomic ions in the extracted beam for hydrogen discharge operation with the various electrode materials. As expected, the presence of the boron nitride layer increases the proton fraction; the resultant proton fraction is increased by over a factor of 2 as compared to operation with all aluminum electrodes. While the use of molybdenum electrodes typically results in a slight decrease in the proton fraction, all other materials tested tend to result in increased proton fraction. The increased proton fraction observed for operation with these electrode materials results in values that are still characteristic of Penning-type discharges; the 16% proton fraction measured due to the presence of boron nitride within the discharge is still well within the range of expected proton fraction values.

Because the sustenance of Penning-type discharges relies on the secondary electron emission upon ion impact at the two cathodes, sputtering of the cathode material has implications on the performance of the BLP source. Optimum performance is achieved with the use of the coated gold or plat-

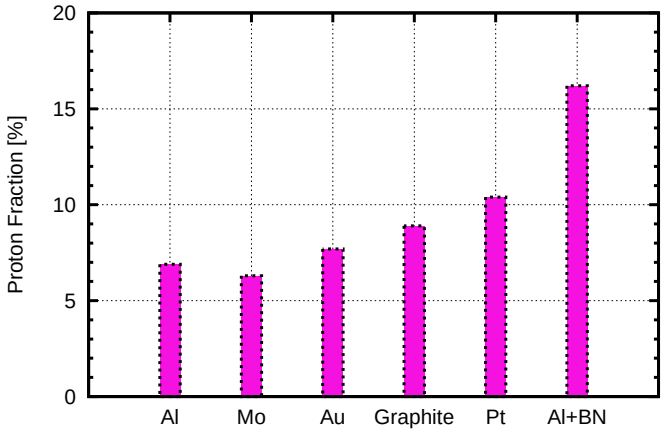

Figure 2.12: Proton fraction in extracted ion beams from hydrogen discharges for BLP source operation with various electrode materials. The plasma interactions with boron nitride result in a factor of two increase in the proton fraction over basic BLP source operation.

inum electrodes, and sputtering through the coating material to the base material will result in a substantial degradation in the source performance. The lifetime of the coated electrodes has not yet been tested, but the modular nature of the BLP source allows for easy replacement electrodes that have reached the end of their useful lifetimes.

While specific plasma-wall interaction processes cannot be directly measured within the BLP source, it is apparent that the material properties and the resultant physical and chemical surface interactions directly affect the plasma properties and quality of the extracted ion beam. That the ion current density from the BLP source increases with increasing electrode material work function demonstrates the importance of material selection while motivating further understanding of the processes at play. The source discharge current generally gives a first indication of the relative magnitude of the plasma density, but source operation with the various electrode materials was found to result in reduced discharge current compared to the basic BLP source. It is possible that the increased secondary emission from the different material surfaces results in electron currents that effectively cancel

out electron loss currents at the anode, resulting in a reduction in the measured discharge current but overall increase in the plasma density. That the material properties effect this aspect of the source performance is evident, but further work is necessary to understand the relative importance of the complex processes involved in plasma-surface interactions in the presence of electromagnetic fields.

2.3.3 Elongated discharge volume effects

The basic BLP source was fabricated with the ability to accommodate an extension piece that effectively increases the discharge volume by 60%, allowing for the effects of the larger discharge volume on the discharge current, extracted ion current, and atomic fraction to be measured. Elongated annular anodes 4.13 cm in length were used for this discharge; initial experiments used aluminum electrodes for comparison to the basic BLP source, with further experiments utilizing gold and platinum electrodes in the elongated source (see section 2.3.5).

Experimental results

Figure 2.13 compares the extracted ion current density for the elongated anode discharge and the basic BLP discharge. The use of the elongated anode and subsequent elongated discharge volume resulted in 30% less discharge current under similar operating conditions of 800 V applied anode voltage, 0.8 mTorr source pressure, and 410 G applied axial magnetic field. The resultant extracted ion current, however, increased by a factor of 3. This trend opposes that seen by Guharay [41], where increasing the discharge volume by 25%, also through increased anode length, resulted in increases in both discharge and extracted ion currents by a factor of 2.

The increased length of the discharge volume allows those electrons oscillating between the two cathodes to undergo more ionizing collision events with neutral gas species for each pass through the discharge volume. For fixed anode voltage, pressure, and axial magnetic field, however, it is noted that the plasma density itself may not be increased with the increased discharge volume; a constant plasma density with fixed operating parameters results in

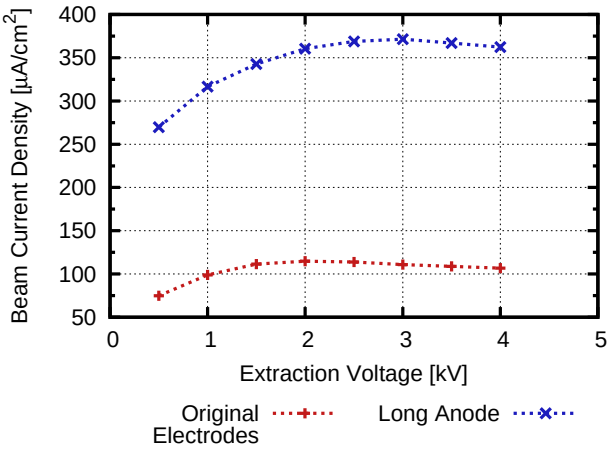

Figure 2.13: Ion current density for basic BLP source operation and BLP source operation with elongated discharge volume. Increasing the discharge volume by 60% resulted in an increase in the ion current density by a factor of 3.

greater total electron and ion yields for an elongated discharge volume. The increased number of ions available for extraction can explain the increased extracted ion current observed with elongated source operation.

The elongated discharge volume was found to have no effect on the atomic ion fraction. This lends evidence to the lack of increased plasma density within the elongated discharge volume, as the atomic ion fraction from these two discharges utilizing aluminum electrodes are consistent for similar operating conditions.

2.3.4 Electron injection from field emitter arrays

Preliminary investigations of the effects of electron injection from field emitter arrays directly into the BLP discharge were performed. The principal of electron injection into Penning-type discharges has been established with the incorporation of filaments for thermionic emission into the Penning source discharge chamber [42], a configuration known as a hot cathode Penning source. The use of field emitter arrays here aims to accomplish electron emission and injection into the Penning-type discharge through electron field

emission, which can occur with substantially lower power consumption as compared to thermionic emission. The electron injection is accomplished by the emission of electrons from the emitter array in the presence of a high electric field. Electron field emission typically requires field gradients on the order of 1 volt per nanometer. Electric fields of this order of magnitude are difficult to generate in typical laboratory settings, but the field emission can be enhanced by sharp structures on the material surface that act to locally compress electric field lines and increase the field gradient. The increased field gradient allows the bound electron to tunnel through the existing potential barrier to the surface of the bulk material. The field enhancement factor γ describes the amount of local field compression achieved at the surface of a sharp tip feature extending from the bulk material surface; the effective electric field is often enhanced by 2-3 orders of magnitude over the nominal applied electric field.

The electron emission current is dependent on the field emitter geometry and is given by the Fowler-Nordheim equation.

$$ln(\frac{I}{E^2}) = ln(\frac{aA}{\phi}\gamma^2) - \frac{b\phi^{1.5}}{\gamma E} \tag{2.3}$$

where

I: electron current
E: applied electric field
A: emitter area
γ: field enhancement factor
ϕ: material work function
a, b: material constants

It can be seen from the Fowler-Nordheim equation that the electron emission current is enhanced by both large emitter areas and large field enhancement factors. Because increasing the area of a single emitter reduces the effectiveness of the field enhancement due to less local compression of the electric field, arrays of sharp field emitters are used to effectively increase the emitter area. 1 cm x 1 cm arrays of carbon nanofibers fabricated in the

University of California, Berkeley Nanolab facilities were obtained for incorporation into the BLP source. The carbon nanofibers were grown on silicon substrates, with typical tip height and radius values of 5 μm and 30 nm, respectively. Typical tip spacing ranged between 10-30 μm. Figure 2.14 shows a scanning electron microscope image of a sample carbon nanofiber array [43]. The field enhancement factors of the carbon nanofiber arrays were characterized by measuring the electron current as a function of applied voltage and gap length; a typical I-V curve is shown in Figure 2.15. Field enhancement factors of 1000-2000 were measured for the tested carbon nanofiber arrays.

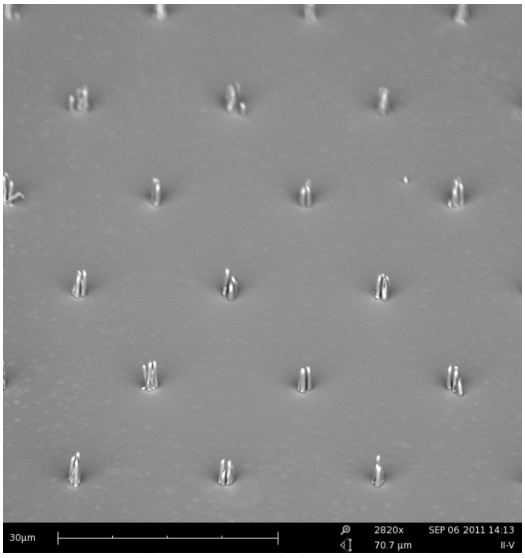

Figure 2.14: SEM image of carbon nanofiber array [43].

The carbon nanofiber arrays were then mounted within the BLP source for electron injection in the axial direction of the discharge. The carbon nanofiber arrays were mounted on the cathode surface opposite the extraction aperture such that the active surface of the array faces the discharge region. A schematic of the carbon nanofiber array setup within the BLP source is shown in Figure 2.16. The electric field required for field emission is applied between the cathode surface upon which the array is mounted and an electrically isolated grid positioned between the array active surface and the discharge region. Emitted electrons are thus accelerated beyond the grid into

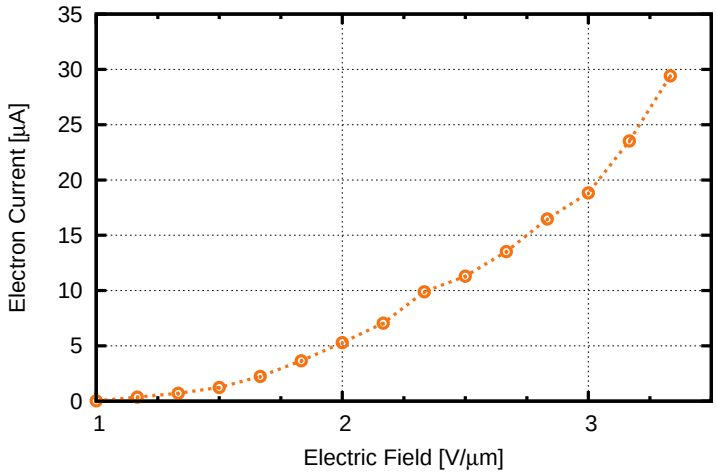

Figure 2.15: I-V curve for electron field emission from carbon nanofiber array.

the discharge region. The cathode surface upon which the carbon nanofiber arrays were mounted was biased at a negative potential, while the grid for field emission was electrically tied to the source body to approximate the original position of the backplate cathode; this biasing scheme was utilized to most closely approximate the basic BLP source condition and potential distribution within the discharge region in the absence of the field emitter arrays.

The emitted electron current from the carbon nanofiber arrays was measured with no plasma present to characterize the emission behavior within the BLP source. The distance between the carbon nanofiber array surface and the grid was approximately 300 μm, and electric field strengths up to 3.3 V/μm were applied to stimulate the electron field emission. The electron current was measured on the grid across a sensing resistor but was not monitored during experiments when the plasma was present.

Experimental results

BLP source operation with field emitter arrays present was characterized by reduced discharge current, by 50% or more depending on the discharge conditions; the effective surface area of the cathode available for ion bombardment

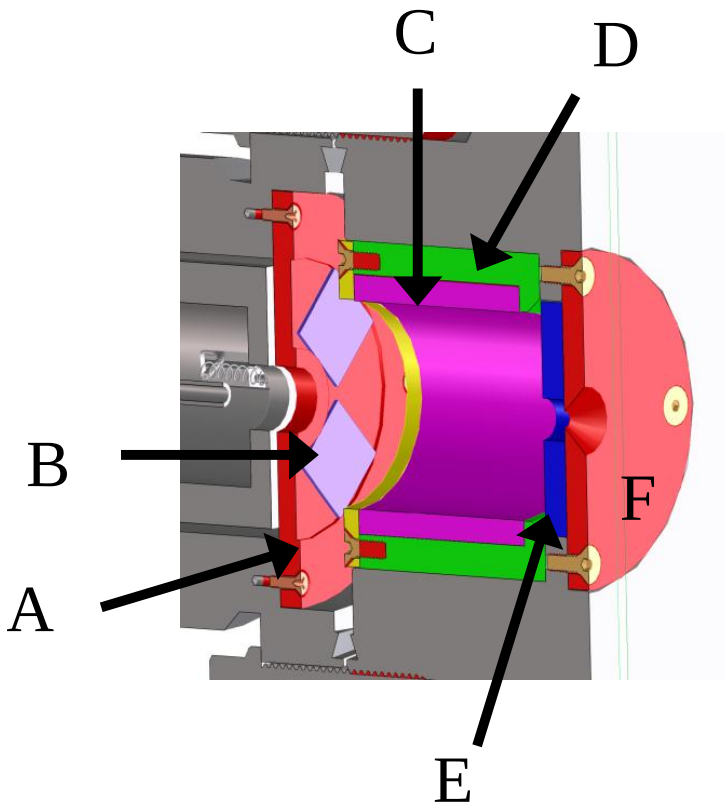

A–Backplate cathode	D–Insulator
B–Field emitter array	E–Cathode shield
C–Anode	F–Extraction aperture

Figure 2.16: Schematic of carbon nanofiber array setup within BLP source. The electric field required for electron field emission is applied between the backplate cathode and a grid (not shown) between the arrays and the discharge region.

and secondary electron emission is reduced by both the presence of the grid and the partial shielding by the carbon nanofiber array. A bias voltage was then applied to the backplate cathode with plasma present. The discharge current was observed to increase with increased bias voltage on the backplate cathode. Figure 2.17 shows the variation of the extracted ion current density with applied electric field on the field emitter array; these data were measured from a 0.8 mTorr, 400 V discharge with 230 G applied axial magnetic field. The extracted ion current density increases with increasing field on the carbon nanofiber array, but the extent to which electrons emitted from the carbon nanofiber array influence the discharge is inconclusive. A bias on the backplate cathode results in an asymmetric discharge that may also contribute to the increased ion current density; as the backplate cathode voltage is increased, ions that are not lost to the grid are accelerated into the backplate cathode (and field emitter array) with increasing energy. Secondary electrons emitted from the backplate cathode due to this ion bombardment are either lost to the grid or accelerated into the main discharge. The two distinct plasma regions on either side of the grid result in discharge instability as the magnitude of the voltage on the backplate cathode approaches the applied anode voltage.

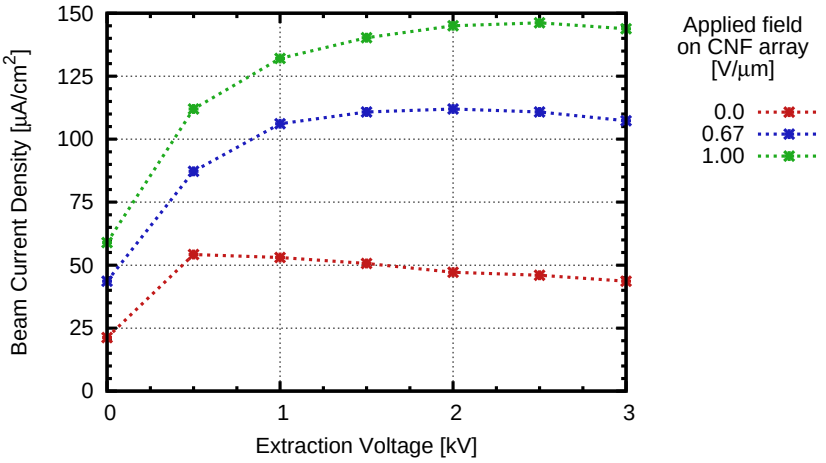

Figure 2.17: Extracted ion current variation with applied electric field on carbon nanofiber array.

The effect of the presumed electron injection into the BLP discharge on the proton fraction was measured. Figure 2.18 shows mass spectra for increasing applied electric field on the field emitter array. The total ion current measured beyond the mass analyzing sector magnet at Faraday cup 2 is increased with the increased applied field, corresponding to the increased extracted ion current density. Despite the increase in total current measured, the proton fraction remained constant for the three discharge conditions.

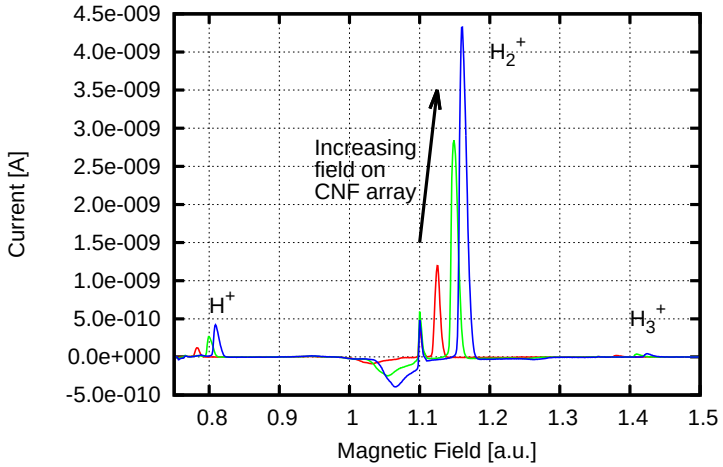

Figure 2.18: Mass spectra for discharges utilizing a carbon nanofiber array for electron field emission. The fraction of protons in the extracted ion beam is unchanged.

Efficient electron injection into and measurement of the effect on the BLP discharge remains a challenge. A meaningful comparison of the discharge characteristics with and without electron injection from a carbon nanofiber array is difficult to obtain with the experimental setup utilized here due to the asymmetry of the discharge and reduced cathode area. The microscopic nature of the carbon nanofiber field emitters may allow for minimal reduction in the effective cathode area through division of the field emitter array active area and strategic placement of the resultant smaller arrays. Such a scheme may also allow for less invasive methods for application of the fields required for the electron field emission. An additional challenge facing the field emitter arrays in a plasma environment is the degradation of the field emitter

tips due to plasma bombardment. The electron emission characteristics of the field emitter tips in the BLP source may degrade under ion bombardment due to etching and sputtering effects. Applying protective coating materials to the carbon nanofiber tips has been shown to protect the tips from extensive damage in a hydrogen plasma environment without degrading the field emission properties [44]; Penning-type discharges subject the field emitter tips to much harsher plasma environments than previously studied, and further work must be done to determine the effectiveness of such an approach.

2.3.5 Effects of multi-cusp magnetic confinement

Efforts to improve the performance of a Penning-type discharge focused on increasing the electron density within the plasma for overall increased plasma density and higher values of extractable ion current. This method involved two distinct approaches: creation and injection of additional electrons into the discharge, and increased lifetime of electrons already existing in the discharge through additional confinement schemes. The electrode material variation and use of field emitter arrays described in previous sections both aimed to increase the electron density within the BLP source. Electron confinement is already achieved to some extent within Penning-type discharges with the use of the axial magnetic field for increased electron path length. Further confinement was imposed upon the plasma species with the use of a multi-cusp magnetic field. Multi-cusp magnetic confinement has been shown to increase the plasma density for various ion source configurations by reducing electron losses to the conducting source chamber walls [45].

A permanent magnet multi-cusp magnetic field is generated using magnets of alternating magnetization direction. The magnetic field lines terminate on the poles, creating cusp structures in the resultant magnetic field. Figure 2.19 illustrates one such multi-cusp configuration and the resultant field lines; the alternating positions of the north and south magnet poles create a strong magnetic field near the magnet surfaces that decreases with distance from the multi-cusp magnets. Multi-cusp magnetic confinement of the plasma in an ion source is achieved by surrounding the ion source chamber with arrays of alternating magnets; a resultant multi-cusp field is shown

in Figure 2.20. The multi-cusp magnetic field extends into the discharge region, resulting in a strong transverse magnetic field component near the source chamber wall and a field-free region in the center of the discharge volume. Electrons approaching the chamber wall are generally deflected by the strong magnetic field to regions of weaker field; electron losses to the chamber wall thus occur on longer timescales, resulting in longer plasma confinement times.

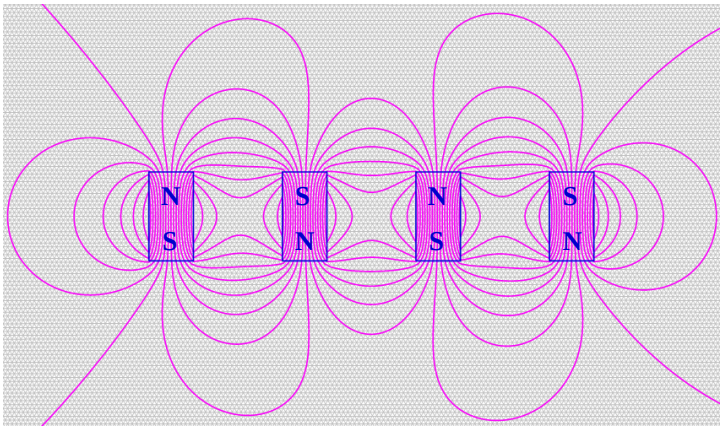

Figure 2.19: Simulated magnetic field lines for from magnets with alternating magnetization directions. The magnetic field lines terminate at the magnet poles, creating "cusps" in the resultant magnetic field.

For Penning-type discharges, the multi-cusp magnetic field is superimposed upon the existing axial magnetic field required to sustain the discharge. The multi-cusp magnets introduce a transverse component to the magnetic field distribution within the discharge volume. Two different multi-cusp magnet assemblies were tested with the BLP source to measure the effects of the anticipated increased plasma density on the BLP source performance. The multi-cusp magnet configurations differed in the directions of magnetization for a given row of magnets in the magnet array. Figure 2.21 illustrates the magnetization directions of the magnets used in the two configurations; configuration 1 features magnets that are magnetized along the axial direction of the BLP source, while configuration 2 features magnets that are magnetized

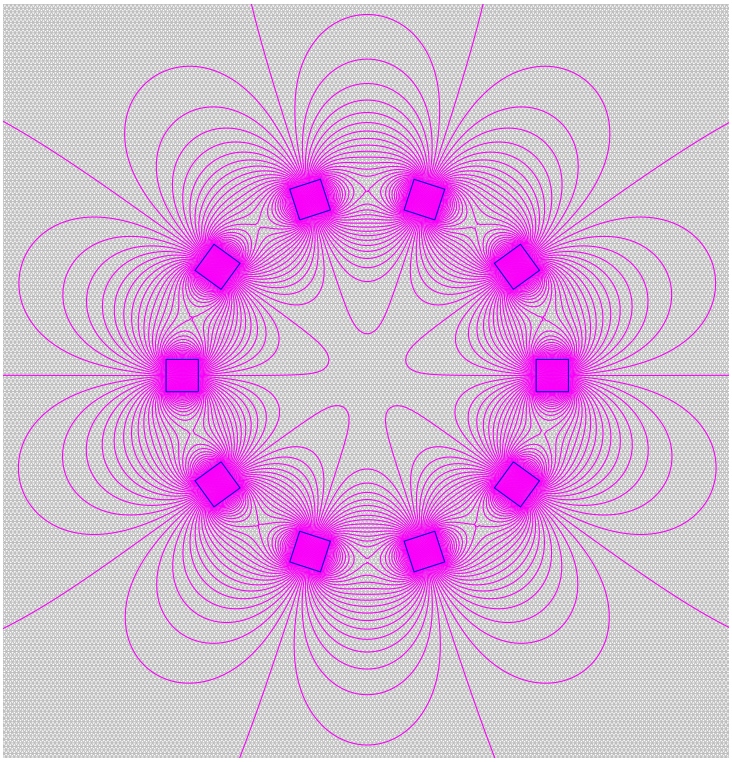

Figure 2.20: Simulated magnetic field lines for multi-cusp magnets arranged in a cylindrical pattern, as along the perimeter of a cylindrical ion source. The multi-cusp magnetic field extends into the discharge region.

along the radial direction of the BLP source. The multi-cusp field is created through the periodic arrangement of these magnets around the annular anode within the BLP source. Figure 2.22 shows a photo of a magnet array within the BLP source. The individual multi-cusp magnets are NdFeB permanent magnets, with 0.3175 cm x 0.3175 cm cross-sectional area and 0.635 cm length. The individual magnets are stacked such that the multi-cusp configuration spans the entire length of the anode, extending the multi-cusp field over the perimeter of the discharge region.

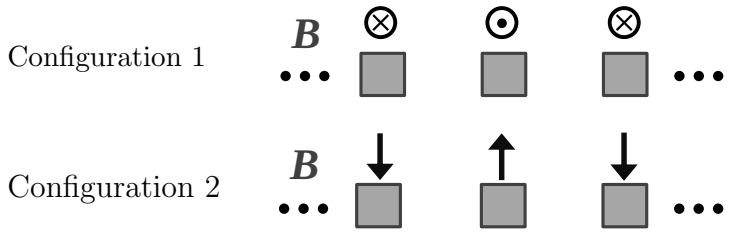

Figure 2.21: Magnetization directions of magnets in the simulated and tested multi-cusp magnet configurations. Configuration 1 features magnets that alternate magnetization direction along the axis of the BLP source. Configuration 2 features magnets that alternate magnetization in the radial direction of the BLP source.

Multi-cusp and total magnetic fields within the BLP source were simulated using the RADIA [46] simulation code for the two different multi-cusp magnet configurations. Figure 2.23 shows vector field plots of the resultant transverse magnetic field distribution within half of the discharge region for the two multi-cusp magnet configurations. Because the transverse field components do not affect the axial field required for the discharge, only the transverse component of the magnetic field is shown. The half cross-sectional areas within the BLP source are depicted at the ion source mid-plane and at the extraction plane, where ions are extracted. The magnetic field distributions are symmetric about the y-axis in the plots shown, and the origin denotes the ion source axis. It is seen from the vector field plots that the overall transverse magnetic field is stronger near the anode surface and drops

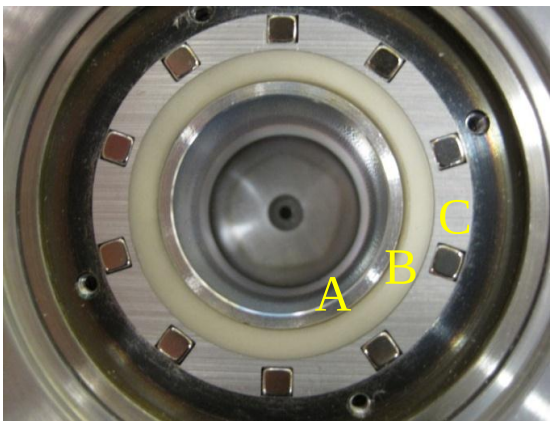

A–Anode
B–Anode insulator
C–Multi-cusp magnet array

Figure 2.22: Photo of multi-cusp magnets surrounding the cylindrical anode in the BLP source. The aluminum cathode shield and extraction aperture can be seen.

to nearly zero near the axis of the discharge region for both configurations. The magnitude of the multi-cusp magnetic field is stronger for configuration 2, as indicated by the lengths of the vectors in the vector field plots.

A different representation of the multi-cusp magnetic fields can be seen in Figure 2.24. Here, the magnitude of the transverse magnetic field is plotted throughout the three-dimensional discharge region. These plots indicate that the strong transverse components of the magnetic field generated by the multi-cusp magnets span the length of the discharge region for configuration 2 only; for configuration 1, these regions of stronger magnetic field are confined to the ends of the discharge region, near the cathodes. It can also be seen that the maximum transverse magnetic field for configuration 2 is nearly twice as strong as that of configuration 1. The two configurations were incorporated into the BLP source for comparison with basic BLP source operation and to observe the effects of the different transverse magnetic field magnitudes and structure on the BLP discharge.

Experimental results

BLP source performance with the incorporated multi-cusp magnetic fields was characterized by greatly reduced discharge current; the discharge current

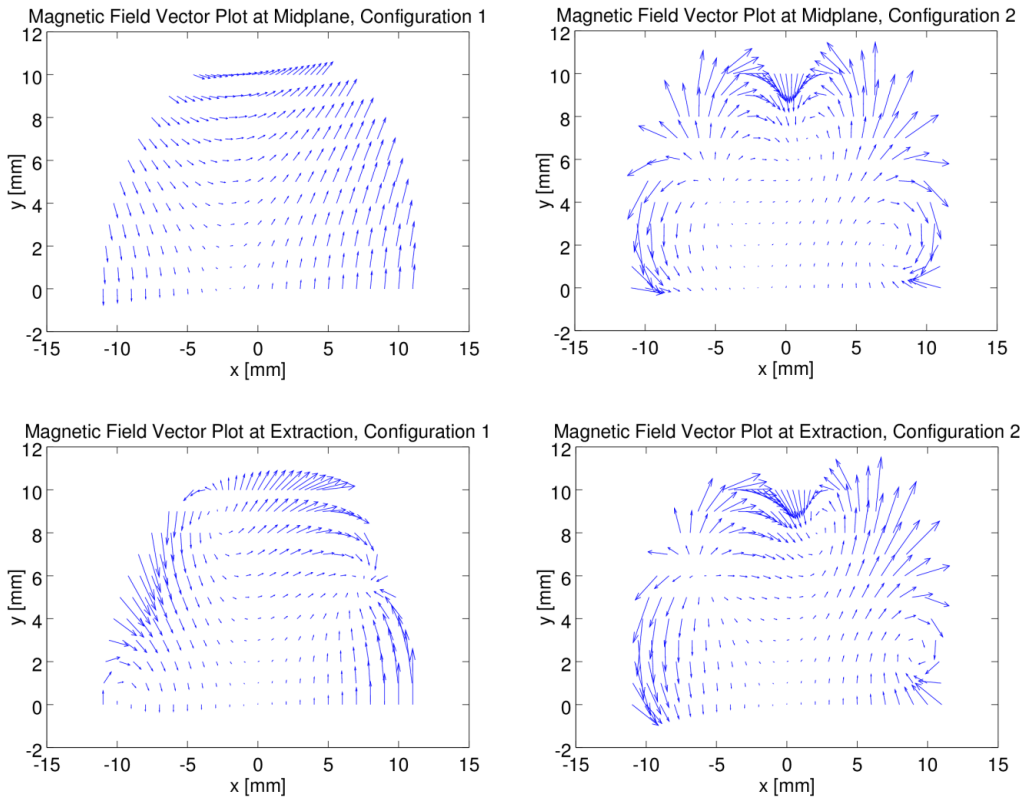

Figure 2.23: Simulated vector field plots for multi-cusp magnet configuration 1 (left) and configuration 2 (right). The transverse magnetic field vectors are plotted at the ion source mid-plane and extraction plane. In the extraction plane plots, the extraction aperture sits at the origin.

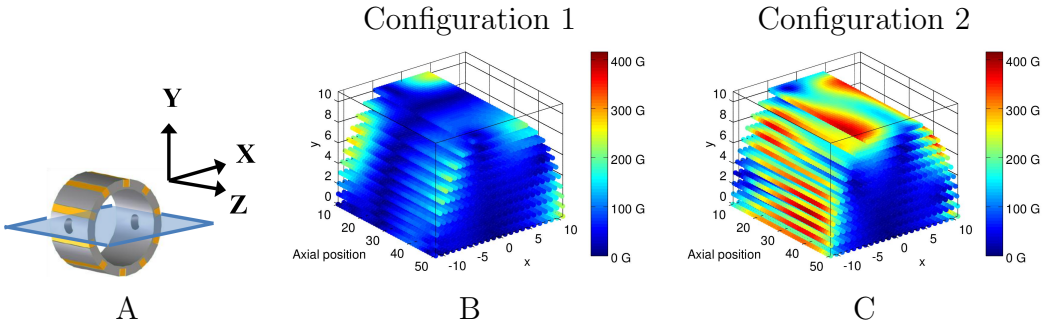

Figure 2.24: Magnetization directions of magnets in the simulated and tested multi-cusp magnet configurations. Configuration 1 features magnets that alternate magnetization direction along the axis of the BLP source. Configuration 2 features magnets that alternate magnetization in the radial direction of the BLP source.

for operation with multi-cusp magnet configuration 1 was typically 20-50% of that for the basic BLP source for similar pressure, axial magnetic field, and applied discharge voltage. Because one component of the discharge current in a Penning-type discharge is the electron loss current to the anode, the greatly reduced discharge current can be an indication of plasma confinement. Figure 2.25 compares the extracted ion current density for the basic BLP discharge and the BLP discharge utilizing multi-cusp magnet configuration 1. The addition of the multi-cusp magnetic confinement resulted in a factor of 3 increase in the extracted ion current density. Because the basic BLP source and BLP discharge using multi-cusp magnet configuration 1 utilize the same discharge volume and electrode material, the increased ion current density and drastic reduction in discharge current are both attributed to the reduced electron loss current to the anode. This is further supported by the discoloration present on the cathode shield near the extraction aperture due to plasma exposure as shown in Figure 2.22. The ion bombardment on the two cathodes leaves a discoloration pattern indicating that the plasma cross-sectional area does not extend to the anode cylinder; the plasma is confined to a smaller volume than that prescribed by the electrode surfaces. Because the elongated discharge volume was shown to result in increased extracted

ion density, multi-cusp magnet configuration 1 was also incorporated into the elongated BLP discharge; the resultant extracted ion current density is also shown in Figure 2.25. The combination of multi-cusp magnetic confinement and the elongated discharge volume resulted in a factor of 9 increase in the extracted ion current over basic BLP source operation; the effects of the elongated discharge volume and multi-cusp magnetic confinement are multiplicative for operation with aluminum electrodes.

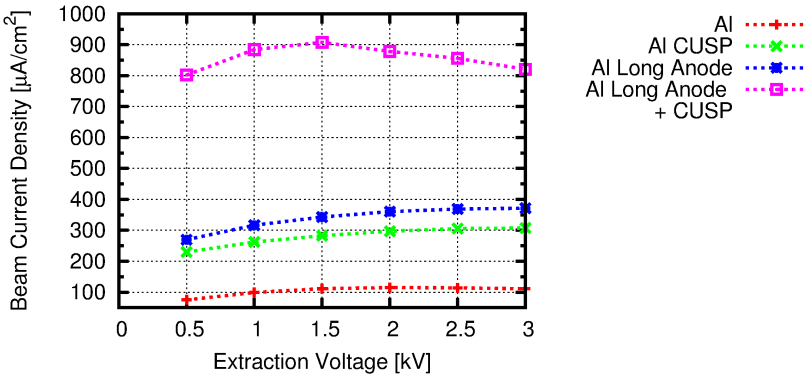

Figure 2.25: Comparison of extracted ion current densities for basic BLP source operation and the elongated BLP discharge both with and without multi-cusp magnetic confinement. Multi-cusp magnetic confinement of the plasma results in a factor of 3 increase in the extracted ion current density.

Figure 2.26 compares the extracted ion current density for operation with the two multi-cusp magnet configurations. It is noted here that these discharges utilized the elongated anode in combination with the multi-cusp magnets; the extracted ion current density for BLP source operation with the elongated anode is also plotted in Figure 2.26 for reference. Though the stronger multi-cusp magnetic field generated by the magnets of configuration 2 is expected to result in greater plasma confinement and thus higher plasma density as compared to operation with multi-cusp magnet configuration 1, the extracted ion current densities plotted in Figure 2.26 indicate that ion source performance is degraded by the stronger multi-cusp field. For source operation utilizing the elongated aluminum anode, the discharge cur-

rent from multi-cusp magnet configuration 1 is only slightly less than that without multi-cusp magnetic confinement. The use of multi-cusp magnet configuration 2 results in a 70% reduction in the discharge current compared to the nominal elongated anode case. Though the extracted ion current is still improved with the use of multi-cusp magnet configuration 2, the strong multi-cusp magnetic field reduces the effectiveness of the plasma confinement. The reduced extracted ion current density may be due to the reduced volume of the field-free region near the ion source axis; the stronger radial magnetic field may be reducing the effective surface area of the cathodes where secondary electrons are emitted, resulting in a weaker discharge and reduced plasma density.

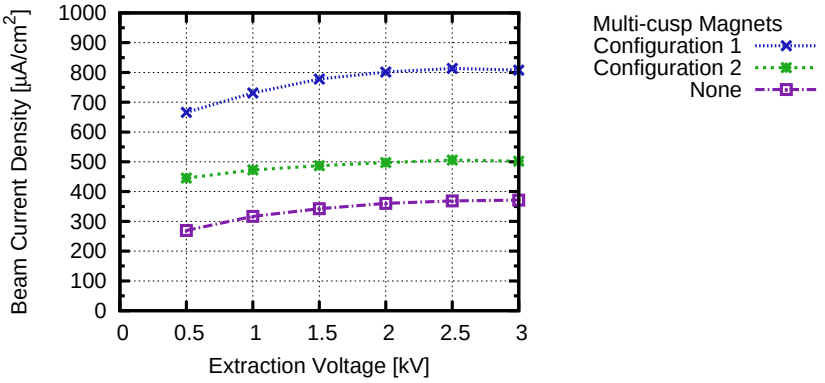

Figure 2.26: Comparison of extracted ion current densities for elongated BLP discharges utilizing the two multi-cusp magnet configurations.

The use of multi-cusp magnetic confinement has resulted in an increase in the BLP source extracted ion current density that is dependent on the strength of the multi-cusp magnetic field. Because the two multi-cusp magnet configurations utilized both resulted in improved ion current density, additional optimization of the multi-cusp magnet configuration may yet result in further improvements to the plasma confinement and ion current density. The two multi-cusp magnet configurations differed in both radial field structure and maximum radial field strength, and the relative importance of each component of the multi-cusp magnetic field to the plasma confinement and

resultant extractable ion current remains unknown.

2.3.6 Combined effects from electrode material variation, elongated discharge volume, and multi-cusp magnetic confinement

The modular nature of the BLP source allows for the combination of the various optimization paths investigated and the effects on the source performance to be observed. Each of the optimization paths explored acted to increase the extracted ion current density by factors of 2-3; the combinative nature of these methods was investigated in the effort to further increase the source performance. Initial results from combining the elongated discharge volume with multi-cusp magnetic confinement in the BLP source are shown in Figure 2.25, with the improved source performance prompting further testing with different electrode materials.

Figure 2.27 shows the extracted ion current densities obtained by utilizing multi-cusp magnetic confinement along with different electrode materials. Ion current densities from basic BLP source operation with and without multi-cusp magnetic confinement are also plotted for reference. All data were obtained using multi-cusp magnet configuration 1. Multi-cusp magnetic confinement acts to increase the extracted ion current density by about a factor of 2.

Figure 2.28 shows the extracted ion current densities obtained by combining aluminum and platinum electrodes with multi-cusp magnetic confinement in an elongated discharge volume environment. The use of the elongated discharge volume along with multi-cusp magnetic confinement in the BLP source with aluminum electrodes resulted in a factor of 9 improvement in the extracted ion current density over that from the basic BLP source; based on previous results from the variation of electrode materials, an additional factor of 2 improvement is expected from discharges utilizing platinum-coated electrodes. The measured data in Figure 2.28 indicate that the full factor of 2 increase is not realized. Because the full effect of the material variation relies on the plasma interaction with the electrode surfaces, it is possible that the presence of the multi-cusp magnetic field interferes with these interac-

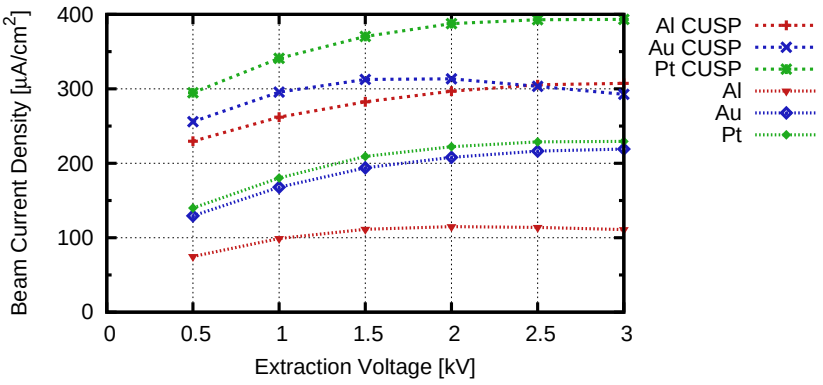

Figure 2.27: Comparison of extracted ion current densities for BLP discharges combining multi-cusp magnetic confinement with various electrode materials.

tions and the net increase in the plasma and/or extracted ion current density is less than expected. The proton fractions obtained from these discharges was consistent with the values expected as a result of the electrode material variation, as in Figure 2.12.

Because operation with any BLP source configuration was characterized by low power, low pressure discharges, the effects of increased source operating pressure on the discharge power and current, as well as the extracted ion current, were measured using the elongated anode along with multi-cusp magnetic confinement with aluminum, gold, and platinum electrodes, as these combinations previously resulted in the best source performance. Each source configuration was found to exhibit discharge instabilities as the hydrogen gas pressure was increased past a maximum value that varied with the electrode material. Typical maximum pressure values fell in the 2.0 mTorr range. The extracted ion current density was observed to increase linearly with the source pressure while the resultant discharge power tends to increase exponentially with the source pressure, as shown in Figure 2.29 and Figure 2.30. Maximum extracted ion current densities and the corresponding source operating parameters for the tested configurations are summarized in Table 2.5.

The maximum measured ion current density obtained from "high pressure" operation with aluminum electrodes, elongated anode, and multi-cusp

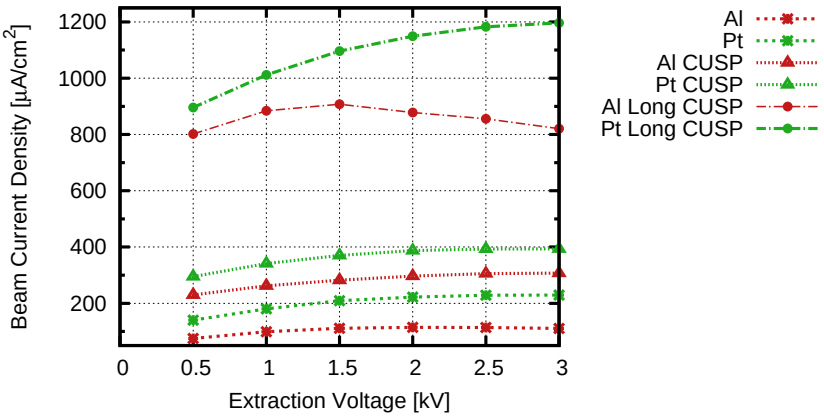

Figure 2.28: Comparison of extracted ion current densities for BLP discharges combining multi-cusp magnetic confinement with aluminum and platinum electrodes in an elongated discharge environment.

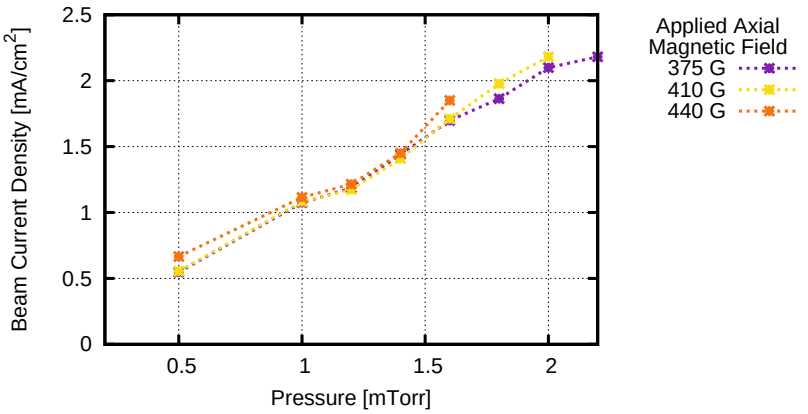

Figure 2.29: Extracted ion current density dependence on source operating pressure for gold electrodes with long anode and multi-cusp magnetic confinement. The applied anode voltage was 800 V. The extracted ion current density increases linearly the source operating pressure.

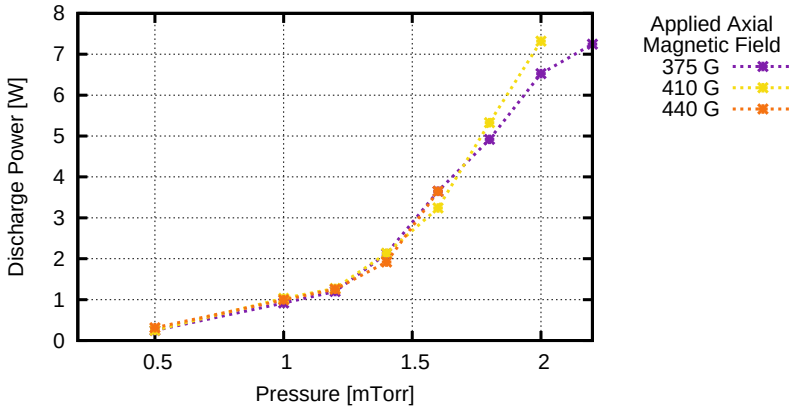

Figure 2.30: Discharge power dependence on source operating pressure for gold electrodes with long anode and multi-cusp magnetic confinement. The applied anode voltage was 800 V. The discharge power increases exponentially with the source operating pressure.

Table 2.5: Maximum extracted ion current density and corresponding operating parameters for operation with various electrode materials, elongated anode, and multi-cusp magnetic confinement.

Electrode material	Al	Au	Pt
Discharge voltage [V]	800	800	800
Axial magnetic field [G]	230	410	410
Pressure [mTorr]	1.6	2.0	1.8
Discharge power [W]	1.0	7.3	9.0
Ion current density $[\frac{\mathrm{mA}}{\mathrm{cm}^2}]$	1.3	2.2	2.0

magnetic confinement represents over a factor of 10 improvement over that from the basic BLP source. The use of gold or platinum electrodes in this configuration further improves the source performance by nearly a factor of 2. Though the discharge conditions under which these maximum values were obtained differed slightly with the different electrode materials, the maximum values nearly reflect the expected factor of 2 increase in the extracted ion current expected with the use of the coated electrodes.

2.4 Summary

The complex nature of plasma interactions within Penning-type ion sources warrants further study for better understanding of the processes involved and ways in which these processes can be exploited to improve the performance of such ion sources. The Berkeley Lab Penning source was designed and fabricated with the intent of investigating methods for improving the ion source performance through closer examination of the processes at play. The extent to which secondary electron emission under ion bombardment influences the extracted ion current density was taken advantage of with the use of different electrode materials for increased secondary electron emission. Electron losses to the anode were reduced through plasma confinement using permanent magnet-generated multi-cusp magnetic fields. The effects of increased discharge volume and electron injection into the discharge were also explored. Combinations of the various methods for source improvement resulted in an overall factor of 20 increase in the extracted ion current density as compared to the baseline source configuration. The methods employed provide valuable insight into approaches for further exploitation of the characteristics of Penning-type discharges and relevant processes for improved ion source performance and efficiency.

Chapter 3

Ion beam extraction and optics

3.1 Introduction

Ion beam extraction and ion optics relates to the extraction of ions from a plasma source and the transport of extracted ions to their final application. The ion beam extraction system is designed to impart desired characteristics to the resultant ion beam, largely utilizing electromagnetic fields to guide and shape the ion beam as it traverses the extraction system. Simulation programs aid in the design of the electrodes used to effectively accelerate the ion beam to the desired energy over the desired distances, and are invaluable in guiding the optimization of the transport and optics of the ion beam.

3.2 Ion beam formation

As was mentioned in the preceding section describing the Penning discharge, a discharge source becomes an ion source when features are introduced into the discharge chamber such that the ions generated within the plasma can be extracted and directed toward some final application. This is generally accomplished by introducing an aperture or multiple apertures in one surface of the discharge chamber. The ions are then easily extracted from within the plasma through the application of an electric field between the discharge chamber surface containing the extraction aperture, generally referred to as

the plasma electrode, and an external electrode. The external electrode is often referred to as the extraction electrode. Positive ions are extracted from the plasma with a net positive bias on the plasma electrode with respect to the extraction electrode; in a similar fashion, negative ions are extracted with a net negative bias on the plasma electrode. The continuous extraction of ions from the plasma results in a stream of ions from the plasma that can then be referred to as an ion beam. The plasma and extraction electrodes are shaped in such a way as to impart specific characteristics, i.e. beam diameter, divergence angle, etc., to the ion beam. A comprehensive discussion of ion extraction is given in [47].

3.2.1 Child-Langmuir law

The maximum transportable current between two planar conducting surfaces under the condition of space-charge limited emission is given by the Child-Langmuir law

$$J = \frac{4}{9}\varepsilon_0\sqrt{\frac{2q}{m}}\frac{V^{1.5}}{d^2} \tag{3.1}$$

where

J: Current density
q, m: Charge, mass of charged particle
V: Net voltage difference
d: Distance between surfaces

The maximum transportable current density is a function of the charged particle mass and charge state, as well as the net voltage and distance between the two conducting surfaces. The relevant case for an ion source extraction system requires an aperture through which the ions can be extracted from the plasma. The current is then also a function of the cross-sectional area through which the ions are extracted from the plasma. Figure 3.1 shows a schematic of a so-called diode extraction system, in which the ion extraction is accomplished using only two electrodes. In the figure shown, positive ions are extracted from the plasma, through the extraction aperture, by the

electric field between the plasma and extraction electrodes. Here, a voltage difference of 2 kV is applied between the two electrodes. The positive ions are accelerated into the extraction electrode by the electric field; the electrode at which the ion beam is lost is thus often referred to as a target or beam dump.

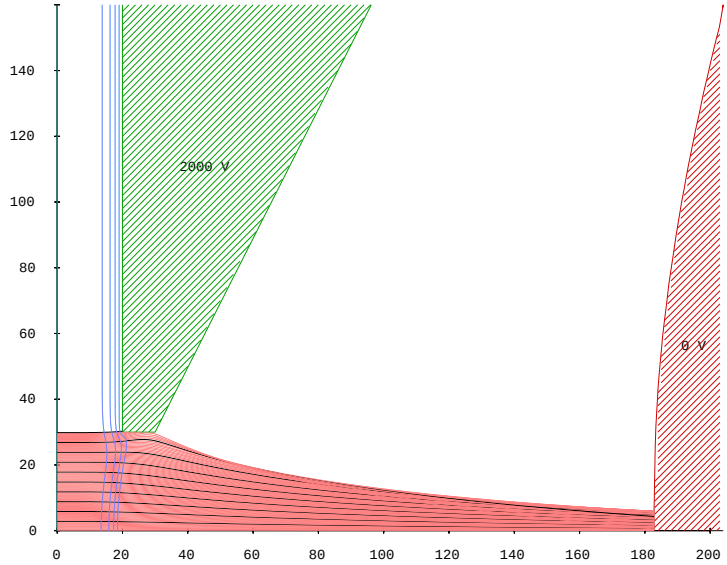

Figure 3.1: Ion beam extraction with diode extraction system. Two electrodes are used to accomplish the ion beam extraction. For positive ions, a negative field gradient is applied to draw ions out of the plasma.

The Child-Langmuir law allows for the definition of the perveance as

$$P = \frac{I}{V^{1.5}} \tag{3.2}$$

which relates the maximum extracted current to the applied voltage for the given extraction system. The perveance is constant for a fixed plasma density and fixed extraction system and thus provides a useful metric for predicting the ion beam behavior when certain parameters are changed.

3.2.2 Plasma meniscus formation

The equipotential surface between the bulk plasma within the discharge chamber and the vacuum region into which ions are extracted is referred to as the plasma meniscus. Additionally, a region exists between the bulk plasma itself and the plasma meniscus, known as the sheath, over which potential gradients exist to allow for the smooth transition between the bulk plasma at the plasma potential and the plasma electrode on high voltage. Ion extraction requires matching between the equipotential surfaces inside and outside of the plasma, and thus the plasma meniscus plays an important role in the ion beam formation and extraction characteristics. The shape of the plasma meniscus is determined by the interplay between the plasma density, the shapes of the plasma and extraction electrodes, the size of the extraction aperture, and the electric field induced by the applied extraction voltage. The shape of the plasma meniscus strongly influences the focal properties of the extracted ion beam and is thus especially important for diode extraction systems utilizing only two electrodes. Figure 3.2 illustrates the possible plasma meniscus shapes and the resultant ion trajectories in the extracted beam. In the ideal case, the plasma potential and potential induced by the extraction field create a flat plasma meniscus, resulting in parallel ion trajectories and a parallel beam. When the plasma density and extraction potential are not matched, the plasma meniscus protrudes into or recedes from the region of the extraction aperture. For a relatively high extraction potential with respect to the plasma density, the plasma meniscus is convex and protrudes into the region of the extraction aperture, resulting in a divergent ion beam. For a relatively low extraction potential with respect to the plasma density, the plasma meniscus is concave and recedes from the region of the extraction aperture, resulting in a convergent ion beam. The focal point of the ion beam, also known as the beam crossover point, varies in position based on the relative strengths of the plasma potential and extraction potential.

3.2.3 Beam emittance

The degree of convergence or divergence of charged particle beams is characterized by the beam emittance. The position and momentum of individ-

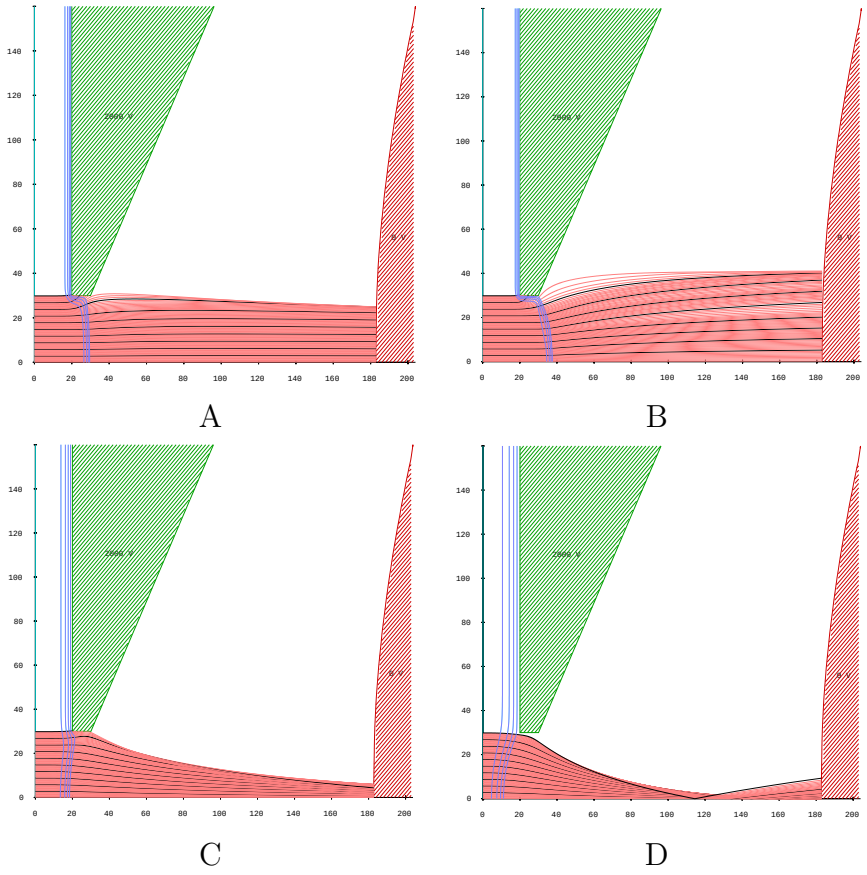

Figure 3.2: IGUN simulation of plasma meniscus shapes and effects on extracted ion beam. (A) The plasma meniscus is relatively flat, resulting in parallel ion trajectories. (B) The plasma meniscus is convex, and the ion beam is divergent. (C) The plasma meniscus is concave, and the ion beam is convergent. (D) The plasma meniscus is concave, but the focal point of the beam (beam crossover) is between the two electrodes, and the beam is then divergent.

ual particles in the beam can be mapped to a six-dimensional phase space (x-x', y-y', z-z'), and the emittance is effectively the phase space "volume" encompassed by the ensemble of beam particles. The emittance in each two-dimensional space is conserved when the electromagnetic forces acting on the particles are linear; the transverse emittance, the emittance in one direction (here, the x direction) transverse to the beam transport axis, satisfies the equation

$$\gamma x^2 + 2\alpha x x' + \beta x'^2 = \epsilon \tag{3.3}$$

where

x: Particle position
x': Particle angle
α, β, γ: Twiss parameters

The emittance is derived from the particle equations of motion, and it can be seen that equation 3.3 prescribes an ellipse of area ϵ in each two-dimensional phase space. The elliptical emittance pattern is often plotted in the x-x' phase space, in this case, and gives a visual representation of the degree of convergence or divergence of the beam. The constants α, β, γ are collectively referred to as the Twiss parameters and are derived from critical points on the plotted emittance ellipse. Figure 3.3 shows schematic and simulated emittance patterns that demonstrate the varying degrees of convergence of an ion beam. The different emittance patterns can be interpreted as follows: in the divergent beam case, particles with larger transverse positions within the beam also have larger beam angles, so as a particle's distance from the central axis of the beam increases, the particle moves away from the central axis faster and the beam diverges. The opposite is true of the convergent beam case; particles further from the central axis of the beam approach the central axis at a faster rate, and the beam extent in the transverse direction decreases as the beam advances in the axial direction. For the parallel beam case, the variation of beam angle with beam extent in the transverse direction is small; the ensemble of particles are transported with roughly the same beam angle over all positions within the beam. The focused beam case features a spread of beam angles with minimal extent in the

transverse direction. As mentioned earlier, the emittance is conserved when the electromagnetic forces acting on the particles are linear; in the graphical representation of the emittance, the area of the ellipse plotted in the two-dimensional phase space is constant. When nonlinear forces such as space charge effects are present, the elliptical representation of the beam becomes distorted, and the emittance is no longer strictly conserved. The area of the ellipse in phase space can thus grow under the influence of nonlinear forces.

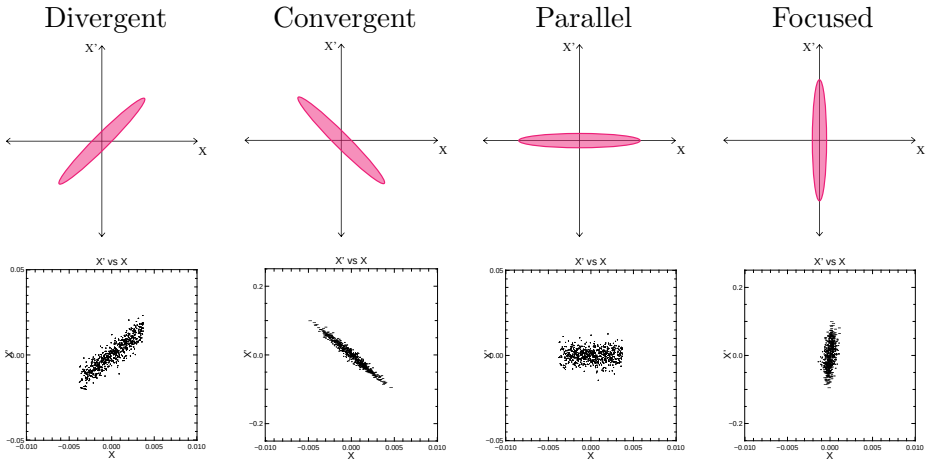

Figure 3.3: Schematic and simulated emittance patterns for the varying degrees of convergence of an ion beam.

3.3 Ion optics simulations

The design of an ion beam extraction and focusing system relies on the use of simulation programs that can take into account the various self-induced and applied electromagnetic fields present during beam extraction and transport. Numerous codes have been developed for ion beam extraction and ion optics simulations, utilizing different methods for solving Poisson's equation and the particle equations of motion to obtain self-consistent solutions for characteristics of the beam transport. The widely used codes IGUN [48] and PBGUNS [49] solve for the plasma meniscus by matching equipotentials inside and outside the plasma region and compute the resultant particle trajec-

tories for steady-state beam transport. IGUN self-adjusts the ion extraction current on successive iteration cycles, adjusting the Debye length within the plasma region until a self-consistent solution for the shape and location of the plasma meniscus is reached. PBGUNS utilizes a fine mesh region near the plasma emission surface, solving for the plasma meniscus equipotential by matching the particle trajectories and the resultant space charge density distribution on adjacent mesh positions until the solution converges. These codes have two-dimensional capabilities and are thus limited to the simulation of cylindrically symmetric or rectangular slit extraction geometries. The three-dimensional particle-in-cell code WARP3D [50] simulates particle trajectories by advancing individual particles in the simulation space over a user-defined time interval and calculating the resultant electromagnetic fields within the simulation space. Individual particles are tracked during the simulation, making extensive data on the particle position and momentum at each time step of the simulation available to the user. The nature of the code allows for the calculation of both time-dependent behavior as well as IGUN-like steady-state behavior of the beam. While WARP3D can handle much more complex problems and can provide much more information on the behavior of individual particles during beam transport, the code itself was created with beam transport through accelerator lattice components in mind, and is thus not optimized for ion beam extraction from a plasma.

The codes IGUN, PBGUNS, and WARP3D were utilized in simulating similar extraction geometries for comparison of the beam radius, maximum divergence angle, and ion current on target for a 100 keV atomic hydrogen (H^+) beam. The IGUN schematic of the electrode geometry is shown in Figure 3.4. In these simulations, atomic hydrogen ions were extracted through a 0.6 mm diameter aperture in the plasma electrode and accelerated to the target by the field applied between the plasma electrode and the electron suppression shroud. The extraction gap between the plasma electrode and the electron suppression shroud was varied between 20-30 mm, while the distance from the electron suppression shroud to the target was fixed at 25 mm. The plasma electrode was biased at positive 100 kV, the electron suppression shroud was biased at negative 1 kV, and the target was held at ground potential. The electron suppression shroud repels secondary electrons that are

emitted upon ion impact at the target, preventing those electrons from being accelerated back toward the plasma electrode. The beam trajectory is shown for each simulation program in Figure 3.5. The emittance plots for the ion beam at the target surface are shown for the three simulation programs in Figure 3.6. Comparisons of the beam radius and maximum divergence angle on target are shown in Figure 3.7.

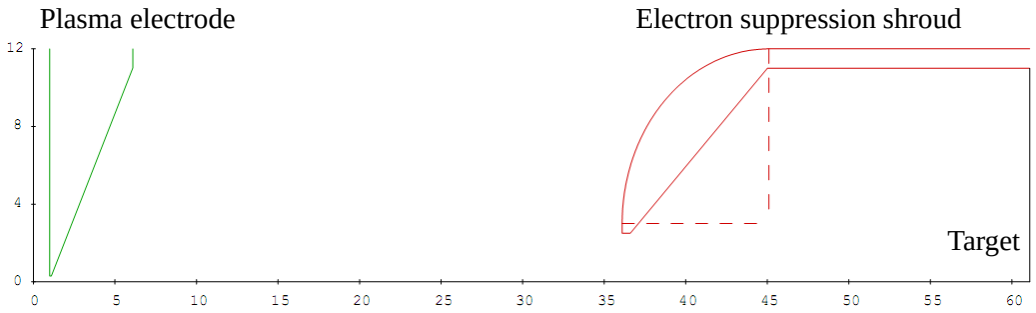

Figure 3.4: IGUN schematic of simulated electrode geometry. Beam acceleration occurs mainly between the plasma electrode, here biased at 100 kV, and the electron suppression shroud, here biased at -1 kV. The target is grounded and sits at the edge of the simulation region.

The three simulation programs show similar trends for both the beam radius and maximum divergence angle with varying extraction gap length; under these conditions, the plasma density is slightly weak in relation to the accelerating electric field, and the beam is overfocused. As the extraction gap decreases, the accelerating electric field becomes stronger, moving the beam crossover point closer to the plasma electrode and resulting in both larger beam diameters and larger maximum divergence angles at the target. The beam radius values are a better match between the simulation programs for shorter extraction gap lengths, with values diverging as the extraction gap length increases. The beam radius values obtained using WARP3D show less variation with the extraction gap length; because WARP3D is not optimized for ion beam extraction from a plasma, the method by which the beam is initiated in the WARP simulation impacts the final beam diameter. The maximum divergence angles obtained from the PBGUNS simulations

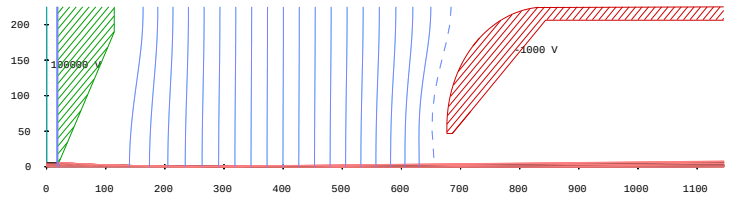

A

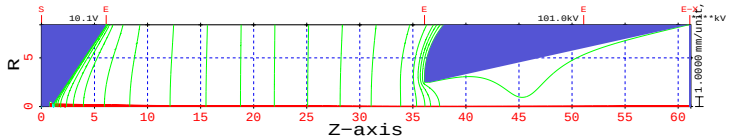

B

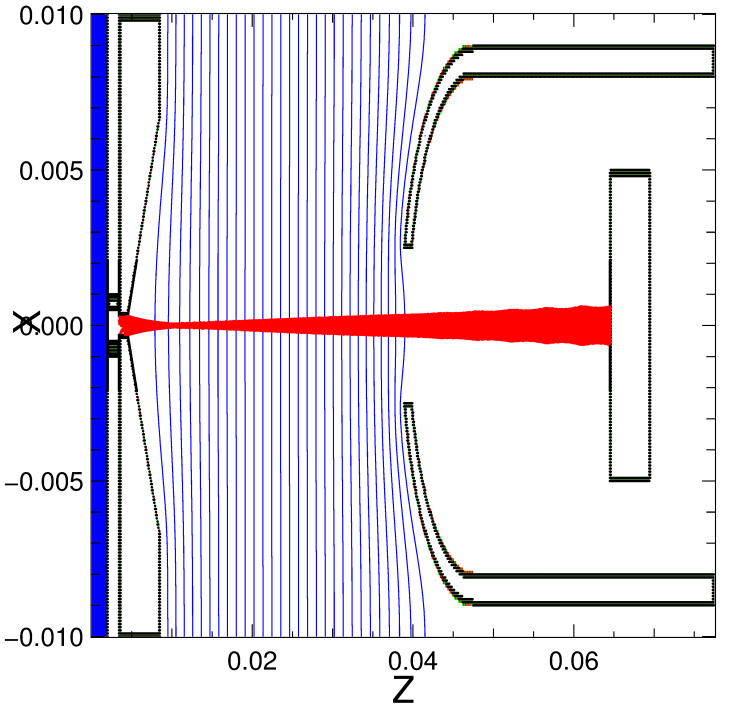

C

Figure 3.5: Beam trajectory comparison for the three simulation programs IGUN (A), PBGUNS (B), WARP3D (C). A 100 keV, 100 μA H^+ beam was simulated, with an extraction gap of 30 mm and shroud-to-target distance of 25 mm.

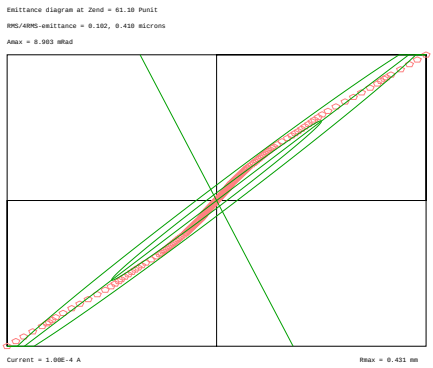

A

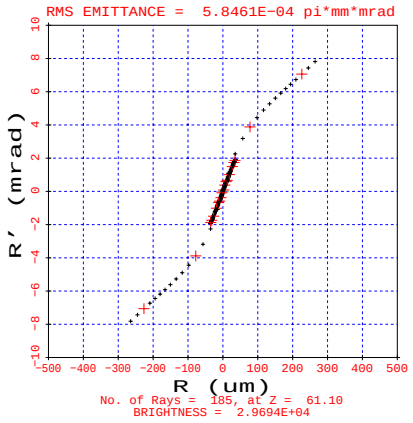

B

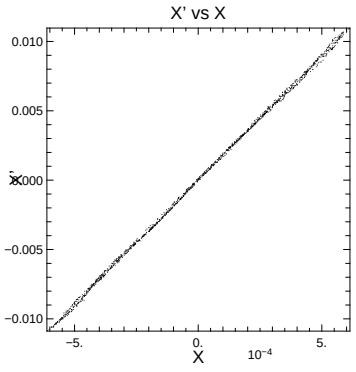

C

Figure 3.6: Beam emittance comparison for the three simulation programs IGUN (A), PBGUNS (B), WARP3D (C).

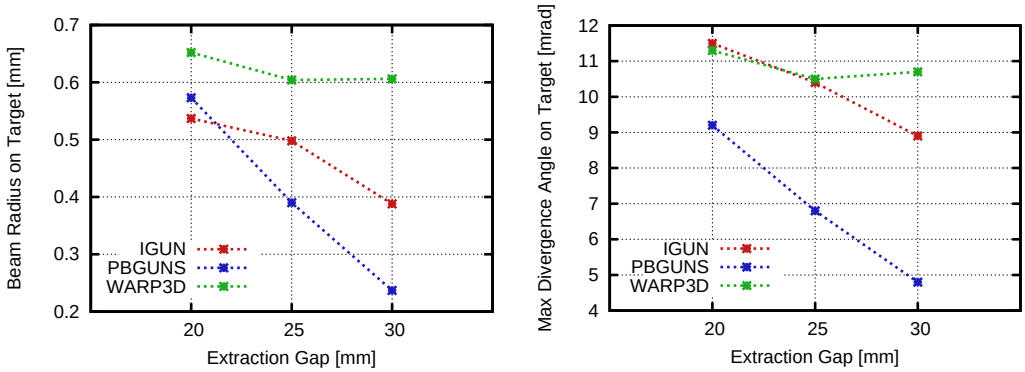

Figure 3.7: Beam radius (A) and maximum divergence angle (B) comparison for the three simulation programs IGUN, PBGUNS, WARP3D. Both the beam radius and maximum divergence angle are measured at the target plane.

are well below those values obtained with the other programs; it is noted that the beam ions were initiated with no angular spread (see simulations in section 3.4.1), which may explain the much smaller divergence angles obtained at the target. It is evident from these simulation results that proper plasma/beam initiation parameters for each simulation program are vital to obtaining meaningful results. Because there is such a variation in the beam radius at the target, comparison with experimental data provides the best indication of how closely each of the simulation programs approximate the experimental case.

Ion optics simulations are an important step in the design of an ion beam extraction and focusing system. Simulations give initial indications as to how the various components of the extraction system affect the properties of the beam transport and how parameters can be adjusted to achieve the desired design goals. The combination of simulation and experimental work is essential to the optimization of ion beam optics and focusing components.

3.4 Passive beam focusing methods

As the field of ion optics suggests, charged particle beams can be directed much as beams of light are directed with the use of lenses and other optical elements. Charged particle lenses often make use of the focusing properties of electrostatic and magnetic fields, and are referred to as active focusing elements when electromagnetic fields are applied to achieve these focusing effects. The diode extraction system discussed earlier describes the simplest case of an ion beam active focusing system; the ion beam is shaped and feels focusing effects due to a lens effect of the extraction aperture. The extent to which the beam is focused depends on the relative strengths of the plasma density and the applied electric field. Additional focusing elements provide greater control of the beam focusing achievable in the extraction system. Accel-decel systems or systems utilizing Einzel lenses introduce additional electrodes to which electrostatic potentials can be applied, allowing for greater flexibility in focusing the beam diameter to the desired value. Magnetic lenses such as solenoids or quadrupole magnets are also readily employed for beam focusing, requiring strong magnetic fields for intense beam currents. Figure 3.8 shows the focusing effects of two solenoid fields on a hydrogen ion beam.

While the use of active focusing elements to simultaneously achieve beam transport and beam focusing is widely studied and employed for various ion beam applications, situations arise in which additional active focusing elements are undesirable. Any portable system greatly benefits from the reduction in bulk and complexity that is possible by eliminating additional focusing elements and the associated power supplies. The beam optics then rely on the design of the acceleration column and the characteristics of the ion beam. While the ion beam tends to feel focusing effects even in the simple diode extraction case, the extent of focusing achievable is limited and the minimum ion beam diameter is of the order of the diameter of the extraction aperture. Thus in the absence of active focusing methods, small extraction apertures are employed for applications requiring small diameter ion beams. Because the ion current density from an ion source is fixed by the operating conditions, the total ion current extracted from the ion source becomes

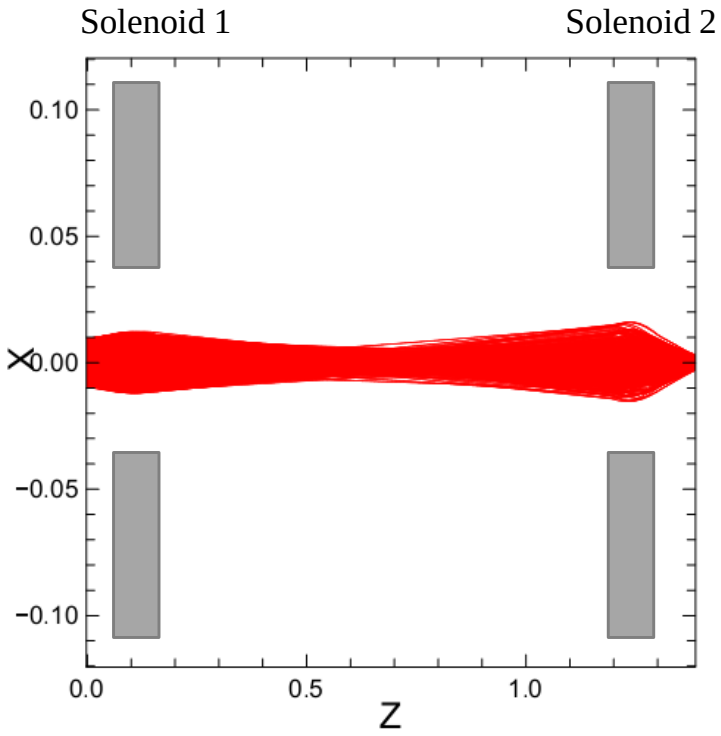

Figure 3.8: Simulation of focusing effects of two solenoid fields on a hydrogen ion beam.

practically limited by the area of the extraction aperture. A factor of two reduction in the diameter of the extraction aperture results in a reduction of the extracted ion current by a factor of four. Applications requiring high beam current densities over small beam areas thus require high plasma densities from the ion source to compensate for the restrictions imposed by the size of the aperture.

For the associated particle imaging application discussed in Section 1.2.1, neutron yields comparable to and greater than that available from existing systems prescribe a monatomic ion current on the neutron production target of the order of 50 μA for the D-T fusion reaction at 100 keV beam energy. The imaging resolution desired of the system also imposes a 1 mm diameter on the ion beam at the target. For Penning-type discharges, the diatomic nature of the majority of extracted beam ions further increases the current requirement by as much as a factor of 5. For the BLP source described in the previous section, the maximum measured current density of 2.2 mA/cm^2 requires an extraction aperture on the order of 3.5 mm in diameter to achieve the desired neutron yield. Because no active focusing elements are to be utilized in this API application, the BLP source cannot meet the design goal of a 1 mm beam diameter at the neutron production target if the high neutron yield requirement is satisfied. The low plasma density of the BLP source, coupled with the characteristic diatomic nature of ions in hydrogen and hydrogen isotope plasmas in Penning-type discharges, creates technical challenges for the incorporation of the BLP source into a high-yield neutron generator with small beam spot on target.

Because the use of additional electromagnetic fields for beam focusing is undesirable for the previously described API application, methods of passive beam focusing were explored. Passive beam focusing aims to reduce the diameter of the ion beam by utilizing elements in the extraction system that do not require additional applied electromagnetic fields, making use of the applied voltages already present in the acceleration column of the system.

3.4.1 Ion beam collimation

Collimation traditionally refers again to optics principles and involves passing rays of light through long, narrow, parallel channels in a material. Rays that are not parallel to the axis of the collimating material, or the collimator, are absorbed by the material, while parallel rays pass through the channels unimpeded. Practically, a maximum angle of divergence is defined by the geometry of the collimating channels; rays with divergence angles below the cutoff angle will pass through the collimator, reducing the divergence and resulting in more parallel rays. Figure 3.9 illustrates the passage of rays of light through a collimator.

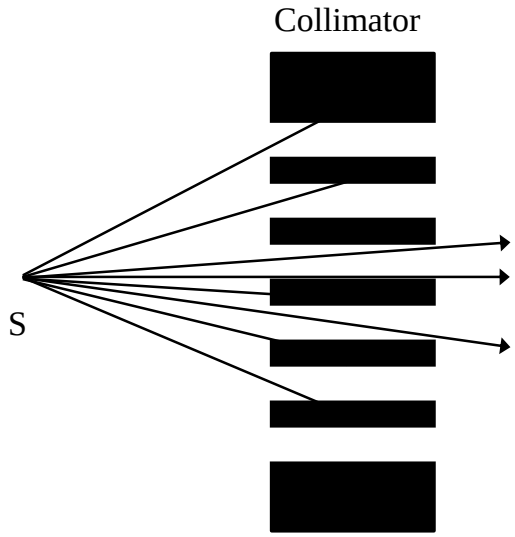

Figure 3.9: Light passing through a collimator. Light rays from the point source S pass through the collimator for small divergence angles. Large divergence angles result in absorption at the collimator.

Similarly, ion beams passing through long, narrow channels are collimated, removing ions with large divergence angles from the beam. The situation with ion beams becomes more complicated, however, due to the nature of the charged particle beams and interactions with electromagnetic fields. Ideally, charged particles in field-free regions would behave similarly to

light rays, and passage through a collimator would result in a relatively parallel beam with minimal divergence. In practice, however, self-induced fields within the ion beam and space-charge effects will both act to increase the divergence of the beam even after collimation. The situation is exacerbated when electromagnetic fields are present; accelerating fields, especially nonlinear fields, can reduce the effectiveness of collimation by causing additional emittance growth. Nevertheless, collimation is useful for limiting the growth of the beam diameter by reducing the spread of divergence angles within the beam. An important consequence of the use of ion beam collimation is the resultant reduction in the beam current after passage through a collimator. The collimator physically blocks ions from exiting the collimating material, and current losses to the collimator can be substantial depending on the geometry of the collimator and the characteristics of the beam. Certain applications take advantage of this beam loss; neutron generator development done in [51] relied on ion beam collimation to limit the beam current and resultant neutron yield such that a maximum neutron yield was not exceeded. The Gaussian nature of the extracted ion beam typically results in a beam "core" and "halo" structure, where the majority of the beam ions have low divergence angles and are centered around the beam axis, or the core. A fraction of the beam ions have larger divergence angles and larger radial positions within the beam; these ions make up the low intensity beam halo, and collimation of this portion of the beam results in a reduced beam diameter while minimizing current losses to the collimator.

This collimation effect is difficult to simulate using traditional ion optics codes due to the methods by which the plasma or ion beam is initiated within the simulation. For IGUN, the adjustment of the Debye length over each iteration cycle results in poor simulation convergence for large aspect ratios on the extraction aperture, i.e. when the diameter of the extraction aperture is not large compared to the length of the extraction channel. For PBGUNS, the simulated plasma region is defined by a surface of emission on the plasma electrode, and the effect of the extraction channel length on the transmitted beam radius and current is only observed when an angular distribution is imparted to the initiated beam. PBGUNS provides several methods by which this can be done, including specifying angular distributions along the

axial direction within the plasma region and initiating a Maxwellian angular distribution over the emission surface. These methods increase the number of simulation cycles required for program convergence, but more closely approximate the collimation effect of a long extraction channel than the parallel beam injection mode. Figure 3.10 shows the geometric representation of the plasma electrode for several extraction channel lengths simulated using PBGUNS. The extraction of an atomic deuterium (D^+) ion beam with beam energy of 100 keV was simulated using different extraction channel lengths. The effect of the extraction channel length on the ion current on target, ion beam diameter, and maximum divergence angle was analyzed at the surface of a target situated 55 mm downstream from the plasma electrode, similar to the ion optics simulations discussed in section 3.3; the ion current density across the extraction aperture area was held constant for all channel lengths. Simulation results for the beam current and radius on target are plotted in Figure 3.11. As the channel length increases, the beam current reaching the target decreases as more current is lost to the channel. The beam diameter also decreases with increasing channel length.

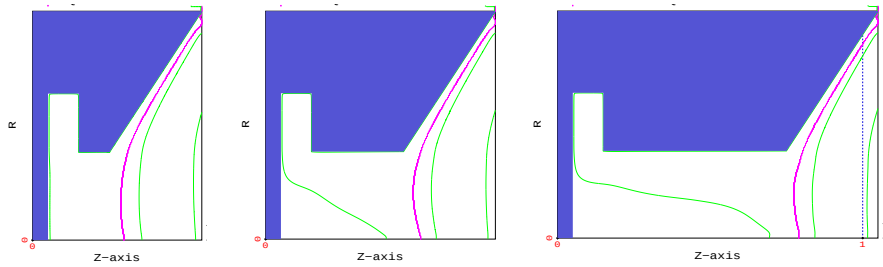

Figure 3.10: Channel length variation in PBGUNS simulations. Extraction channel lengths of 0.1 mm (A), 0.3 mm (B), and 0.6 mm (C) are shown.

Collimation experiments were performed to analyze the effects of collimation channel length on the resultant ion current and ion beam diameter. Experiments utilized a Penning source obtained from Thermo Fisher Scientific. The Thermo Penning source was fitted with a 2 mm diameter extraction aperture. The extraction aperture has an intrinsic channel length of 5 mm.

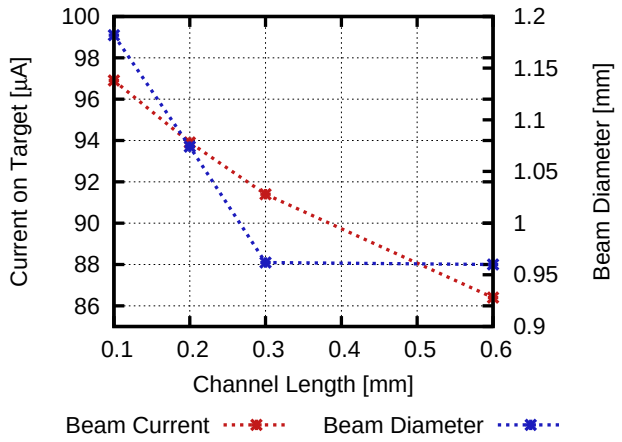

Figure 3.11: PBGUNS simulation results for increased channel length. Both the beam current and beam diameter on target decrease with increasing channel length.

The presence of an intrinsic channel length subjects the ion beam to collimation effects as it is extracted from the ion source, and additional collimator pieces were incorporated into the extraction aperture to measure the effects on the ion beam spot size and ion current on target at various ion energies. Two additional collimator pieces extend the extraction channel length to 8 mm and 11 mm; Figure 3.12 illustrates the collimator setup with respect to the ion source. It is noted here that increasing the length of the channel through which ions are extracted has two major effects: in addition to collimating those ions in the beam with large divergence angles, the long extraction channel also affects the plasma meniscus formation. The long extraction channel alters the equipotential lines at the exit of the channel, and thus affects the plasma boundary with the vacuum region. The beam diameter and ion current on target for the various extraction channel lengths thus results from the combined effects due to the altered plasma meniscus and altered ion optics and the beam collimation itself.

The Thermo Penning source was operated in several modes during the ion beam collimation experiments. Because the plasma density in Penning-type discharges increases with increased gas pressure, the Thermo Penning source was typically operated with either 0.6 or 3.0 mTorr of hydrogen gas and the

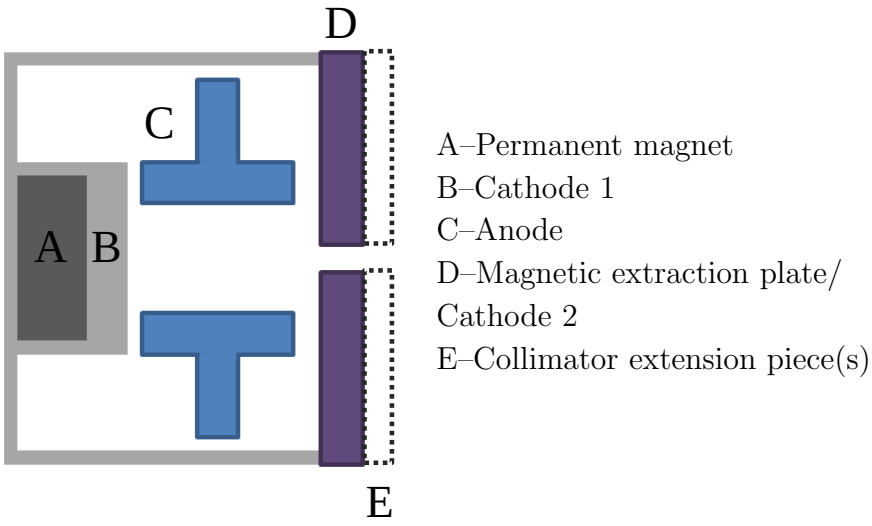

Figure 3.12: Collimator setup with respect to Thermo Penning ion source. The magnetic extraction plate has an intrinsic channel length of 5 mm. Additional extension pieces increase the channel length to 8 mm and 11 mm.

effects on the extracted ion current (and, indirectly, the matching between the plasma meniscus and the extraction electric field) were measured. The gas pressure within the source also affects the distribution of ion energies within the plasma and extracted ion beam [27], which can also affect the properties of the extracted ion beam and subsequent collimation effects. The Thermo Penning source houses permanent magnets to generate the axial field required for the Penning discharge, and so the axial magnetic field was not adjusted during operation. The anode voltage was fixed at 2.4 kV for these experiments, resulting in discharge currents of 1.2 and 1.8 mA at source operating pressures of 0.6 and 3.0 mTorr, respectively.

For beam energies below 50 keV, the ion beam diameter on target was measured optically by recording images of the beam spot on a target through a transparent vacuum window. The target surface was angled 45 degrees with respect to the beam axis to enable viewing of the beam spot, resulting in elliptical beam images. The extraction system consists of three distinct electrodes: the plasma electrode at the source, the electron suppression shroud, and the target. A schematic of the experimental setup can be seen in Figure 3.13. The source body and plasma electrode are held at ground potential, while the (negative) accelerating potential is applied to the electron suppression shroud. Reverse-biased Zener diodes provide a constant 1.4 kV voltage difference between the electron suppression shroud and the target, such that a separate potential is not applied to the target. A 200 MΩ bypass resistor forces current through the circuit; this current ensures that the Zener diodes maintain the required breakdown voltages, and the proper potentials are applied to the target and electron suppression shroud. The target potential is more positive than the potential on the electron suppression shroud. The electron suppression shroud suppresses secondary electrons that are emitted from the target upon ion impact; secondary electrons emitted from the target are repelled by the more negative potential at the shroud, and thus cannot be accelerated back toward the plasma electrode. The absence of the electron suppression shroud would allow backstreaming electrons to contribute to the overall current measurement at the target and thus should be avoided. The beam spots and beam intensity profiles were analyzed using the image analysis program ImageJ [52]. The beam spot size was quantified by analyzing

the major and minor axis data for the elliptical beam patterns.

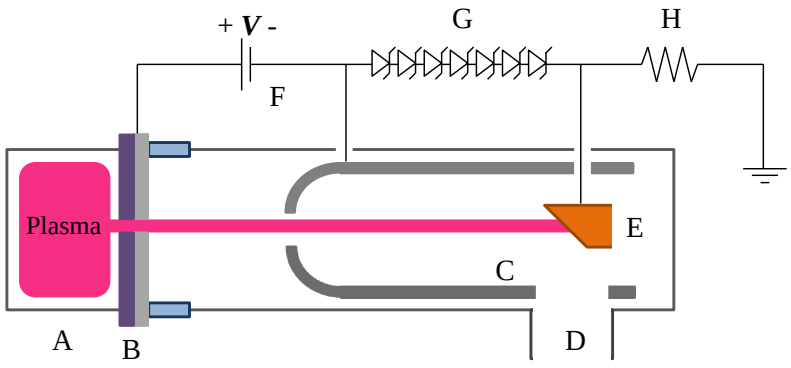

A–Ion source
B–Collimator
C–Electron suppression shroud
D–Side port to camera
E–Angled target
F–High voltage supply
G–Diode stack
H–Bypass resistor

Figure 3.13: Schematic of experimental setup for optical observation of beam spot on target. A negative high voltage is applied between the plasma electrode and the electron suppression shroud. The diode stack provides a 1.4 kV voltage difference between the shroud and target; the target is biased at a more positive potential than the shroud. The bypass resistor to ground ensures constant current flow through diode stack.

Experimental results

Figure 3.14 shows elliptical beam spot images for extraction voltages of 0, -10, and -20 kV. The nature of the Penning discharge results in a nonzero ion current even without an applied extraction voltage; ions are accelerated to the two cathodes by the symmetric potential distribution within the discharge chamber, and some ions near the central axis of the source are able to stream out of the discharge region through the extraction aperture. As the extraction voltage is increased, the intensity of the central region, the beam core, increases.

Figure 3.15 shows beam spot images for the two modes of operation at

Figure 3.14: Elliptical beam spot images for extraction voltages of 0 (A), -10 (B), and -20 (C) kV. The intensity of the central region, the beam core, increases with increasing extraction voltage.

beam energy of 30 keV and extraction channel length of 5 mm. The elliptical beam spot images corresponding to operation in the high pressure (3.0 mTorr) mode are characterized by an intense central region, the beam core, and less intense perimeter region, the beam halo. Beam spot images from operating in the low pressure (0.6 mTorr) mode exhibit less intense beam cores, with less distinct transitions between the core and halo regions. The two different operation modes were investigated to examine the effects of the plasma density on the beam spot on target. While a decrease in beam core intensity was observed for low pressure operation, no appreciable difference in beam diameter was observed for all extraction channel lengths. Major and minor axis data as a function of extraction channel length are plotted for 30 keV hydrogen beams in Figure 3.16. These data were obtained by analyzing the intensity profiles of the elliptical beam images. The major and minor axis data typically vary by about ten percent between the two operation modes for each channel length. For the longest extraction channel length, 11 mm, very little difference in beam diameter was observed between the two modes. It is noted here that only qualitative ion current measurements at the target were obtained during these experiments due to the nature of the experimental setup, and that more accurate measurements were obtained in subsequent experiments (see following section). Qualitatively, the ion current on target for a given extraction channel length is higher for source operation with higher gas pressure. The higher plasma density results in more ions that can be extracted. For similar operating regimes, increasing the extrac-

tion channel length resulted in reduced ion current on target for a given beam energy. The increased extraction channel length imposes a stricter angular cutoff condition on the ions in the beam.

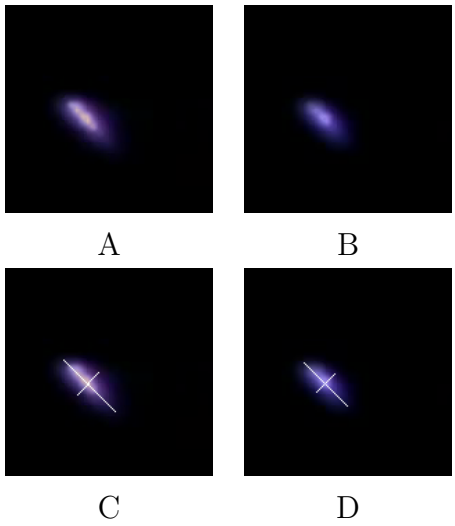

Figure 3.15: Elliptical beam spot images for Thermo Penning source high (A, 3.0 mTorr) and low (B, 0.6 mTorr) pressure operation. The beam energy is 30 keV, and the extraction aperture is 2 mm in diameter. The central region of the beam is more intense for high pressure operation. In (C) and (D), the same images are overlaid with major and minor axes to demonstrate the analysis method.

Subsequent experiments ran the Thermo Penning source in the high pressure mode to maximize the ion current on target. The elliptical beam images on target were observed for beam energies of 10-40 keV, with representative beam images shown in Figure 3.17. As the extraction voltage and beam energy are increased for a given channel length, the intensity of the beam core increases, while the overall beam diameter decreases. This trend can be seen for all extraction channel lengths. As the extraction channel length increases for a given beam energy, the overall beam diameter also decreases, as do the total areas and intensities of the beam core and halo regions. At a given beam energy, better matching between the plasma meniscus and the applied

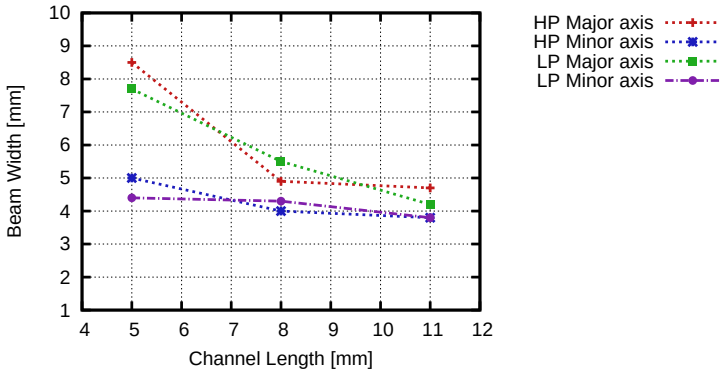

Figure 3.16: Major and minor axis data as a function of extraction channel length. The beam energy is 30 keV. HP denotes high pressure operation, and LP denotes low pressure operation.

electric field typically occurs for extraction channel lengths on the order of the diameter of the extraction aperture. The Thermo Penning source features an extraction channel length that is over a factor of two larger than the diameter of the aperture, and it is expected that the ion optics are optimized for extraction with the original aperture. As the extraction channel length increases, the magnitude of the electric field within the channel decreases, and the extracted ion current on target likely reflects the combined effects of both the variation in the plasma-vacuum region boundary and the collimation of ions in the beam.

The intensity profiles along the major and minor axes of the elliptical beam images are plotted in Figure 3.18 for channel length of 5 mm at beam energy of 40 keV. Similar analysis was performed for the extended channel lengths. The intensity scale has arbitrary units, but it is noted that the same scale is used for all beam profiles. Beam profile analysis data are plotted in Figure 3.19. Increasing the channel length from 5 mm to 8 mm results in a reduction in both the major and minor axis beam diameters, with no reduction in intensity of the beam core region (not shown). Further increasing the extraction channel length to 11 mm further reduces the major and minor axis beam diameters, but also results in a 25% reduction in the beam intensity.

For beam energies above 50 keV, the experimental setup was modified

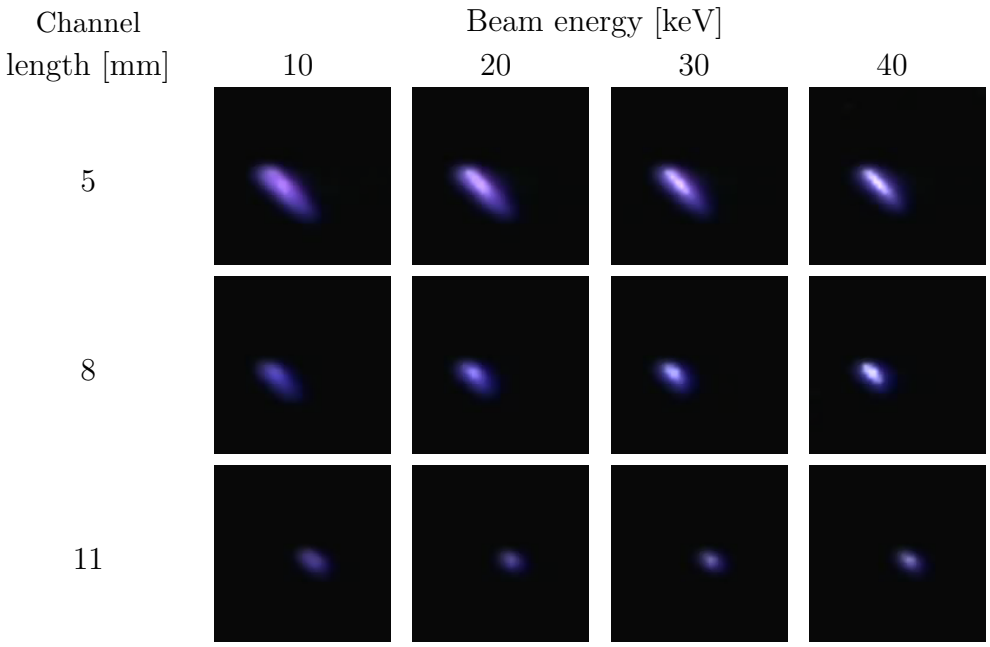

Figure 3.17: Elliptical beam spot images for increasing channel length. The overall beam diameter decreases with increasing extraction voltage.

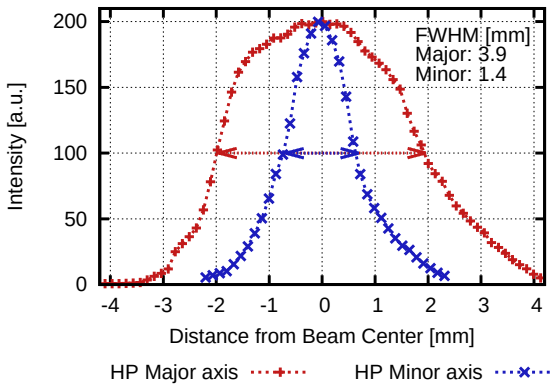

Figure 3.18: Beam intensity profiles along the major and minor axes of elliptical beam image for 5 mm channel length. The beam energy is 40 keV.

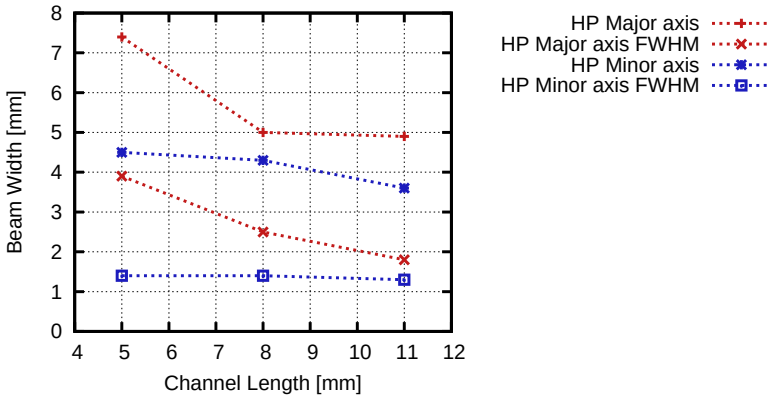

Figure 3.19: Major and minor axis data as a function of extraction channel length from beam profile analysis. The beam energy is 40 keV.

such that viewing of the beam spot on target was no longer possible. The ion source and vacuum chamber were mounted within a shielding enclosure for maximum beam energy of 81 keV. The extraction gap length between the plasma electrode and electron suppression shroud was adjusted to match this maximum beam energy. Measurement of the beam diameter on target was accomplished by measuring the burn marks left on flat targets after ion extraction for extended periods of time. The ion current on target was measured across a 4.88 kΩ resistor between the target and the bypass resistor to ground. For "high pressure" source operation with 3.0 mTorr gas pressure in the ion source and 2.4 kV applied anode voltage, the extracted ion current was measured at the target as a function of extraction voltage applied to the electron suppression shroud for ion extraction with the three extraction channel lengths. The extraction voltage was ramped up to -81 kV and then held constant at -81 kV so that the burn mark pattern at the target was allowed to develop. The duration over which the beam energy was kept at this maximum value varied based on the measured target at the current. Figure 3.20 shows the extracted ion current measured on target as a function of the beam energy for ion extraction through a 2 mm diameter aperture for the three extraction channel lengths. Similar data is also plotted in Figure 3.20 for ion extraction through a 1 mm aperture. The longer extraction channels result

in substantial current attenuation; for extraction through the 2 mm diameter aperture, the ion current on target decreases by about 30% for each 3 mm increase in the extraction channel length. This behavior is not reflected in the data from ion extraction through the 1 mm diameter aperture, likely due to the placement of the 1 mm aperture. The limiting aperture was placed between the original extraction plate and subsequent extraction channel extension pieces, such that the aperture at the channel exit was 1 mm only for the case with no additional extension pieces, i.e. 5 mm channel length.

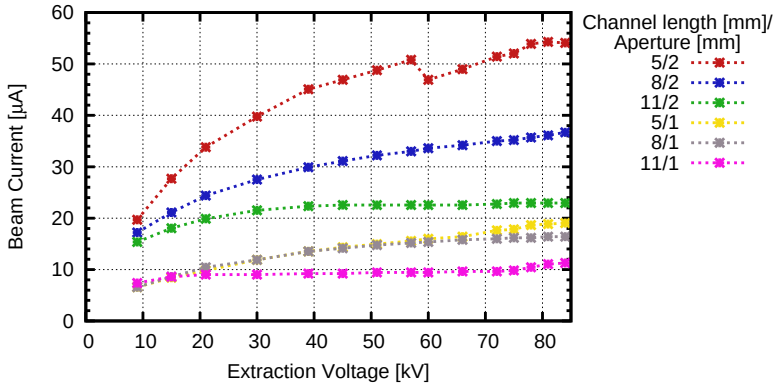

Figure 3.20: Ion current on target for 1 and 2 mm diameter extraction apertures and extraction channel lengths of 5, 8, 11 mm.

For a constant plasma density and current density at a given ion source extraction aperture, the extracted ion current scales with the area of the extraction aperture. A reduction in the diameter of the extraction aperture by a factor of two should result in a decrease in the extracted ion current by a factor of four. The extracted ion current data in Figure 3.20 indicate that the ion current from the 1 mm aperture is greater than 25% of that from the 2 mm aperture for all extraction channel lengths. This is likely due to beam loss on the collimator, as well as the placement of the 1 mm diameter limiting aperture. The 30% decrease in ion current on target with each 3 mm increase in extraction channel length is not observed with the use of the 1 mm aperture; the 1 mm diameter aperture combined with 2 mm diameter extraction channels results in an increased cutoff angle for ions in the beam as compared to 1 mm diameter extraction channels. The 30% decrease in ion

current with increased extraction channel length may be observed for true 1 mm diameter extraction channels.

The ion beam diameter at the target was measured by examining burn mark patterns on aluminum foils at the target surface after exposure to the incident ion beams at beam energy of 81 keV. Burn mark patterns for 2 mm extraction apertures can be seen in Figure 3.21 for the three extraction channel lengths. The burn mark patterns are typically characterized by a small diameter, darker beam core region and a larger diameter, less intense region concentric with the core. The total burn pattern diameter for each case is slightly larger than the 2 mm diameter of the extraction aperture. It is noted here that the less intense burn pattern may be due to the less intense beam halo discussed earlier, but may also be due to heat deposition by the energetic ions. The burn mark for extraction with the 11 mm long channel is noticeably different than for the shorter channels; the darker beam core is not present in the burn pattern for the longest channel. The burn pattern also shows a different color variation for the longest channel, and may be due to the less intense, lower current beam obtained with the longest channel. The burn pattern for the longest channel may resemble the patterns for the shorter channels given adequate exposure time. Intensity analysis of the burn mark images was performed, with results shown in Figure 3.22. Intensity profiles were taken along lines bisecting the burn mark patterns. For extraction with 5 and 8 mm long channels, the low intensity (darker) regions in the beam profile plot indicate the beam width. The spike in intensity in the beam profile plot for the 5 mm channel is due to damage on the foil surface. For extraction with the 11 mm long channel, the color variation in the burn pattern results in a beam profile plot where the beam width is indicated by the high intensity (lighter) central region of the profile. While the beam profile plots indicate beam widths of 2 mm for each of the three extraction channels, it is difficult to determine the true beam width from burn pattern analysis due to the nature of the burn marks: larger diameter features may or may not be due to heat deposition.

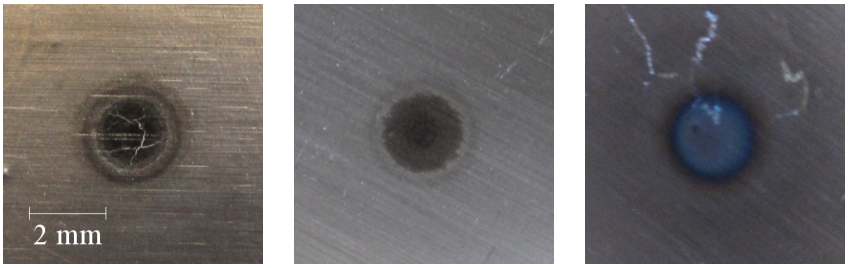

Figure 3.21: Burn mark patterns on target for extraction channel lengths of 5 (A), 8 (B), and 11 (C) mm. Burn mark patterns are typically characterized by a small diameter, darker beam core region and a larger diameter, less intense region concentric with the core. The burn mark for extraction with the 11 mm long channel is noticeably different than for the shorter channels.

Collimation summary

Ion beam collimation by utilizing long extraction channels reduces the divergence of beam ions and the overall beam diameter as measured at a beam target downstream from the extraction aperture. This has been confirmed both optically and by measuring burn patterns left on the target after prolonged exposure to the ion beam. Collimation using long extraction channels also results in current attenuation; this effect is more pronounced with increased extraction channel length. For higher beam energies, the use of collimating channels at the extraction aperture typically results in ion beam diameters at the target that are of the order of the extraction aperture, indicating that beam divergence due to the strong accelerating field is minimal.

3.4.2 Ion beam guiding

For ion sources with low plasma and beam current densities such as the BLP source, reducing the beam diameter by utilizing both small extraction apertures and long extraction channels results in current attenuation that restricts the usefulness of such a source. The high neutron yields desired for the transmission imaging methods discussed in Section 1.2.1 are not attainable

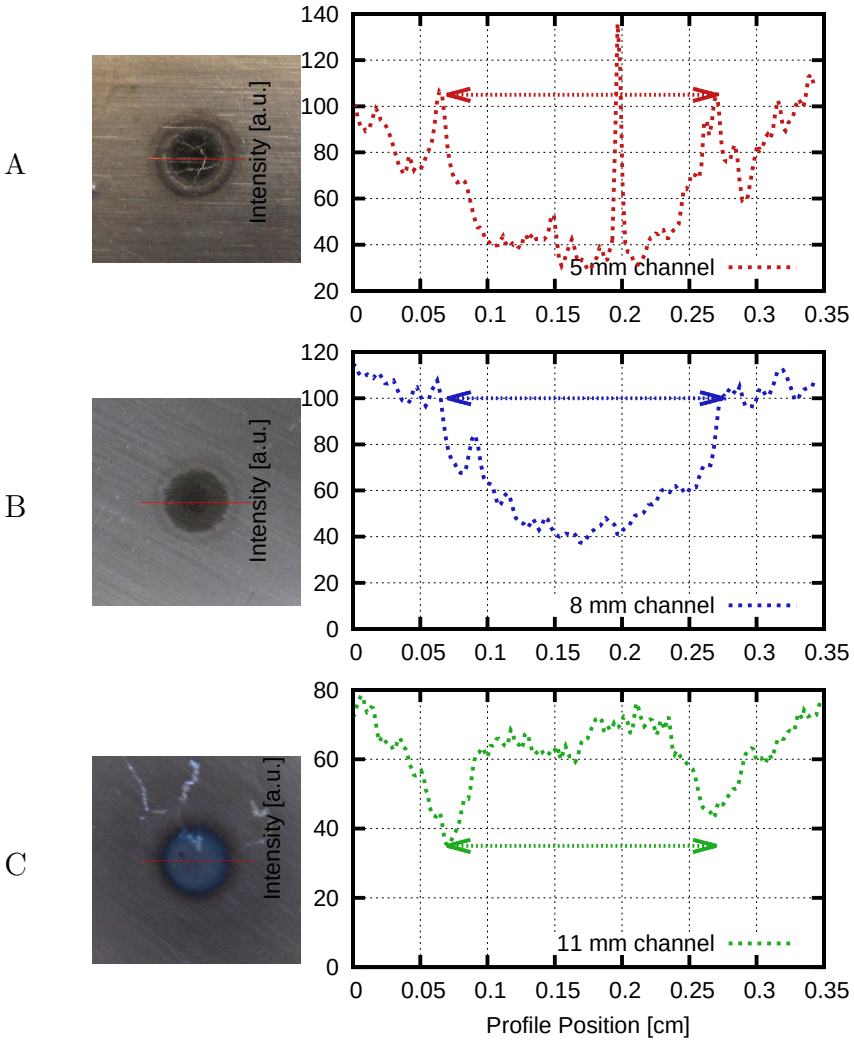

Figure 3.22: Burn mark profile analysis for extraction channel lengths of 5 (A), 8 (B), and 11 (C) mm. The red lines through the burn mark centers indicate the position along which the intensity profile is plotted for the respective patterns. Each pattern indicates a beam width of 2 mm, as indicated by the arrows on the plots above.

with the BLP source if extraction apertures of 1 or even 2 mm in diameter are used; the low current output of such a source forces a tradeoff between high neutron yield and the spatial resolution achievable with beam diameters on the order of 1 mm. The ability of a system to focus a low current, larger diameter beam such that the current density of the beam is increased greatly enhances the usefulness of such a system. As discussed previously, methods for beam focusing utilizing applied electromagnetic fields are widely available but highly undesirable for the field-portable applications of interest. A method of passive beam focusing known as ion beam guiding has seen recent and extensive research, most notably for beams of highly charged ions. This method is of interest for applications such as patterning of surfaces with microbeams and irradiation of cells [53], as well as particle induced X-ray emission (PIXE) analysis [54], and typically make use of μm beam widths. Early work explored the use of microscopic channels in dielectric foils, with nm scale capillary diameters and μm scale capillary lengths, but the use of macroscopic capillaries for imaging applications has attracted recent interest. The passive focusing is achieved with the use of a tapered dielectric capillary. The dominant process is often attributed to the charging of the inner wall of the capillary by incident ions as the ion beam is injected into the tapered dielectric capillary [55]. Ions incident on the inner wall of the capillary create local charge patches that deflect subsequent incident ions away from the inner wall. Ion guiding is achieved after the inner surface charges up, and subsequent incident ions are guided toward the capillary exit. Figure 3.23 illustrates the charging behavior required to establish the ion guiding effect.

The parameters relevant to the discussion of ion guiding with the use of tapered dielectric capillaries are the transmission efficiency and the beam compression factor. The transmission efficiency ϵ is defined here as the ratio of the exit beam current to the incident beam current. The beam compression factor is defined as the ratio of the exit beam current density to the incident beam current density. Additionally, the geometric transmission efficiency ϵ_{geom} is defined as the ratio of the exit and incident cross-sectional areas of the dielectric capillary, and represents the minimum transmission efficiency of the transmitted ion beam due to collimation effects.

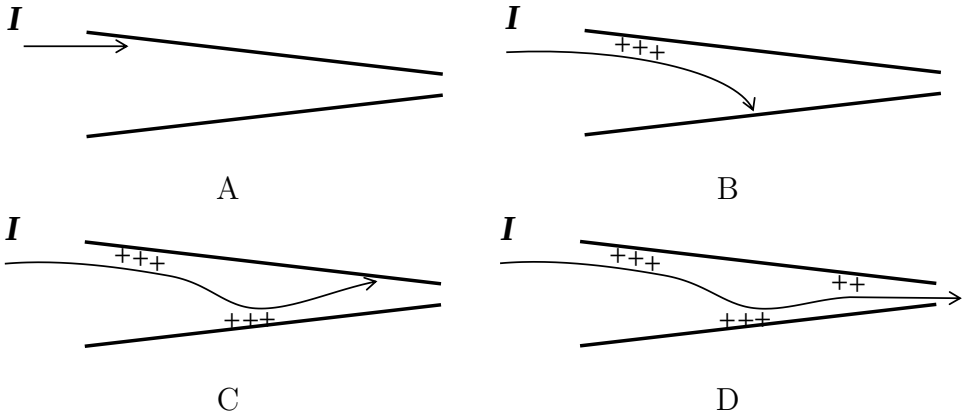

Figure 3.23: Schematic of charging behavior required to establish the ion guiding effect, as in [55]. In (A), ions incident on the inner wall of the dielectric capillary create a local charge patch that deflects subsequent ions (B), (C) away from the inner wall. In (D), the local charge patches guide the ion beam to the capillary exit.

$$\epsilon = \frac{I_{exit}}{I_{entrance}} \tag{3.4}$$

$$\epsilon_{geom} = \frac{A_{exit}}{A_{entrance}} \tag{3.5}$$

$$\eta = \frac{J_{exit}}{J_{entrance}} = \frac{\frac{I_{exit}}{A_{exit}}}{\frac{I_{entrance}}{A_{entrance}}} = \frac{\epsilon}{\epsilon_{geom}} \tag{3.6}$$

where

$I_{entrance}$, I_{exit}: Ion currents at capillary entrance and exit
$A_{entrance}$, A_{exit}: Cross-sectional areas at capillary entrance and exit

Much of the work on ion guiding focuses on either the guiding of slow (tens of keV), highly charged ions, or fast (MeV), light ions. These two

regimes have been observed to exhibit different ion transport characteristics that affect the overall transmission efficiency of the dielectric capillary; aspects of the transmission and beam compression of fast, light ions has thus led some to conclude that the dominant transport mechanism is not the charging of the inner wall of the dielectric capillary, but the small angle scattering of ions off the insulating walls as they traverse the length of the capillary. The wide range of variable parameters for a given guiding experiment makes comparison across and even within regimes difficult, but examining the different dependencies allows for better understanding of the processes involved and evaluation of the viability of this passive focusing method for the API application.

Tilt angle dependence

The angle between the beam and capillary axes has been observed to affect the transmission of ions through tapered dielectric capillaries. Several groups [56], [57], [58], [59] have reported maximum transport efficiencies for nonzero tilt angles between the beam and capillary axes, while others [60], [61] observe no such effect, instead observing maximum transmission when the beam and capillary are aligned. Figure 3.24 shows reported transmission efficiency as a function of tilt angle for 2 MeV protons [61] and 24 keV Ar^{8+} ions [56].

It is interesting to note that the conflicting tilt angle dependence spans both regimes. In the work performed by Kreller et al. [56], the transmission of Ar^{8+} ions was observed for beam energies of 8, 24, and 60 keV; the authors report maximum transmission efficiency at nonzero tilt angles for the lower energy ion beams, but no such effect for the 60 keV beam. This trend would seem to indicate that the tilt angle dependence vanishes with increasing beam energy, but this is refuted by the previously cited work by Nebiki et al. with both 2 MeV He^{+} ions [57] and 6.4 MeV $^{15}N^{2+}$ ions [58]. Incorporation of a dielectric capillary into any final application would thus require experimental determination of the tilt angle dependence of the given system.

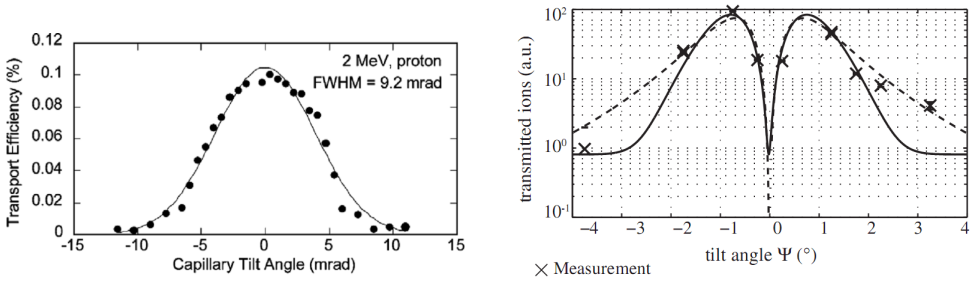

A B

Figure 3.24: Reported transmission efficiency dependence on tilt angle between ion beam and dielectric capillary axis for a 2 MeV beam of protons [61] (A) and 24 keV beam of Ar^{8+} ions [56] (B). In (A), the maximum transmission occurs when the ion beam and dielectric capillary are aligned. In (B), a non-zero tilt angle between the ion beam and dielectric capillary axis results in maximum transmission.

Energy dependence

Because individual guiding experiments typically utilize monoenergetic beams or focus on a narrow range of energies for a given ion species, the effect of the ion energy on the transmission characteristics has not been definitively determined. As previously noted, Kreller investigated the transmission of Ar^{8+} ions for several beam energies, but the authors do not discuss the transmission efficiency dependence on the incident ion energy. Vokhmyanina et. al [62] studied the transmission of 200-500 keV protons through a macroscopic tapered quartz tube, with results suggesting a $\frac{1}{E}$ dependence for the transmission efficiency in this energy range. Extrapolating this dependence to include MeV protons predicts a higher transmission efficiency than that reported by Hasegawa et al. [61], though it is noted that neither group reports much information on the ion currents used for both experimental setups. While groups working with highly charged ions in the low-keV energy range have widely accepted the dominant transport mechanism to be the guiding effect from the charged inner wall of the capillary, those working in the MeV energy range tend to attribute the transport mechanism to small

angle scattering of the ions off the inner capillary wall [63], [57], drawing these conclusions from the lack of observed time dependent behavior of the transmission efficiency (see next section). Monte Carlo simulations [63] of the elastic scattering of protons off the inner walls of a tapered glass capillary show good agreement with experimental results for the outlet beam intensity profile of 2 MeV protons, strongly suggesting that small angle scattering is the dominant transport mechanism in this energy regime. The energy range over which the transition between the two dominant mechanisms occurs remains undetermined.

Charge/current dependence

The transmission efficiency for highly charged ions through tapered dielectric capillaries typically exhibits time dependent behavior that is associated with the charge up of the capillary inner wall. The transmission efficiency has been observed to increase with the charge buildup time, stabilizing to a maximum value as a charge equilibrium is reached. Figure 3.25 shows the time dependent behavior of the transmitted ions as reported by Ikeda et al. [53] and Nakayama et al. [59]. Several groups have observed this charge buildup to occur over tens of seconds for ion currents in the pA range. The transmission of light ions with MeV energies has not demonstrated this time dependence, a strong indicator that charging of the inner wall and subsequent ion deflection is not a dominant mechanism at these higher energies. The medium energy range investigated by Vokhmyanina for the transmission of protons makes no mention of time dependent behavior.

Because the charge buildup is a function of the number of ions incident on the inner surface of the guiding structure, the ion beam current is expected to influence the transmission efficiency. Nearly all guiding experiments make use of low incident beam currents, in the pA-nA range, while the use of ion guiding for passive focusing in the API application would require the transmission of beam currents on the order of 100 μA. Increased beam current would likely result in faster charge buildup such that the transmission efficiency stabilizes more quickly. While the charge buildup for pA/nA currents occurs over tens of seconds, higher beam currents may result in such

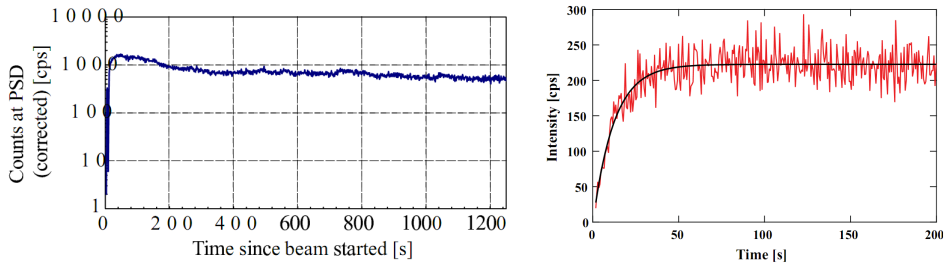

Figure 3.25: Time dependent behavior of transmitted ions for 8 keV Ar^{8+} ions [53] (A) and 3 keV I^{q+} ions [59] (B), where q=10-50. The increase in transmitted ions occurs over tens of seconds in both cases.

short charge buildup times as to mask the time dependent behavior of the ion transmission. Vokhmyanina utilized proton beam currents of up to 2 μA, and, as noted earlier, the presence or lack of time dependent behavior is unreported. Experimental and theoretical work by Gruber [64] suggests that large quantities of deposited charge on insulating capillaries has several detrimental effects on the transmission characteristics: the total transmission efficiency decreases with increasing deposited charge, and high incident ion currents can lead to sudden discharge events that instantaneously reduce the transmission efficiency. These experimental results, however, indicate that the peak transmission efficiency for a given beam energy is achieved with greater quantities of deposited charge as the beam energy increases. Thus the transmission of high ion currents may require increased beam energy for optimum transmission efficiency.

Taper angle dependence

For cases where small angle scattering plays a large role in the beam transmission, the taper angle is expected to influence both the transmission efficiency and the divergence of the beam at the exit of the dielectric capillary. Larger taper angles would typically result in more scattering events for a single ion in the beam, which can result in increased ion losses to the walls and re-

duced transmission. Larger taper angles can also increase the divergence of the beam as ions gain larger transverse energy components with subsequent scattering events. Nebiki observed reduced transmission (as measured by nuclear reaction analysis spectra) with increased taper angle for the transmission of 6.4 MeV $^{15}N^{2+}$ ions; the transmission drops by about 60% when the taper angle is increased from 7 mrad to 160 mrad. For beam transmission due to charging of the capillary inner wall, larger taper angles for constant capillary length result in reduced inner wall surface area, which can affect the amount of charge deposited and thus the transmission efficiency.

Reported beam compression factors

Beam compression is achieved when the transmitted current density through the tapered dielectric capillary exceeds the incident current density. Beam compression requires the transmission efficiency to exceed the minimum transmission due to collimation effects from the reduced aperture size, i.e. the geometric transmission efficiency. Reported beam compression factors span several orders of magnitude, with Nebiki reporting beam compression factors as high as 1.8e4 for 2 MeV He^+ ions [57]. Because many of these experiments have applications requiring beam diameters of the order of tens to hundreds of μm, the geometric transmission efficiency is often very small; the resultant transmission efficiency can be on the order of 1%. Beam compression factors of 5-10 are more widely reported [56], [53], with corresponding transmission efficiencies up to 20-30%.

Ion guiding for the associated particle imaging application

Challenges abound in adapting this passive focusing technique into a neutron generator system. While the desired beam width required for the API application is relatively relaxed compared to the μm beam widths required for the applications previously mentioned, beam currents of the order of 100 μA have not yet been studied in conjunction with ion guiding. The beam parameters relevant to a BLP source-based neutron generator prescribe a region in the ion guiding parameter space that has not yet been explored. The ion guiding method was thus investigated for the passive focusing of

predominantly molecular H_2^+ and D_2^+ ion beams with currents in the tens of μA range.

Tapered dielectric capillaries were incorporated into an experimental setup similar to that shown in Figure 3.13 to evaluate the viability of the ion guiding method for passive focusing of hydrogen and deuterium ion beams to sub-mm beam widths. The experimental setup utilized is illustrated in Figure 3.26. The BLP source was utilized to allow for adjustment of the ion current injected into the tapered dielectric capillaries. The tapered dielectric capillaries used were tapered Pyrex tubes with inner diameters at the entrance ranging from 2-3 mm, inner diameters at the exit ranging from 0.5-1 mm, and lengths ranging from 70-110 mm. A sample Pyrex tube is shown in Figure 3.27. The tapered Pyrex tube was mounted between the electron suppression shroud and the target, and an electrically isolated grid was mounted between the electron suppression shroud and the Pyrex tube entrance for measurement of the ion current injected into the guide. The ion currents on the grid and target were each measured across 57 kΩ resistors. The ion optics assembly (electron suppression shroud, grid, Pyrex guide tube) was mounted to the BLP source for alignment with the extracted ion beam axis; this experimental setup was not able to accommodate mechanisms by which the tilt angle between the guide tube and the ion beam axis could be adjusted, so no tilt angle dependencies are measured. The Pyrex tube was held in place with three-pronged plastic support pieces that ensured alignment with the axis of the ion optics assembly; rubber o-rings secured the Pyrex tube within the plastic supports. The ion optics components were supported by and electrostatically isolated from each other by ceramic rods extending from the BLP source plasma electrode surface; the assembled components are shown in Figure 3.28.

Experimental results

Incident beam currents of 10 and 20 μA were injected into the tapered Pyrex tubes with energies ranging between 20-40 keV. The incident beam currents were first measured on the grid and target with no Pyrex tube in place, to establish source operating modes for later experiments utilizing the tapered

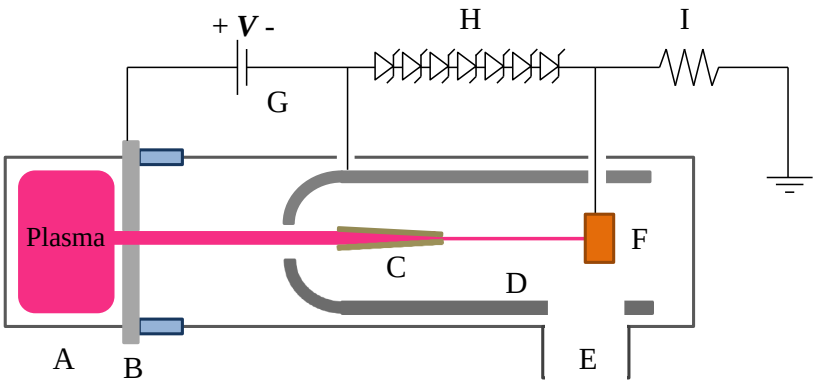

A–Ion source
B–Plasma electrode
C–Tapered dielectric capillary
D–Electron suppression shroud
E–Side port
F–Flat target
G–High voltage supply
H–Diode stack
I–Bypass resistor

Figure 3.26: Schematic of experimental setup for ion guiding experiments. Ions are extracted and accelerated by the electric field between the plasma electrode and electron suppression shroud. The tapered dielectric capillary sits between the electron suppression shroud and the target.

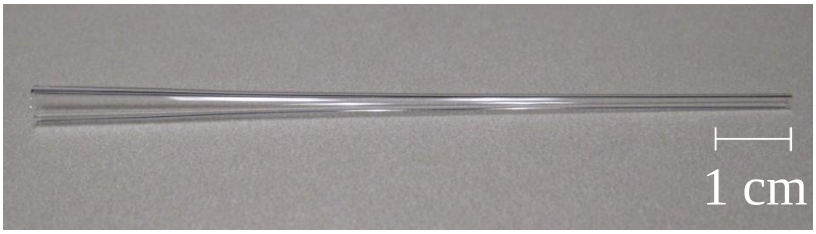

Figure 3.27: Photo of sample tapered Pyrex tube used for ion guiding experiments.

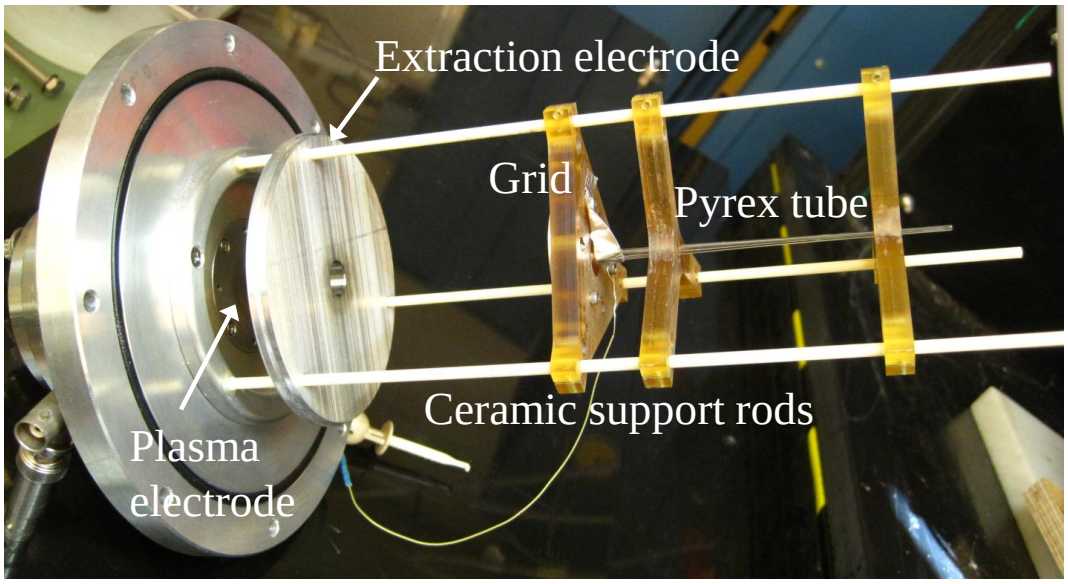

Figure 3.28: Photo of experimental setup used for ion guiding experiments. The extraction electrode, electron suppression shroud (not shown), grid, and tapered Pyrex tube are supported by plastic and ceramic supports for alignment with the ion beam axis. Components can slide along the ceramic support rods to adjust the spacing.

Pyrex tubes. The two source operating modes utilized for the ion guiding experiments largely differed in the applied axial magnetic field used to generate the discharges. Little to no ion transmission was observed when a bare Pyrex tube was utilized; it is likely that ions incident on the front surface of the capillary quickly charge up the front surface, blocking subsequent ions from being transmitted. A thin aluminum cap was placed on the front of each guide and electrically tied to the grid to prevent this charging of the front surface. Initial experiments utilized hydrogen discharges within the BLP source; deuterium discharges were later utilized for relative neutron yield measurements.

The use of tapered Pyrex tubes was observed to be very sensitive to alignment issues; though the tilt angle between the capillary and beam axes was not manually adjustable, it is noted that small errors in the alignment arose from the adjustable nature of the ion optics assembly and these slight misalignment issues often acted to severely degrade the transmission. The slight misalignment issues may be introducing a tilt angle between the capillary and beam axes that results in the suboptimal transmission conditions.

The time dependent behavior characterized by both a charge buildup over several seconds before stable transmission levels are reached and sudden discharge events that instantaneously reduce the transmission were observed during the ion guiding experiments. Figure 3.29 shows the charge buildup and subsequent stable transmission of a 20 keV, 10 μA hydrogen ion beam. The minimum (geometric) transmission efficiency for this sample was nearly 8%. The data shown in Figure 3.29 indicate a transmission efficiency of 15%; the corresponding beam compression factor is 2. It is noted here that the presence of the conductive aluminum cap at the front surface of the Pyrex tube can cause beam loss such that the actual beam current injected into the Pyrex tube is less than the nominal value expected in each operation mode; for the case plotted in Figure 3.29, the full 10 μA of current may not be injected into the guide tube due to losses on the conductive aluminum cap, and so the transmission efficiency and corresponding beam compression factor may actually be higher. The 15% transmission efficiency and beam compression factor of 2 thus represent minimum values for this experimental condition. The transmission efficiency was not observed to exhibit the $\frac{1}{\mathrm{E}}$

energy dependence suggested by Vokhmyanina in this beam energy range of 20-40 keV, instead remaining constant as the beam energy increased. The sensitivity of the alignment was readily apparent during the ion guiding experiments with hydrogen discharges; shifting from the source operating condition with output ion current of 10 μA to that with output current of 20 μA by increasing the applied axial magnetic field of the BLP source often resulted in reduced beam compression.

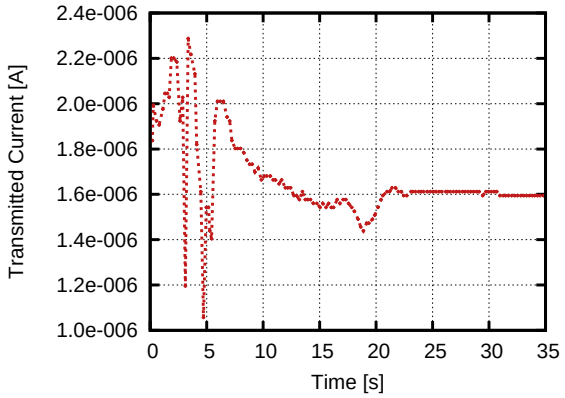

Figure 3.29: Time dependent behavior of ion transmission.

To further investigate the supposed reduced beam compression for higher injected beam current observed with hydrogen discharges, deuterium discharges were utilized to simultaneously measure the ion current on target and the resultant relative neutron yield. The BLP source was operated with deuterium gas to measure the relative neutron yields with and without the ion guiding with tapered Pyrex tubes. The flat copper target used in previous measurements was replaced with a neutron production target comprised of a titanium surface layer explosively bonded to a main copper body. Because the expected D-D neutron yield for 10-20 μA of D_2^+ ion current at 40 keV beam energy is only on the order of 1e4 n/s, the neutron detector utilized for the yield measurements was placed as close as possible to the neutron production target. The neutron detector is a BF_3 high energy neutron detector with 7 cm of borated polyethylene surrounding the detector active area. The detector was previously calibrated using an AmBe source of known source strength and distance of 1 m; the placement of the detector near the

neutron production target thus only allows for relative neutron yields to be measured. Figure 3.30 shows the neutron detector within the experimental teststand area.

Pyrex tubes with taper angles of 8 and 16 mrad were utilized during the neutron yield experiments to observe the effect of the taper angle on the transmission of deuterium ion beams. For the source operating condition with output ion current of 20 μA, the taper angle was found to have no effect on the transmission efficiency for a 40 keV, 20 μA D_2^+ ion beam; in both cases, the transmission efficiency was as high as 60%, with average values near 50% and fluctuations resulting from fluctuations in the discharge current and current losses to the grid and aluminum cap assembly. The high transmission efficiency was confirmed by both the ion current measurements at the neutron production target and by the relative neutron yield measurements, though issues with high secondary electron currents prompted further neutron yield measurements (see Chapter 4). The time dependent behavior of the transmitted ion current on target and corresponding time-averaged neutron yield for beam transmission through the Pyrex tube with 16 mrad taper angle is shown in Figure 3.31. The sharp drops in the transmitted ion current shown in Figure 3.31 typically correspond to source instabilities, though several discharge events were observed to occur over this measurement interval. These discharge events were often followed by persistent negative current as measured at the neutron production target, with slow recovery to positive values. The data plotted in Figure 3.31 indicate that though the transmitted ion current appears to decrease over time, the relative neutron yield actually increases during this measurement interval; this is likely due to effects of beam-loading of the target and is further explored in Chapter 4. The measurement of negative current at the target suggests that a significant electron current is not properly suppressed.

The neutron yield spectra for beam transmission with and without Pyrex guide tubes is shown in Figure 3.32. The 50% transmission efficiency corresponds to beam compression factors of 6 and 8 for the Pyrex tubes with taper angles of 8 and 16 mrad, respectively.

The transmission efficiency dependence on the Pyrex tube taper angle differed markedly for incident ion currents of 10 and 20 μA. Previous mea-

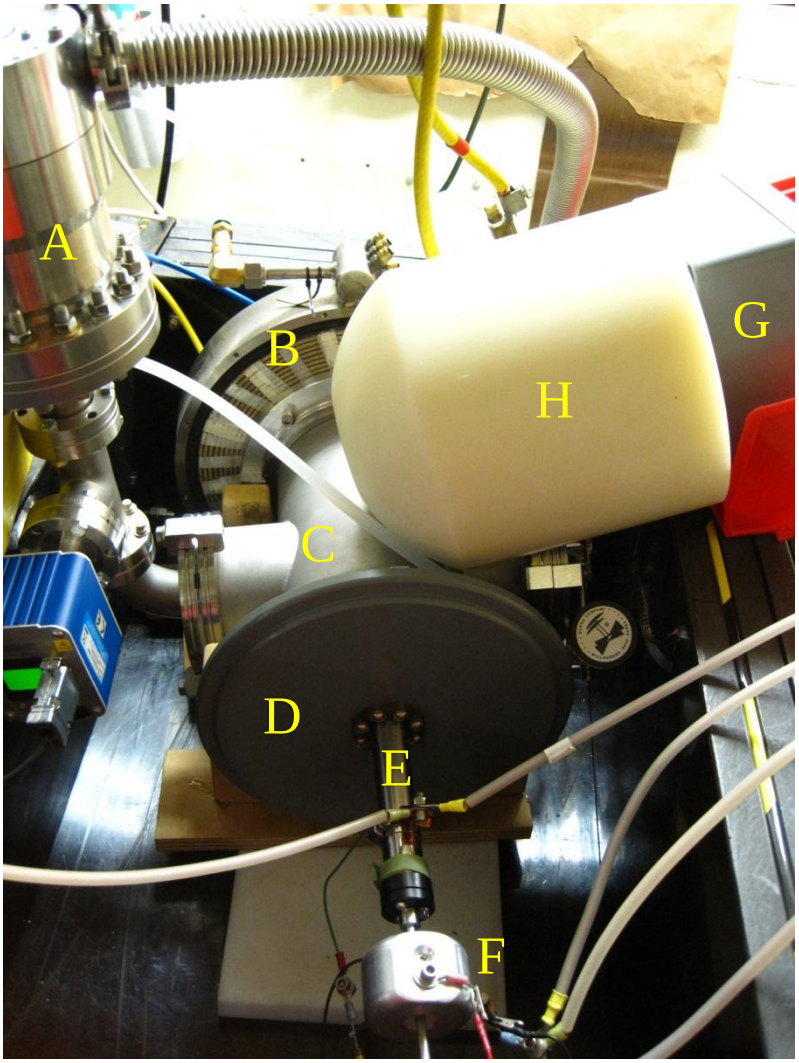

A–Turbo pump	E–HV connection for shroud
B–Electromagnet	F–HV connection for target
C–Vacuum chamber	G–Neutron detector
D–HV insulator	H–Polyethylene moderator

Figure 3.30: Photo of experimental setup within teststand with neutron detector in place. The ion source is not shown.

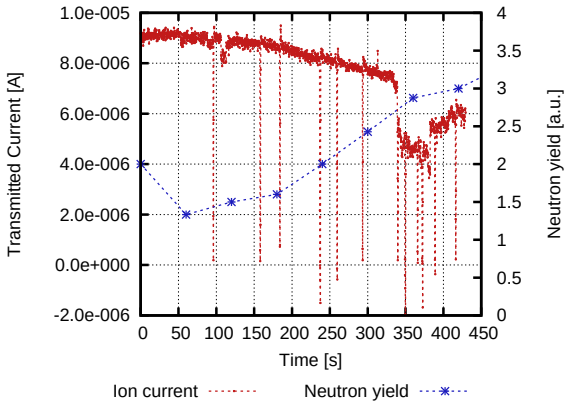

Figure 3.31: Time dependent behavior of ion transmission with corresponding time-averaged neutron yield. The 40 keV, 20 μA D_2^+ ion beam is transmitted through a tapered Pyrex tube with taper angle of 16 mrad. The decreasing transmitted ion current may be due to inadequate suppression of electrons, as the increasing neutron yield is consistent with a transmission efficiency of 50%.

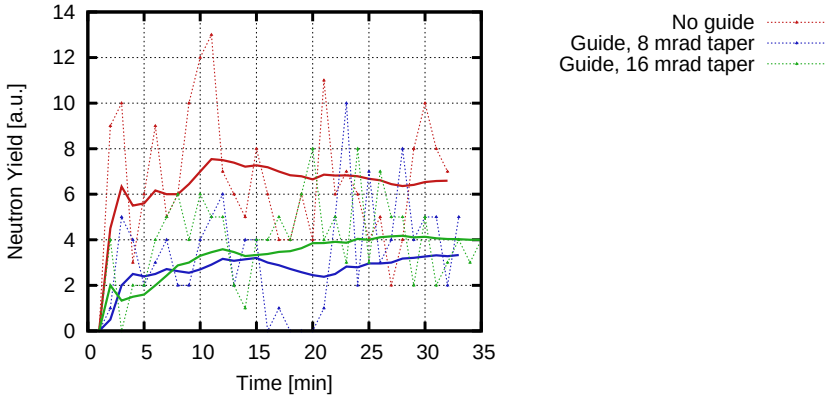

Figure 3.32: Neutron yield measurements with and without tapered Pyrex tubes for ion guiding. The neutron yields for ion guiding using Pyrex tubes with taper angles of 8 and 16 mrad both indicate 50% transmission efficiency. The solid lines indicate the relative time-averaged neutron yields.

surements with hydrogen discharges utilized the 8 mrad Pyrex tube sample, resulting in transmission efficiency of 15% and beam compression factor of 2. Similar transmission characteristics were observed with the deuterium discharge for the 8 mrad Pyrex tube sample and beam energy of 40 keV; this was not confirmed with neutron yield measurements, as the yield resulting from these conditions was not measurable above the detector background level. For the 16 mrad case, injection of the 40 keV, 10 μA D_2^+ ion beam resulted in a measured transmission efficiency of 70% and corresponding beam compression factor of 11. Because the taper angle was not observed to affect the transmission efficiency of the 20 μA beam, the substantial increase in the transmission efficiency and beam compression factor is more likely to result from reduced beam losses to the aluminum cap at the front surface of each tapered Pyrex tube. The opening aperture of 3.2 mm on the 16 mrad Pyrex tube sample was slightly larger than the 2.5 mm opening aperture on the 8 mrad Pyrex tube sample, and it is likely that the reduced beam loss before injection and the resultant effects on the transmission due to the increased amount of charge available both act to affect the characteristics of the transmission. Figure 3.33 shows the reduced neutron yield due to the reduction in injected ion current and subsequent reduced ion current at the target.

The burn mark on the neutron production target from the compressed deuterium ion beam transmitted through the 8 mrad Pyrex tube sample can be seen in Figure 3.34. The target also shows burn patterns from previous operating conditions. The beam spot on the target is consistent with the 0.7 mm diameter aperture at the exit of the 8 mrad Pyrex tube sample, indicating little beam expansion over the 3 mm distance from the Pyrex tube exit to the neutron production target.

The transmission efficiencies and beam compression factors, as well as relevant parameters, are summarized for the experimental cases previously discussed in Table 3.1. The neutron yields are normalized to the average neutron count rate measured from the full 40 keV, 20 μA deuterium ion beam incident on the neutron production target. No relative neutron yield is given for the case where the 10 μA ion beam is injected into the Pyrex tube with taper angle of 8 mrad; as previously mentioned, the resultant neutron yield was not detectable above the background level.

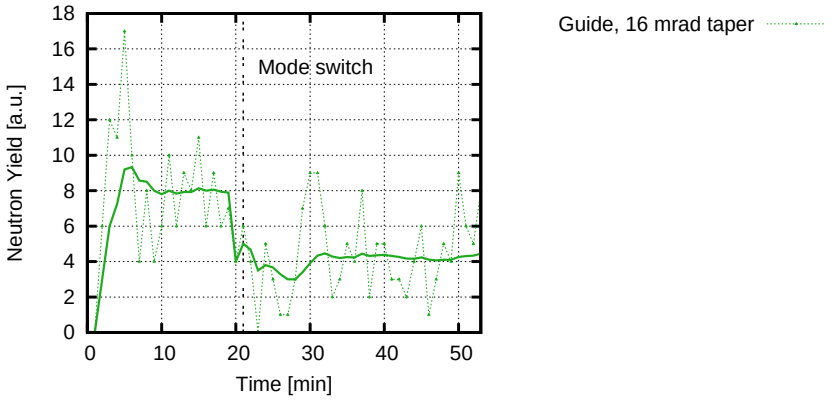

Figure 3.33: Neutron yield measurements for ion guiding with 16 mrad Pyrex tube sample. The solid line indicates the time-averaged neutron yield. The beam energy is 40 keV. The initial injected ion current is 20 μA. The black dashed line at t=21 minutes indicates the point in time when the source operating condition was switched to the 10 μA case. The resultant neutron yield drops by about 50%, consistent with the transmitted ion currents measured at the target.

Table 3.1: Measured transmission efficiencies and beam compression factors.

Injected current [μA]	10		20	
Taper angle [mrad]	8	16	8	16
Transmission efficiency	0.15	0.7	0.5	0.5
Beam compression factor	2	11	6	8
Exit current density $\left[\frac{\mu A}{cm^2}\right]$	400	1400	2600	2000
Relative neutron yield	–	0.46	0.54	0.59

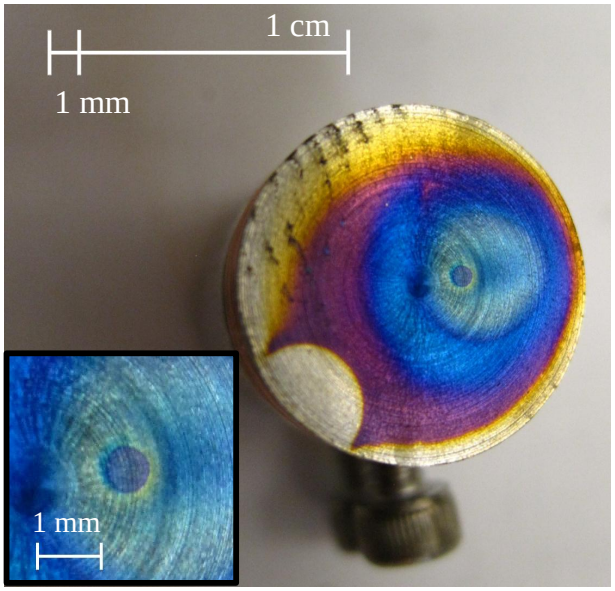

Figure 3.34: Burn mark on the neutron production target from the compressed deuterium ion beam. The inset shows a closer view of the burn mark. The diameter of the burn pattern is consistent with the 0.7 mm aperture at the exit of the 8 mrad Pyrex tube sample.

The measured beam compression factors fall within the range of typical beam compression achieved for the various ion species and ion energies previously studied. As the bulk of previous studies utilize ion beams with magnitudes in the pA/nA range, the absolute values of ion current transmitted, as high as 10 μA, represent at least an order of magnitude increase in the maximum ion current previously observed to have been transmitted through tapered dielectric capillaries with this type of guiding effect. Even with these higher currents, the presence of the time dependent behavior characterized by initial charge buildup before stabilization of the transmission tends to indicate that the dominate transport mechanism is the ion guiding effect, rather than small angle scattering. The sudden, spontaneous discharge events that are thought to be associated with large charge deposition due to high incident currents on the capillary walls were observed, but the degradation and recovery of the transmission occurred on millisecond timescales and thus may not be an issue for final applications; in these experiments, the discharge events occurred on a timescale shorter than the counting interval for the neutron yield measurements, and so the neutron yield measurements were not affected by these transients. The stable transmission of 10 μA of molecular D_2^+ ions suggests the ability to transport even higher beam currents, as the spontaneous discharge events do not result in persistent degradation of the transmission efficiency.

We note here that the measurement of negative currents on the target points to a significant secondary electron current that may artificially enhance the transmission efficiency. The improper suppression of the secondary electron component generated from ion impact at the target, such that secondary electrons emitted at the target are accelerated back towards the ion source, would result in an increased current measurement on the target. Conversely, secondary electrons generated within the Pyrex tube and collected at the target can dominate the current measurement at the target, resulting in a negative current measurement on the target. The inability to distinguish between ion and electron currents in this experimental setup prompted more refined neutron yield measurements for more accurate determination of the transmission efficiency. These more refined neutron yield measurements can also aid in determining the neutron yield contribution from the Pyrex tube

and other auxiliary surfaces, which can also act to artificially enhance the transmission efficiency by including a component that is not generated at the neutron production target. These neutron yield measurements are described in Chapter 4.

Ion guiding summary

The use of tapered dielectric capillaries for passive ion beam focusing has been studied for various ion species and energies, with typical beam compression factors of 5-10 reported for experimental conditions spanning the available parameter space dictated by variations in ion species and charge state, incident beam energy, incident beam current, and geometric transmission efficiency. The bulk of experimental conditions investigated thus far focused on incident beam currents in the pA/nA range. The viability of this passive beam focusing technique for the API application hinges on the ability to transport ion currents of tens to hundreds of μA while maintaining beam compression factors of 5-10. The transmission of 40 keV D_2^+ ion beams of 10 and 20 μA was investigated in first attempts to establish the viability of this method for the passive focusing of high current ion beams. The resultant transmission and beam compression behavior have demonstrated the stable transmission of up to 10 μA of molecular D_2^+ ions; the transport of ion currents of this magnitude represents at least an order of magnitude increase in the maximum ion current previously observed to have been transmitted through tapered dielectric capillaries [62]. The transmission of D_2^+ ion currents of this magnitude was confirmed by comparison of relative neutron yield measurements for 40 keV D_2^+ ions incident on a neutron production target both in the absence of and in the presence of the tapered guides, though it is noted that neutron yield contributions from the Pyrex tube and other auxiliary surfaces must be determined for more accurate transmission efficiencies.

Factors that may affect the viability of this passive focusing technique for neutron generator applications relate to the physical characteristics of the tapered dielectric capillary itself. The inclusion of a glass or similarly fragile dielectric capillary would typically preclude the use of this technique

for neutron generators in harsh environments where vibrations may result in misalignment or breakage of the focusing element. For higher beam energies and higher ion currents, ion energy loss on the inner wall of the tapered dielectric capillary and even at the conductive front surface of the capillary can cause the capillary to heat up and may affect the transmission over time. Gruber [64] observed decreasing transmission efficiency with increasing temperature of borosilicate (Duran) capillaries, suggesting that the increased surface conductivity of the capillary with increased temperature allows charge patches to diffuse such that the ion guiding effect cannot be established. Prolonged transmission of ions through tapered dielectric capillaries has not been extensively explored; these experiments typically observed the transmission characteristics over timescales of 30-60 minutes per run with no adverse effects on the transmitted ion current and resultant neutron yield, and further experiments are necessary to determine whether thermal issues come into play for prolonged beam transmission.

3.5 Summary

Ion optics considerations are necessary to any beam extraction system for efficient beam transport with the desired characteristics imposed by the final application. Understanding the evolution of the various beam parameters is key to finding ways to manipulate the relevant components for system optimization. Ion optics simulations play a vital role in promoting this understanding, providing a means for systematic studies of various effects for both initial design considerations and experimental verification. While traditional ion optics simulation programs provide useful tools for the evaluation of conventional beam extraction systems, the use of passive focusing techniques such as physical beam collimation and ion guiding with tapered dielectric capillaries is difficult to simulate in conjunction with typical extraction components. These passive focusing methods motivate experimental work to establish formulations for the processes at play and the resultant effects on the transport characteristics. The combination of simulation and experimental work is essential to the optimization of ion beam optics and focusing components.

Chapter 4

Neutron yield measurements

4.1 Introduction

Initial BLP source-based D-D neutron generator performance was evaluated in first experiments both with and without ion guiding with the tapered dielectric capillaries. This section addresses several aspects of neutron production from accelerator-based neutron generators that must be considered for efficient operation.

4.2 Beam loading

Accelerator-based neutron generators utilizing the D-D and D-T fusion reactions for neutron production facilitate the fusion reactions by accelerating deuterium and/or tritium ions to high energies into a target. Fusion reactions occur between beam ions and deuterium or tritium atoms already present in the target. The target is either pre-loaded with deuterium or tritium atoms, or "beam loaded" by the deuterium or tritium ions that are extracted from the ion source and driven into the target. Because the neutron yield is proportional to the deuterium or tritium atom density in the target, the neutron yield from a beam-loaded target will increase over time as more ions are driven into the target and the atom concentration in the target increases. The neutron yield will saturate as the deuterium or tritium concentration in

the target equilibrates, requiring a balance between the incoming ions and losses due to the fusion reactions and the diffusion of deuterium or tritium atoms within the target material away from the ion beam spot on the target. It is noted here that for the D-T fusion reaction involving a deuterium ion beam incident on a tritium-loaded target, D-T neutron yields are obtained until the pre-loaded tritium is depleted; as the tritium is depleted by the D-T fusion reactions, the target is simultaneously beam-loaded with deuterium ions, and the neutron yield will become dominated by the D-D yield.

During the ion guiding experiments described in Section 3.4.2, each experimental condition utilized similar beam-loading times over which the average neutron yield remained fairly constant such that steady-state neutron production conditions were assumed. During the course of experimental runs, however, increased average neutron yields were observed once the beam was extracted onto the target following a short duration over which the beam extraction was turned off. It was concluded that the titanium neutron production target had not been loaded to its saturation concentration, and the measured neutron yields did not reflect the maximum values obtainable from a saturated target. Further experiments were undertaken to observe the measured neutron yield over time, both with and without the use of the tapered Pyrex tubes.

The duration of experimental runs typically ranged from 10-90 minutes, over which large fluctuations in the measured neutron yield were observed. These large fluctuations may be the result of fluctuations in the ion beam current due to fluctuations in both the plasma density in the ion source, as well as due to time-dependent ion guiding effects. Over the course of a typical 20-30 minute experimental run, the gradual increase in the average neutron yield and approach to saturation values associated with beam-loading of the target was not observed. The average neutron yield over successive runs, however, was observed to increase over time. The neutron production target was allowed to cool between successive runs over periods of 5-30 minutes; the extraction voltage was turned off such that beam was not extracted onto the target. Resuming the neutron production by resuming the beam extraction typically resulted in high initial neutron yield peaks over the first several minutes of the experimental run, with subsequent values settling to

average neutron yields that were lower than the initial high yield peaks but represented higher average yields when compared to the previous run. The beam on/off procedure was repeated until the average neutron yield over an experimental run period saturated as compared to previous runs. Figure 4.1 shows the neutron yield spectrum for successive runs for a 40 keV deuterium beam transmitted through the 16 mrad Pyrex tube sample onto a titanium target. Saturation yields are reached after approximately 4-5 hours of beam-loading of the target. As noted in Section 3.4.2, the neutron detector was not calibrated for the position in which the detector was placed during these experiments, and thus relative neutron yields must be evaluated.

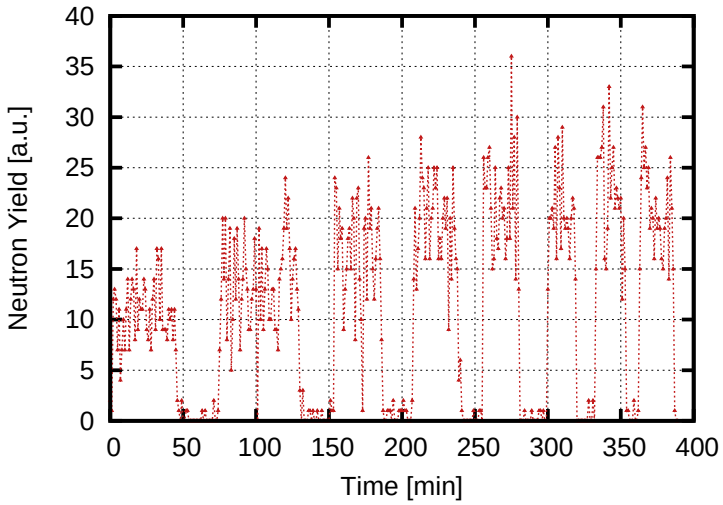

Figure 4.1: Neutron yield spectrum for successive beam on/off experimental runs for a 40 keV deuterium beam. The beam is transmitted through the 16 mrad Pyrex tube sample onto a titanium target. The average neutron yield saturates after a beam-loading period of about 5 hours.

As can be seen in Figure 4.1, the beam-loading period for beams transmitted through the Pyrex tube samples typically lasts for several hours. This is likely due to both the low beam current and low energy of ions incident on the target. Ions generated within and extracted from the BLP source are predominantly diatomic D_2^+ ions that can break up at the target, giving

each resultant atom half of the incident beam energy. SRIM [66] calculations indicate longitudinal ranges of 462 and 210 nm for 40 keV D_2^+ and 20 keV D^+ ions, respectively. The low ion energies result in shallow implant depths into the target, and the active volume of the target is limited by the beam spot on the target and this shallow implant depth. Implanted ions can diffuse away from the active volume, especially as the target heats up due to energy deposition by the implanted ions, resulting in long beam-loading times before saturation concentrations are reached.

The high initial neutron yield peaks often observed at the beginning of experimental runs may be due to implanted ions diffusing toward the surface during the beam off period, or higher deuterium concentrations retained within the active target volume during the beam off period. The beam off period allows the target to cool, slowing diffusion away from the active target volume. Thus the deuterium concentration within the active target volume may be higher than the equilibrium concentration achieved as the experimental run progresses.

Deuterium retention in the titanium target was observed by allowing the target to rest for approximately 16 hours before resuming beam extraction. The measured neutron yield on resuming beam extraction was about 25% of the saturation yield for the case with the tapered Pyrex tube.

4.3 Target material

The saturation concentration of deuterium within the neutron production target is influenced by the target material. As mentioned in Section 1.3.1, common materials utilized for neutron production targets include titanium, molybdenum, and scandium, as these materials are able to retain high concentrations of hydrogen and hydrogen isotopes; hydrogen retention within the titanium lattice due to hydride formation can result in hydrogen to titanium atom ratios of 2:1. Molybdenum has been shown to result in saturation neutron yields of about 45% of the saturation yield from titanium targets [67] due to reduced hydride formation. Target materials demonstrating reduced saturation yields can still be attractive due to the poor thermal conductivity exhibited by titanium. The poor thermal conductivity of titanium prevents

adequate heat dissipation and proper target cooling, and maintaining the maximum saturation neutron yield with thick titanium targets is difficult, especially for high power densities that can be deposited in the small ion beam spots on the target surface. Thus materials with greater thermal conductivities such as molybdenum or copper are often used as backing layers to titanium surface layers for better target cooling, or can replace the titanium altogether. Additional target materials investigated during these neutron yield experiments included copper and Pyrex. These two materials were utilized in attempts to estimate the contribution to the neutron yield from the Pyrex tube and other auxiliary surfaces, as both materials are expected to result in reduced maximum neutron yields as compared to that from adequately cooled titanium targets. Data on relative neutron yields from different target materials under operating conditions similar to the experimental setup utilized here are typically unavailable, with most work focusing on higher energies and higher beam currents. Data compiled by Kim [65] indicate that the integrated fusion cross-sections for both D-D and D-T fusion reactions from titanium and copper targets are of the same magnitude at the low energies utilized in these experiments; Figure 4.2 shows the integrated fusion cross-sections as a function of energy for copper, chromium, and titanium. Because the saturation neutron yields from copper and titanium can be of similar magnitudes at these low energies, any contribution to the total neutron yield from the Pyrex tube and auxiliary surfaces can be difficult to determine. This motivated the incorporation of the Pyrex target material. The beam on/off experiments were performed for both copper and Pyrex targets, as well as the titanium target, for deuterium ion beams with and without the Pyrex guide tube present. The average neutron yield as a function of the elapsed beam on target time is plotted in Figure 4.3 for the various target materials. The average neutron yield data points were obtained by averaging the neutron yield over the duration of the given beam on period. The saturation neutron yields, normalized to the saturation yield from the titanium target with no ion guiding and 20 μA incident deuterium ion current, are given in Table 4.1. In the absence of the Pyrex guide tube, the saturation yields from the copper and Pyrex targets are approximately 40% and 5% of that of the titanium target, respectively. Beam injection

into and transmission through the tapered Pyrex tube results in normalized neutron yields of 40%, 30%, and 13% for titanium, copper, and Pyrex targets, respectively. The saturation yields obtained utilizing the tapered Pyrex tubes are also normalized to the saturation yield from the titanium target without the use of the tapered Pyrex tube.

Table 4.1: Relative neutron yields from tested target materials, for ion beams transmitted with and without tapered Pyrex tube. The neutron yields are normalized to that from the titanium target with no Pyrex tube present.

Target material	No guide	With guide
Titanium	1 ± 0.21	0.41 ± 0.09
Copper	0.48 ± 0.11	0.29 ± 0.11
Pyrex	0.05 ± 0.03	0.13 ± 0.06

The beam-loading times necessary to reach saturation yields ranged from about 3-5 hours for the metallic targets; the Pyrex target required less time to reach saturation yields. The faster saturation time for the Pyrex target is likely due to less deuterium retention within the Pyrex lattice and faster buildup to this reduced saturation concentration.

4.4 Neutron production and beam current transmission from ion guiding with tapered Pyrex tubes

The measured saturation yield data obtained with the various target materials allows for the neutron production from the Pyrex tube and auxiliary surfaces to be determined, as well as the transmission efficiency of ion beams injected into the tapered Pyrex tube. As noted in Section 3.4.2, secondary electron production can mask the beam current as measured at the target, manifesting as a negative current measurement. This was especially prevalent with the use of the copper target, where negative currents on target persisted despite a non-zero neutron yield. When no Pyrex tube is present,

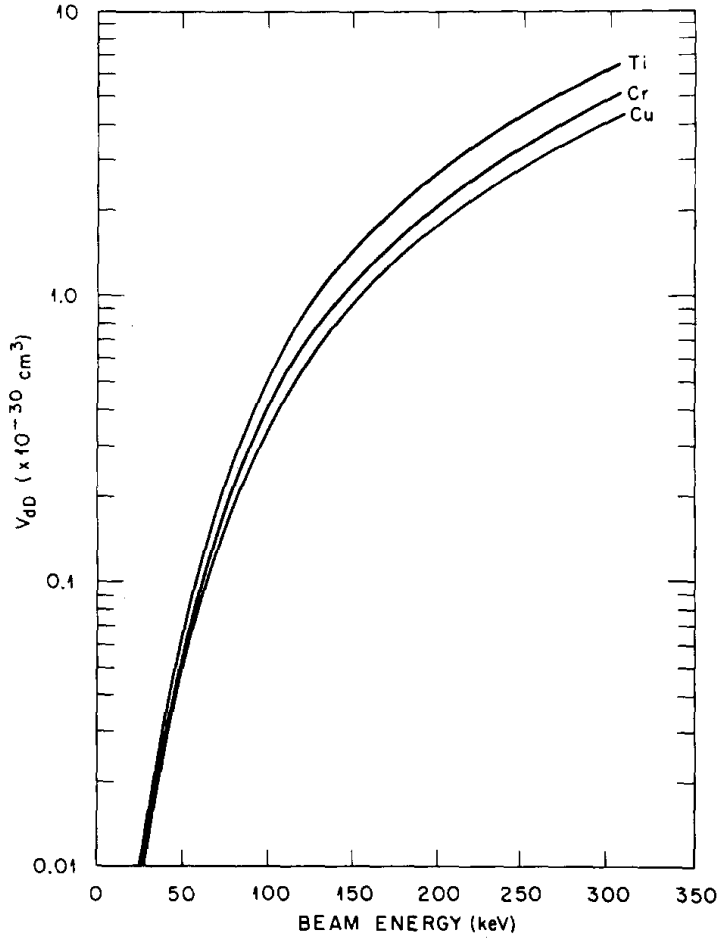

Figure 4.2: Integrated D-D fusion cross-sections as a function of energy for copper, chromium, and titanium targets [65]. At the energies of interest for these experiments, less than 50 keV, the different target materials result in integrated cross-sections of similar magnitudes.

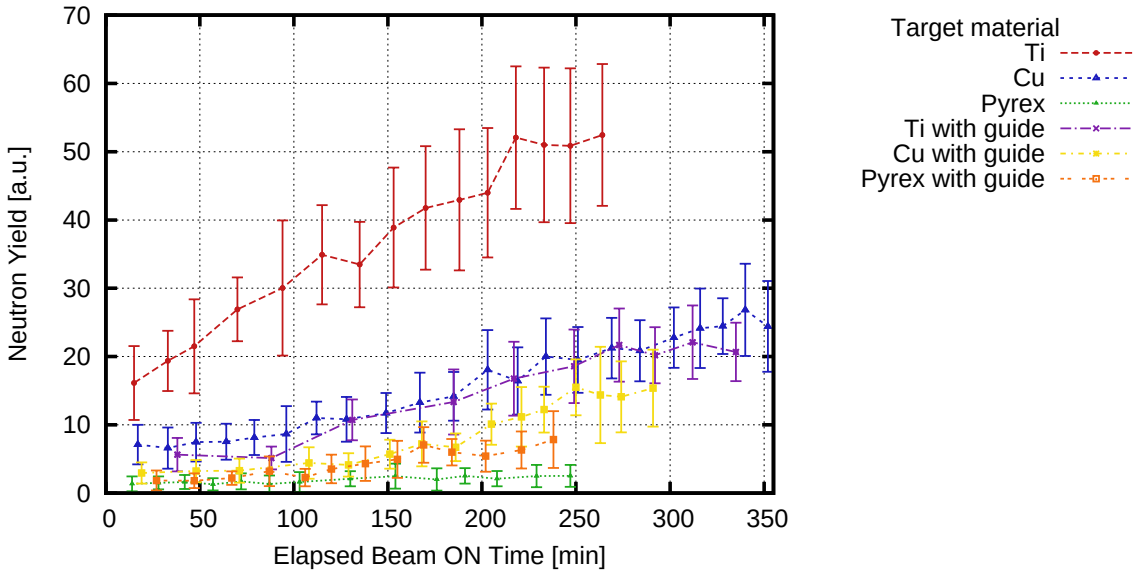

Figure 4.3: Average neutron yields as a function of elapsed beam on target time for different target materials.

neutron production occurs predominantly at the neutron production target, with negligible production occuring at the grid near the aperture in the electron suppression shroud due to high grid transparency. Any neutron production on the grid is thus neglected. Beam losses to the Pyrex tube and auxiliary surfaces will result in neutron production that contributes to the total measured neutron yield for ion beam transmission through the Pyrex tube; thus the total measured yield includes the component from the Pyrex tube and the component from production at the target. The total neutron yield from an ion beam transmitted through the tapered Pyrex tube can then be defined for each target material (here, titanium and copper):

$$Y_{Ti,guide} = Y_{guide} + y_{Ti} \tag{4.1}$$

$$Y_{Cu,guide} = Y_{guide} + y_{Cu} \tag{4.2}$$

where

Y_{guide}: Neutron yield from Pyrex tube and related surfaces
y_{Ti}, y_{Cu}: Neutron yield contribution from production at the target

It is assumed here that the neutron production from the Pyrex tube and auxiliary surfaces is constant for constant injected ion current, regardless of the target material. The neutron yield from copper targets relative to that from titanium targets is given by the ratio of the saturation yields from the respective materials in the absence of the Pyrex guide tube:

$$\eta_{Cu} = \frac{Y_{Cu,noguide}}{Y_{Ti,noguide}} \tag{4.3}$$

The neutron yield contribution from production at the copper target in 4.2 can then be expressed in terms of the neutron yield contribution from production at the titanium target:

$$Y_{Cu,guide} = Y_{guide} + \eta_{Cu} y_{Ti} \tag{4.4}$$

The neutron yield contribution from the Pyrex tube and related surfaces, Y_{guide}, is eliminated from the system of equations by taking the difference of 4.1 and 4.4:

$$Y_{Ti,guide} - Y_{Cu,guide} = y_{Ti}(1 - \eta_{Cu}) \tag{4.5}$$

$$y_{Ti} = \frac{Y_{Ti,guide} - Y_{Cu,guide}}{1 - \eta_{Cu}} \tag{4.6}$$

The transmission efficiency, previously defined as the ratio of exit to incident beam currents, is given by the ratio of the neutron yield contribution from production at the titanium target with the Pyrex tube to that without the Pyrex tube:

$$\epsilon = \frac{y_{Ti}}{Y_{Ti,noguide}} = \frac{\frac{Y_{Ti,guide} - Y_{Cu,guide}}{1-\eta_{Cu}}}{Y_{Ti,noguide}} = \frac{Y_{Ti,guide} - Y_{Cu,guide}}{Y_{Ti,noguide} - Y_{Cu,noguide}} \tag{4.7}$$

Thus the measured values $Y_{Ti,guide}$, $Y_{Cu,guide}$, $Y_{Ti,noguide}$, $Y_{Cu,noguide}$ determine the transmission efficiency. Equations 4.1 and 4.6 can then be used to evaluate the neutron yield contribution from the Pyrex tube:

$$Y_{guide} = Y_{Ti,guide} - y_{Ti} = Y_{Ti,guide} - \epsilon Y_{Ti,noguide} \tag{4.8}$$

Evaluating Equations 4.7 and 4.8 for the transmission efficiency and the neutron yield contribution from the guide using the relative neutron yield data in Table 4.1 gives a transmission efficiency for the 16 mrad Pyrex tube sample of 24%, about half of the transmission efficiency obtained through beam current measurements, and a relative neutron yield from the guide tube of 0.17 ± 0.04. Similar analysis can be performed using the data obtained from the Pyrex target with and without ion guiding; the data from the Pyrex target gives a transmission efficiency of 30%, and a relative neutron yield from the guide tube of 0.11 ± 0.03. It is noted here that the relative neutron yield contribution from the Pyrex guide obtained using the copper target data is greater than the total relative neutron yield from the case utilizing the Pyrex guide tube along with the Pyrex target, but is within the calculated experimental error due to the large fluctuations in the neutron yield data. The calculated transmission efficiencies, resultant beam compression factors, and relative neutron yield contributions from the Pyrex guide are summarized in Table 4.2.

Table 4.2: Calculated transmission efficiency, beam compression factor, and relative neutron yield contribution from the 16 mrad Pyrex tube sample. Values are calculated with Ti/Cu data and Ti/Pyrex data.

	Cu data	Pyrex data
Transmission efficiency	0.24	0.30
Beam compression factor	3.8	4.8
Y_{guide}	0.17 ± 0.04	0.11 ± 0.03

The reduced transmission efficiency compared to the results obtained through beam current measurements may reflect the presence of a secondary electron current that acts to artificially increase the transmission efficiency.

This reduced transmission efficiency, however, still results in compression of the transmitted ion beam that is useful for these neutron generator applications. Further work is necessary to optimize the transmission efficiency and resultant beam compression factor.

It is noted here that the use of tapered Pyrex tubes for beam compression can induce ion energy distributions that result in reduced neutron yields, especially if small misalignments between the beam axis and tapered Pyrex tube axis are present. This effect would not be apparent in the ion current measurement at the target, as the total charge is collected regardless of the ion energy. The molecular D_2^+ ions may also dissociate at the inner surface of the Pyrex tube, with further reduced neutron yields due to ion energy losses of the lower energy atomic species. The likely induced ion energy spread with the use of tapered Pyrex tubes for ion guiding and subsequent beam compression, as well as contributions to the neutron yield from the tapered Pyrex tube itself, has implications for further use of this method for neutron generator applications. Energy loss of transmitted ions due to interactions with and within the guide tube act to reduce the maximum neutron yield, requiring either increased ion current or increased incident beam energy to account for these losses if a specific neutron yield is required.

4.5 Summary

Various issues related to the neutron production target must be considered when attempting to maximize the neutron yield from an accelerator-based neutron generator. Proper target design requires the appropriate choice of target material for maximum capacity for and sustained retention of the hydrogen isotopes to be used for neutron generation. The use of target materials with poor thermal conductivity, such as the ever-prevalent titanium, requires the incorporation of active or passive cooling methods for sustained maximum neutron yields. Obtaining maximum neutron yields also requires sufficient loading of the neutron production target, whether by pre-loading in a separate process or beam-loading from the neutron generator itself. For low beam currents, low beam energies, and small beam spot sizes characteristic of the BLP neutron generator, typical beam-loading times of 5-6 hours were

required before the neutron yield was observed to saturate. The small beam spot on target from ions transmitted through tapered Pyrex guide tubes results in a small active area for neutron production on the target surface, with deuterium retention of approximately 25% within the target after a prolonged period of neutron generator inactivity.

Relative neutron yields from the BLP neutron generator from ion beams transmitted both with and without the use of the tapered Pyrex tubes were measured for a more refined estimate of the neutron yield contribution from the Pyrex tube itself. Titanium, copper, and Pyrex targets were utilized, and the Pyrex tube was calculated to contribute as much as 40% of the total neutron yield for the case when the Pyrex tube was utilized in conjunction with the titanium target. This contribution to the neutron yield results in calculated transmission efficiencies that are as much as a factor of 2 lower than that obtained from current measurements at the neutron production target; the higher transmission efficiency previously measured may include current contributions from secondary electrons that would not contribute to the neutron yield. The neutron yield contribution from the Pyrex tube, as well as energy losses sustained by transmitted ions, have implications for further use of this ion guiding method for neutron generator applications that must be addressed with further study.

Chapter 5

Conclusion

5.1 Summary and outlook

The use of accelerator-based neutron generators for non-destructive imaging and analysis in commercial and security applications is continuously under development, with improvements to available systems and combinations of available techniques revealing new capabilities for real-time elemental and isotopic analysis. The recent application of associated particle imaging techniques for time- and directionally-tagged neutrons to induced fission and transmission imaging methods demonstrates such capabilities in the characterization of fissile material configurations and greatly benefits from improvements to existing neutron generator systems. Increased neutron yields and improved spatial resolution can enhance the capabilities of imaging methods utilizing the API technique. The work presented in this dissertation focused on the development of components for use within an API neutron generator with enhanced system spatial resolution. The major focus areas were the ion source development for plasma generation, and passive ion beam focusing techniques for the small ion beam widths necessary for the enhanced spatial resolution. The ion source development focused on exploring methods for improvement of Penning-type ion sources that are used in conventional API neutron generator systems, while the passive beam focusing techniques explored both ion beam collimation and ion guiding with tapered dielectric capillaries for reduced beam widths at the neutron production target.

Penning-type ion sources are utilized in commercially available API neutron generator systems due to their compactness, ease of operation, and low power consumption. These types of ion sources, however, are characterized by low plasma densities and low atomic ion fractions in the discharge that make them unattractive for neutron generator applications requiring high neutron yields. The ion source development undertaken as part of this dissertation work focused on methods by which improvements to the plasma density and atomic ion fraction of Penning-type ion sources could be effected, and the modular Berkeley Lab Penning source was designed and fabricated to test the effects of the various improvement schemes. These improvement schemes included electrode material variation for enhanced plasma density from increased secondary electron emission under ion bombardment; electron injection into the discharge by way of electron field emission from carbon nanofiber arrays; and enhanced magnetic confinement of the plasma with the use of multi-cusp magnetic fields. Strategic combinations of these improvement schemes have resulted in a factor of 20 improvement in the extracted ion current density over the baseline source performance. The resultant extracted ion current density of 2.2 mA/cm^2 is comparable to existing Penning sources for neutron generator applications, with the Berkeley Lab Penning source exhibiting lower power consumption. The current iteration of the Berkeley Lab Penning source utilizes an electromagnet to generate the axial magnetic field required of Penning-type discharges; this electromagnet is limited in the maximum applied magnetic field and is highly undesirable for a compact, field-portable neutron generator. The planned replacement of this electromagnet with a permanent-magnet generated, adjustable axial magnetic field of greater maximum field strength provides a means for further source improvement.

The spatial resolution of an API system is heavily dependent on the diameter of the ion beam spot at the neutron production target. Current API systems can achieve beam spots as small as 2 mm in diameter with the use of active focusing elements. In this work, passive beam focusing techniques were explored to achieve beam widths of 1 and 2 mm in diameter without the use of active focusing elements. These passive beam focusing techniques can result in substantial current losses between the ion source and the neutron

production target, and thus represent a tradeoff consideration in the design of a compact, field-portable neutron generator system of minimum complexity. Ion beam collimation with the use of high aspect ratio extraction channels at the ion source was explored to physically remove those ions in the beam with high divergence angles. The collimation effect is most apparent for low beam energies, where increasing channel length resulted in decreased beam diameter. At beam energies of 81 keV, the beam diameter at the target was consistent with the diameter of the extraction aperture, indicating that the high aspect ratio extraction channels act to suppress those ions with high divergence angles that act to increase the beam diameter downstream. The increased extraction channel length also acted to significantly reduce the ion current reaching the target, with each 3 mm addition to the extraction channel length resulting in a 30% reduction in the ion current at the target. The significant beam loss due to collimation with high aspect ratio extraction channels, with no focusing effects and corresponding increase in beam current density at the target, makes the use of ion beam collimation for small beam widths viable only for high ion current densities.

Because the use of high aspect ratio extraction channels results in significant beam loss and no increase in the extracted ion current density, the passive beam focusing technique known as ion guiding was explored. Ion guiding with tapered dielectric capillaries involves the injection of an ion beam into the tapered capillary, with initial beam losses to the inner wall of the capillary required to charge up this inner surface through the creation of local charge patches. The charge patches then act to deflect subsequent ions away from the wall, guiding the ions through the length of the tapered dielectric capillary to the exit. The amount of beam loss/charge deposition necessary to establish the ion guiding effect varies over a range of parameters including the incident ion species and charge state, beam energy, and geometric parameters of the tapered dielectric capillary, with the net effect of beam compression and increased ion current density at the exit of the capillary typically observed. Typical incident beam currents studied thus far fall in the pa/nA range, far lower than the tens of μA of ion current required for general neutron generator applications. The use of ion guiding with tapered dielectric capillaries for the transmission of tens of μA of hydrogen or

deuterium ion current thus represents an area of the experimental parameter space that has not yet been explored. Tapered Pyrex tubes with inlet inner diameters of 2-3 mm and exit inner diameters of 0.5-1 mm were used in the ion guiding experiments for the passive focusing of ion beams to beam widths on the order of 1 mm in diameter. For a 40 keV, 20 μA deuterium ion beam from the Berkeley Lab Penning source, average transmission efficiencies of 50% were measured. This represents a transmitted ion current of 10 μA and corresponding beam compression factor of 6-8. Attempts to verify the magnitude of the transmitted ion current were made with the simultaneous measurement of the relative neutron yield resulting from D-D fusion reactions at a neutron production target. Initial neutron yield measurements confirmed the relative magnitudes of the ion beams transmitted both with and without the use of the tapered Pyrex tubes, but closer examination warranted further study into the neutron production target material and deuterium concentrations within the target.

Titanium, copper, and Pyrex target materials were utilized to observe the beam-loading behavior and resultant relative neutron yields at saturation for ion beams transmitted both with and without the use of tapered Pyrex tubes. These measurements allowed for a secondary calculation of the transmission efficiency; the calculated transmission efficiency obtained from the neutron yield data was 24%, about half of that obtained from the current measurements. The resultant beam compression factor is subsequently also reduced. A possible explanation for the discrepancy in the transmission efficiency is an artificially high transmission efficiency that includes current contributions from secondary electrons emitted at the target; thus the measured current at the target is higher than the actual ion current collected. The Pyrex tube itself was calculated to contribute to the measured neutron yield, contributing as much as 40% of the neutron yield for ion transmission through the Pyrex tube to the titanium target. The neutron yield contribution from the Pyrex tube and the ion energy losses within the Pyrex tube have implications for the further use of the ion guiding method in neutron generator applications. Further work is necessary to more accurately measure the transmitted ion current, as well as characterize the energy distribution of ions transmitted through tapered dielectric capillaries and the resultant effects on the neu-

tron yield. Nevertheless, the stable transmission of 5-10 μA of ion current through a tapered dielectric capillary represents at least an order of magnitude increase in the maximum ion current typically observed to have been transmitted with this ion guiding effect. These results are promising for the further extension of this method to higher beam currents for increased neutron yields.

The methods and results presented in this work are especially relevant to the improvement of existing accelerator-based neutron generators utilizing Penning-type ion sources both for the API application and for other applications that may benefit from reduced ion beam diameters. Continued interest in the use of accelerator-based neutron generators for non-destructive analysis and imaging methods will allow for further developments in the field of neutron generator technology.

Bibliography

[1] Andy Buffler. Contraband detection with fast neutrons. *Radiation Physics and Chemistry*, 71(3-4):853–861, October 2004.

[2] Dennis Slaughter, Mark Accatino, and A Bernstein. *Detection of special nuclear material in cargo containers using neutron interrogation.* Number August. 2003.

[3] C S Lim, J R Tickner, B D Sowerby, D a Abernethy, a J McEwan, S Rainey, R Stevens, C Manias, and D Retallack. An on-belt elemental analyser for the cement industry. *Applied radiation and isotopes : including data, instrumentation and methods for use in agriculture, industry and medicine*, 54(1):11–9, January 2001.

[4] J.C. Overley. Element-sensitive computed tomography with fast neutrons. *Nuclear Instruments and Methods in Physics Research Section B: Beam Interactions with Materials and Atoms*, 24-25:1058–1062, April 1987.

[5] J Rynes, J Bendahan, T Gozani, R Loveman, J Stevenson, and C Bell. Gamma-ray and neutron radiography as part of a pulsed fast neutron analysis inspection system. *Nuclear Instruments and Methods in Physics Research Section A: Accelerators, Spectrometers, Detectors and Associated Equipment*, 422(1-3):895–899, February 1999.

[6] J.C. Overley, M.S. Chmelik, R.J. Rasmussen, R.M.S. Schofield, G.E. Sieger, and H.W. Lefevre. Explosives detection via fast neutron transmission spectroscopy. *Nuclear Instruments and Methods in Physics Research Section B: Beam Interactions with Materials and Atoms*, 251(2):470–478, October 2006.

[7] Eric B Norman, Stanley G Prussin, Ruth-Mary Larimer, Howard Shugart, Edgardo Browne, Alan R Smith, Richard J McDonald, Heino Nitsche, Puja Gupta, Michael I Frank, and Thomas B Gosnell. Signatures of fissile materials: high-energy γ rays following fission. *Nuclear Instruments and Methods in Physics Research Section A: Accelerators, Spectrometers, Detectors and Associated Equipment*, 521(2-3):608–610, April 2004.

[8] a.S. Vorobyev, O.a. Shcherbakov, Yu.S. Pleva, a.M. Gagarski, G.V. Val'ski, G.a. Petrov, V.I. Petrova, and T.a. Zavarukhina. Measurements of angular and energy distributions of prompt neutrons from thermal neutron-induced fission. *Nuclear Instruments and Methods in Physics Research Section A: Accelerators, Spectrometers, Detectors and Associated Equipment*, 598(3):795–801, January 2009.

[9] W.C. Lee, D.B. Mahood, P Ryge, P Shea, and T Gozani. Thermal neutron analysis (TNA) explosive detection based on electronic neutron generators. *Nuclear Instruments and Methods in Physics Research Section B: Beam Interactions with Materials and Atoms*, 99(1-4):739–742, May 1995.

[10] Tsahi Gozani. Novel applications of fast neutron interrogation methods. *Nuclear Instruments and Methods in Physics Research Section A: Accelerators, Spectrometers, Detectors and Associated Equipment*, 353(1-3):635–640, December 1994.

[11] Tsahi Gozani. Understanding the physics limitations of PFNA - the nanosecond pulsed fast neutron analysis. *Nuclear Instruments and Methods in Physics Research Section B: Beam Interactions with Materials and Atoms*, 99(1-4):743–747, May 1995.

[12] Albert Beyerle, J.Paul Hurley, and Laura Tunnell. Design of an associated particle imaging system. *Nuclear Instruments and Methods in Physics Research Section A: Accelerators, Spectrometers, Detectors and Associated Equipment*, 299(1-3):458–462, December 1990.

[13] A. Beyerle, R. Durkee, G. Headley, J.P. Hurley, and L. Tunnell. Associated particle imaging. In *Conference Record of the 1991 IEEE Nuclear Science Symposium and Medical Imaging Conference*, pages 1298–1304. IEEE.

[14] LE Ussery and CL Hollas. Design and development of the associated-particle three-dimensional imaging technique. 1994.

[15] D Chichester, M Lemchak, and J Simpson. The API 120: A portable neutron generator for the associated particle technique. *Nuclear Instruments and Methods in Physics Research Section B: Beam Interactions with Materials and Atoms*, 241(1-4):753–758, December 2005.

[16] P.a. Hausladen, P.R. Bingham, J.S. Neal, J.a. Mullens, and J.T. Mihalczo. Portable fast-neutron radiography with the nuclear materials identification system for fissile material transfers. *Nuclear Instruments and Methods in Physics Research Section B: Beam Interactions with Materials and Atoms*, 261(1-2):387–390, August 2007.

[17] Paul Hausladen, Matthew A Blackston, James Allen Mullens, Seth M McConchie, John T Mihalczo, Philip R Bingham, Milton Nance Ericson, and Lorenzo Fabris. Induced-fission imaging of nuclear material. Technical report, Oak Ridge National Laboratory (ORNL), 2010.

[18] H.-S Bosch and G.M Hale. Improved formulas for fusion cross-sections and thermal reactivities. *Nuclear Fusion*, 32(4):611–631, April 1992.

[19] J. Csikai. *CRC handbook of fast neutron generators*. Number v. 2 in CRC Handbook of Fast Neutron Generators. CRC Press, 1987.

[20] Y Wu, J P Hurley, Q Ji, J Kwan, and K N Leung. Development of a RF-Driven Neutron Generator for Associated Particle Imaging. 56(3):1306–1311, 2009.

[21] Qing Ji, Floyd D. McDaniel, and Barney L. Doyle. Compact Permanent Magnet Microwave-Driven Neutron Generator. 532:528–532, 2011.

[22] L. Vályi. *Atom and ion sources*. Wiley-Interscience Publications. Wiley, 1977.

[23] F.M. Penning. Die glimmentladung bei niedrigem druck zwischen koaxialen zylindern in einem axialen magnetfeld. *Physica*, 3(9):873–894, November 1936.

[24] F. C. Hoh. Instability of Penning-Type Discharges. *Physics of Fluids*, 6(8):1184, 1963.

[25] Felix K. Chen. Investigation of the striking characteristics of a Penning ion source. *Journal of Applied Physics*, 56(11):3191, 1984.

[26] H. Tawara, T. Itikawa, H. Nishimura, and M. Yoshino. *Cross Sections and Related Data for Electron Collisions with Hydrogen Molecules and Molecular Ions*. Journal of physical and chemical reference data. Reprint. American Chemical Society, 1990.

[27] P Rohwer, H Baumann, W Schutze, and K Bethge. Studies of the center potential in a penning discharge. *Nuclear Instruments and Methods in Physics Research*, 211(2-3):543–546, June 1983.

[28] W Schuurman. Investigation of a low pressure penning discharge. *Physica*, 36(1):136–160, 1967.

[29] R. Baragiola, E. Alonso, and A. Florio. Electron emission from clean metal surfaces induced by low-energy light ions. *Physical Review B*, 19(1):121–129, January 1979.

[30] L N Large and W S Whitlock. Secondary Electron Emission from Clean Metal Surfaces Bombarded by Fast Hydrogen Ions. *Proceedings of the Physical Society*, 79(1):148–157, January 1962.

[31] D Hasselkamp, K.G. Lang, A Scharmann, and N Stiller. Ion induced electron emission from metal surfaces. *Nuclear Instruments and Methods*, 180(2-3):349–356, April 1981.

[32] J. Ferrón, E.V. Alonso, R.A. Baragiola, and A. Oliva-Florio. Ion-electron emission: The effect of oxidation. *Surface Science*, 120(2):427–434, August 1982.

[33] E. R. Cawthron, D. L. Cotterell, and M. Oliphant. The Interaction of Atomic Particles with Solid Surfaces at Intermediate Energies. I. Secondary Electron Emission. *Proceedings of the Royal Society A: Mathematical, Physical and Engineering Sciences*, 314(1516):39–51, December 1969.

[34] P.D. W. M. Haynes, P.D. David R. Lide, and T.J. Bruno. *CRC Handbook of Chemistry and Physics 2012-2013*. CRC Handbook of Chemistry & Physics. CRC Press, 2012.

[35] J Ferron, E V Alonso, R A Baragiola, and A Oliva-Florio. Electron emission from molybdenum under ion bombardment. *Journal of Physics D: Applied Physics*, 14(9):1707–1720, September 1981.

[36] G Lakits, F Aumayr, and H Winter. Statistics of ion-induced electron emission from a clean metal surface. *Review of Scientific Instruments*, 60(10):3151, 1989.

[37] Henry Ivey. Thermionic Electron Emission from Carbon. *Physical Review*, 76(4):567–567, August 1949.

[38] John Cumings and a. Zettl. Field emission and current-voltage properties of boron nitride nanotubes. *Solid State Communications*, 129(10):661–664, March 2004.

[39] Jia Zhang, Kian Ping Loh, Mu Deng, Michael B. Sullivian, Jianwei Zheng, and Ping Wu. Work function of (8,0) single-walled boron nitride nanotube at the open tube end. *Journal of Applied Physics*, 99(10):104309, 2006.

[40] Terence Taylor and John S.C. Wills. A high-current low-emittance dc ECR proton source. *Nuclear Instruments and Methods in Physics Research Section A: Accelerators, Spectrometers, Detectors and Associated Equipment*, 309(1-2):37–42, November 1991.

[41] S. K. Guharay, E. Sokolovsky, and J. Orloff. Characteristics of ion beams from a Penning source for focused ion beam applications. *Journal of Vacuum Science & Technology B: Microelectronics and Nanometer Structures*, 17(6):2779, 1999.

[42] Russell G. Meyerand and Sanborn C. Brown. High-Current Ion Source. *Review of Scientific Instruments*, 30(2):110, 1959.

[43] Arun Persaud, Ole Waldmann, Rehan Kapadia, Kuniharu Takei, Ali Javey, and Thomas Schenkel. A compact neutron generator using a field ionization source. *The Review of scientific instruments*, 83(2):02B312, February 2012.

[44] Ole Waldmann, Arun Persaud, Rehan Kapadia, Kuniharu Takei, Frances I. Allen, Ali Javey, and Thomas Schenkel. Effects of palladium

coating on field-emission properties of carbon nanofibers in a hydrogen plasma. *Thin Solid Films*, pages 4–7, February 2013.

[45] K Leung. Optimization of permanent magnet plasma confinement. *Physics Letters A*, 51(8):490–492, May 1975.

[46] O Chubar, P Elleaume, and J Chavanne. A three-dimensional magnetostatics computer code for insertion devices. *Journal of synchrotron radiation*, 5(Pt 3):481–4, May 1998.

[47] Ralph Hollinger. *Ion Extraction*, pages 61–86. Wiley-VCH Verlag GmbH & Co. KGaA, 2005.

[48] R Becker and WB Herrmannsfeldt. Igun-a program for the simulation of positive ion extraction including magnetic fields. *Review of scientific instruments*, 63(4):2756–2758, 1992.

[49] Jack E Boers. An interactive version of the pbguns program for the simulation of axisymmetric and 2-d, electron and ion beams and guns. In *Particle Accelerator Conference, 1995., Proceedings of the 1995*, volume 4, pages 2312–2313. IEEE, 1995.

[50] David P Grote, Alex Friedman, Irving Haber, and Simon Yu. Three-dimensional simulations of high current beams in induction accelerators with WARP3d. *Fusion Engineering and Design*, 32-33:193–200, November 1996.

[51] Y Wu, J P Hurley, Q Ji, J W Kwan, and K N Leung. Sealed operation of a rf driven ion source for a compact neutron generator to be used for associated particle imaging. *The Review of scientific instruments*, 81(2):02B908, February 2010.

[52] Michael D Abràmoff, Paulo J Magalhães, and Sunanda J Ram. Image processing with imagej. *Biophotonics international*, 11(7):36–42, 2004.

[53] T Ikeda, T M Kojima, Y Iwai, Y Kanai, T Kambara, T Nebiki, T Narusawa, and Y Yamazaki. Production of a nm sized slow HCI beam with a guiding effect. *Journal of Physics: Conference Series*, 58:68–73, March 2007.

[54] Takuya Nebiki, M. Hasnat Kabir, and Tadashi Narusawa. In-air {PIXE} analysis by means of glass capillary optics. *Nuclear Instruments and Methods in Physics Research Section B: Beam Interactions with Materials and Atoms*, 249(1-2):226–229, 2006. <ce:title>Ion Beam Analysis</ce:title> <ce:subtitle>Proceedings of the Seventeenth International Conference on Ion Beam Analysis</ce:subtitle> <xocs:full-name>Seventeenth International Conference on Ion Beam Analysis</xocs:full-name>.

[55] N. Stolterfoht, J.-H. Bremer, V. Hoffmann, R. Hellhammer, D. Fink, a. Petrov, and B. Sulik. Transmission of 3 keV Ne7+ Ions through Nanocapillaries Etched in Polymer Foils: Evidence for Capillary Guiding. *Physical Review Letters*, 88(13):133201, March 2002.

[56] Martin Kreller, Günter Zschornack, and Ulrich Kentsch. Guiding of argon ions through a tapered glass capillary. *Nuclear Instruments and Methods in Physics Research Section B: Beam Interactions with Materials and Atoms*, 269(9):1032–1035, May 2011.

[57] T. Nebiki, T. Yamamoto, T. Narusawa, M. B. H. Breese, E. J. Teo, and F. Watt. Focusing of MeV ion beams by means of tapered glass capillary optics. *Journal of Vacuum Science & Technology A: Vacuum, Surfaces, and Films*, 21(5):1671, 2003.

[58] T. Nebiki, D. Sekiba, H. Yonemura, M. Wilde, S. Ogura, H. Yamashita, M. Matsumoto, K. Fukutani, T. Okano, J. Kasagi, Y. Iwamura, T. Itoh, S. Kuribayashi, H. Matsuzaki, and T. Narusawa. Taper angle dependence of the focusing effect of high energy heavy ion beams by glass capillaries. *Nuclear Instruments and Methods in Physics Research Section B: Beam Interactions with Materials and Atoms*, 266(8):1324–1327, April 2008.

[59] R. Nakayama, M. Tona, N. Nakamura, H. Watanabe, N. Yoshiyasu, C. Yamada, a. Yamazaki, S. Ohtani, and M. Sakurai. Guiding and blocking of highly charged ions through a single glass capillary. *Nuclear Instruments and Methods in Physics Research Section B: Beam Interactions with Materials and Atoms*, 267(14):2381–2384, July 2009.

[60] N. Stolterfoht, R. Hellhammer, J. Bundesmann, and D. Fink. Scaling laws for guiding of highly charged ions through nanocapillaries in an insulating polymer. *Physical Review A*, 77(3):032905, March 2008.

[61] J Hasegawa, S Shiba, H Fukuda, and Y Oguri. A compact micro-beam system using a tapered glass capillary for proton-induced X-ray radiography. *Nuclear Instruments and Methods in Physics Research Section B: Beam Interactions with Materials and Atoms*, 266(10):2125–2129, May 2008.

[62] K a Vokhmyanina, L a Zhilyakov, a V Kostanovsky, V S Kulikauskas, V P Petukhov, and G P Pokhil. Transportation and focusing of accelerated proton beams by means of dielectric channels. *Journal of Physics A: Mathematical and General*, 39(17):4775–4779, April 2006.

[63] Jun Hasegawa, Sarawut Jaiyen, Chalermpong Polee, Nares Chankow, and Yoshiyuki Oguri. Transport mechanism of MeV protons in tapered glass capillaries. *Journal of Applied Physics*, 110(4):044913, 2011.

[64] E. Gruber, G. Kowarik, F. Ladinig, J. Waclawek, D. Schrempf, F. Aumayr, R. Bereczky, K. Tokési, P. Gunacker, T. Schweigler, C. Lemell, and J. Burgdörfer. Temperature control of ion guiding through insulating capillaries. *Physical Review A*, 86(6):062901, December 2012.

[65] Jinchoon Kim. Neutron sources using D-T mixed beams driven into solid target. *Nuclear Instruments and Methods*, 145(1):9–17, August 1977.

[66] James F Ziegler, MD Ziegler, and JP Biersack. Srim–the stopping and range of ions in matter (2010). *Nuclear Instruments and Methods in Physics Research Section B: Beam Interactions with Materials and Atoms*, 268(11):1818–1823, 2010.

[67] Ying Wu. Development of a compact neutron generator to be used for associated particle imaging utilizing a rf-driven ion source, 2009. Copyright - Copyright ProQuest, UMI Dissertations Publishing 2009; Last updated - 2012-07-05; DOI - 2128972571; 52930381; 66569; 9781124142241; 3413523; First page - n/a; M3: Ph.D.; M1: 3413523.